PACIFIC EARTHQUAKE ENGINEERING RESEARCH CENTER

Toward Multi-Tier Modeling of Liquefaction Impacts on Transportation Infrastructure

Brett W. Maurer

Mertcan Geyin

Alex J. Baird

Department of Civil and Environmental Engineering
University of Washington

PEER Report No. 2021/04

Pacific Earthquake Engineering Research Center
Headquarters at the University of California, Berkeley
July 2021

PEER 2021/04
July 2021

Towards Multi-Tier Modeling of Liquefaction Impacts on Transportation Infrastructure

Brett W. Maurer
Mertcan Geyin
Alex J. Baird

Department of Civil and Environmental Engineering
University of Washington

PEER Report 2021/04
Pacific Earthquake Engineering Research Center
Headquarters at the University of California, Berkeley

July 2021

ABSTRACT

Semi-empirical models based on *in situ* geotechnical tests have been the standard-of-practice for predicting soil liquefaction since 1971. More recently, prediction models based on free, readily available data have grown in popularity. These "geospatial models" rely on satellite remote sensing to infer subsurface traits without *in situ* tests. While the concept of such an approach is not new, the recent models of Zhu et al. [2015; 2017] are arguably the most rigorously formulated and well-trained to date. The use of such models is appealing for a range of applications, but these models have not been evaluated using independent datasets, nor have they been tested against more established geotechnical methods. These independent evaluations are important for community acceptance and for identifying pathways to improve the models via future research. In other words, when the geospatial models perform poorly, what do they miss that geotechnical models do not? Moreover, the physical damage and monetary loss from liquefaction are arguably more important than the probability of liquefaction occurring. The extension of geospatial models to predict the consequences from liquefaction is both enticing and consistent with the objectives of PEER. Accordingly, the presented study has two main components.

First, using 15,222 liquefaction case histories from 24 earthquakes, the performance of 23 models based on geotechnical or geospatial data are assessed using standardized metrics. Uncertainty due to finite sampling of case histories is accounted for and used to establish statistical significance. Geotechnical predictions are found to be significantly more efficient worldwide, yet successive models proposed over the last twenty years show little or no demonstrable improvement. In addition, geospatial models outperform geotechnical models for large subsets of the data—a provocative finding given the relative time and cost requirements underlying these predictions. Comparisons between geotechnical predictions versus geospatial models provide key insights into improving geospatial models.

Second, while geospatial models have limitations that can and should be addressed via future research, their capacity for predicting liquefaction is promising, as demonstrated herein for certain events. Accordingly, functions are developed to extend the use of the Zhu et al. models [2015; 2017] to predict: (1) severity of liquefaction ejecta; (2) magnitude of ground settlement; and (3) infrastructure damage and loss. Each of these efforts utilizes a subset of data for which geospatial models performed well in the first part of the study (i.e., the locations studied are those where geospatial models, in general, correctly predicted the occurrence and non-occurrence of liquefaction). These analyses thus represent a best-case scenario for predicting liquefaction consequences using geospatial models.

With respect to infrastructure damage and loss, this study focuses on structures built atop shallow foundation systems, which are the most common worldwide. Utilizing damage-survey data and insurance loss assessments for 62,000 such assets, functions are developed to predict liquefaction-induced damage conditioned on the Zhu et al. models. It is shown that while geospatial models are relatively useful for predicting some modes of damage (e.g., global settlement of foundations), they appear not to capture other significant and very costly modes (e.g., stretching, twisting, and separation of foundations). These modes of failure are presumably

dependent on asset- and site-specific details that geospatial models do not consider. As an example, differential settlements cause structural distortion and are typically very costly, but such settlements are likely correlated to subsurface variability, which geospatial models cannot predict. Due to these limitations (i.e., the inability to predict all modes of damage), currently geospatial models are poor predictors of monetary loss at the site and neighborhood scales. Efforts to predict damage and loss at coarser scales (e.g., on a per-earthquake basis) may be more fruitful.

The most salient conclusions of this study are summarized as follows:

1. Geospatial models demonstrate provocative potential for predicting the occurrence and severity of surficial liquefaction manifestations in the free field. Moreover, these models outperform geotechnical models (which are far costlier and time-consuming to implement) for the large subsets of the data analyzed.

2. However, geospatial models were significantly less efficient on a global scale (i.e., when considering case histories worldwide) and provided results that were much closer to random guessing as opposed to accurate predictions. This highlights the inherent difficulty of predicting what is *below* the ground using only information from *above* the ground. Efficient geospatial models may be developed for certain locales, but the development of a single model that efficiently predicts subsurface traits across various seismological, geological, geomorphic, and climatic settings is inherently challenging. Given these findings, the global "portability" of geospatial models must be improved and considered a future research priority. Results from the testing of geotechnical vs. geospatial models provide useful insights for model improvement. Specific lessons and pathways for achieving these improvements are presented herein.

3. Functions to predict infrastructure damage and loss using geospatial models are presented. These functions are detailed within the report and were developed for several specific types of shallow foundation and for several specific modes of foundation failure. In addition, functions combining all foundation types and all modes of failure were developed. These broadly applicable functions do not require asset-specific information (i.e., the specific type of foundation) and attempt to predict the severity of damage independent of the associated failure mode. Although these functions may be more desirable for general, region-scale analyses, the performance/utility of the developed functions is generally poor, regardless of whether asset-specific information is available. This may be attributable to the fact that some failure modes appear to be strongly dependent on "meso-scale" details (e.g., building geometry, construction quality, subsurface variability, etc.) that are inadequately captured by "macro-scale" geospatial data. The functions developed herein to predict loss are especially ineffective, due to accurate loss prediction being strongly dependent on accurate damage prediction.

4. Lastly, considering (a) the relatively poor performance of geospatial models globally; (b) the relative inability of the models to predict the consequences of

liquefaction (even when the models efficiently predict liquefaction); (c) the primary applications of the models (e.g., post-earthquake reconnaissance and response; regional simulations); and (d) the seminal state of geospatial model-development, it is the authors' opinion that near-term investment should focus on model improvement rather than model extension. Research that improves the capacity of geospatial models to predict liquefaction (e.g., via development of new models or modification of existing models) is likely to be more impactful than research to adapt existing models for prediction of downstream consequences. Although geospatial liquefaction models have demonstrated surprising and provocative potential, there remains significant room for improvement.

ACKNOWLEDGMENTS

Any opinions, findings, and conclusions or recommendations expressed in this material are those of the authors and do not necessarily reflect those of the Pacific Earthquake Engineering Research Center (PEER) or the Regents of the University of California.

CONTENTS

LIST OF TABLES

LIST OF FIGURES

PREFACE

This report is presented in three parts. Part One details liquefaction case-history data newly compiled from three earthquakes in Canterbury, New Zealand, the quantity of which exceeds that obtained from all other earthquakes combined. The data is presented in a dense array structure, allowing researchers to easily access and analyze a wealth of information pertinent to free-field liquefaction response. The methods used to obtain and process the case-history data are detailed, as is the structure of the compiled file. Recommendations for analyzing the data are outlined, including nuances and limitations that users should carefully consider. Part Two presents a rigorous field assessment of liquefaction prediction models based on geotechnical vs. geospatial data. The compilation and analysis of more than 15,000 liquefaction case-histories from 24 earthquakes provides a baseline for model performance and elucidates pathways for model improvement (e.g., when geospatial models perform poorly, can the geotechnical data tell us why?). Part Three addresses the extension of geospatial models for predicting the severity of liquefaction ejecta; magnitude of ground settlement; and infrastructure damage and loss, specifically for infrastructure founded on shallow foundation systems. By synthesizing insights gleaned from Parts Two and Three, overall conclusions are presented, followed by recommendations for future research investment.

1 CPT-Based Liquefaction Case Histories from Three Earthquakes in Canterbury, New Zealand

Earthquakes occurring over the last decade in the Canterbury region of New Zealand have resulted in liquefaction case-history data of unprecedented quantity. This provides the profession with a unique opportunity to advance the prediction of liquefaction occurrence and consequences. Towards that end, this paper presents a curated dataset containing ~15,000 cone-penetration-test (CPT)-based liquefaction case histories compiled from three earthquakes that occurred in Canterbury. The compiled, post-processed data is presented in a dense array structure, allowing researchers to easily access and analyze a wealth of information pertinent to free-field liquefaction response (i.e., triggering and surface manifestation). Research opportunities using this data include, but are not limited to, the training or testing of new and existing liquefaction-prediction models. The many methods used to obtain and process the case-history data are detailed herein, as is the structure of the compiled digital file. Lastly, recommendations for analyzing the data are outlined, including nuances and limitations that users should carefully consider.

1.1 INTRODUCTION

Within the six years following the 4 September 2010 M_w7.1 Darfield earthquake, which triggered widespread liquefaction in the city of Christchurch, New Zealand, and its environs, 21 additional $M_w \geq 5$ earthquakes occurred within ~20 km of the city's center. While *some* liquefaction was observed in at least 10 of these events [Quigley et al. 2013], damaging liquefaction was most notably triggered by ruptures on 22 February 2011, 13 June 2011, 23 December 2011, and 14 February 2016. A comprehensive summary of the first three of these, including tectonic and geologic settings, seismology, and effects, is provided by Quigley et al. [2016]. Specific to liquefaction, observed consequences included: damage to low-, mid-, and high-rise structures, resulting in widespread loss of building stock (e.g., Cubrinovski et al. [2011]; van Ballegooy et al. [2014a]; and Bray et al. [2014]; failure of water, wastewater, power, and communications networks (e.g., O'Rourke et al. [2014]; Kwasinski et al. [2014]; and Tang et al. [2014]); loss of road, rail, bridge, and levee functionality (e.g., Green et al. [2011]; Wotherspoon et al. [2011]; and Cubrinovski et al. [2014]); and impairment of port infrastructure (e.g., Chalmers et al. [2013]).

These effects in a major urban center facilitated and motivated the collection of vast amounts of data, including seismologic, hydrologic, geospatial, and geotechnical measurements, much of which was uploaded to the open access Canterbury Geotechnical Database [CERA 2013], now the New Zealand Geotechnical Database [NZGD 2020]. These bulk, raw ingredients constitute the makings of an unprecedented quantity of liquefaction case histories, which can be used to train or test predictive models. While several "tiers" of liquefaction prediction models exist [Geyin et al. 2020], most prevalent models in practice are based on *in situ* geotechnical tests, among which the cone-penetration-test (CPT) has important advantages [NRC 2016]. Although such models are widely used to predict liquefaction, to date they have been trained on relatively modest datasets. For example, the CPT-based liquefaction triggering model of Boulanger and Idriss [2014], when developed, was trained on essentially all published case histories from all earthquakes combined, or 255 datapoints.

This study described within has compiled a curated digital dataset of approximately 14,500–15,500 CPT-based case histories from three earthquakes in Canterbury—namely, the September 2010 M_w 7.1, Feb. 2011 M_w6.2, and February 2016 M_w5.7 earthquakes—with the exact total depending on criteria discussed subsequently. The post-processed data is presented in a structure array (i.e., a single file), allowing researchers to readily access and analyze a wealth of information pertinent to free-field liquefaction response. As shown in Figure 1.1, this considerably augments the data available for model training and testing (by at least 50 times), presenting the profession with a unique opportunity to advance the science of liquefaction prediction.

Chapter 1 is an introduction to the data compilation program.

Chapter 2 describes the methodology involved in compiling this curated database. The methods used to obtain, process, and populate the database are first detailed, with each "datapoint," including:

- identifying information (e.g., geographic coordinates);
- processed CPT data, both with and without inverse-filtering and interface correction [Boulanger and DeJong 2018];
- peak ground acceleration (PGA) and earthquake magnitude (M_w);
- groundwater table (GWT) depth; and
- the classified occurrence and severity of liquefaction manifestation at the ground surface, with explicit focus on free-field level ground sites.

The structure and formatting of the resulting data array are then discussed, following which recommendations for analyzing the data are given, including nuances, uncertainties, and limitations that users should carefully consider

Chapter 3 presents a rigorous field assessment of liquefaction prediction models based on geotechnical vs. geospatial data using the outputs of Chapter 2. Chapter 4 addresses the extension of geospatial models for predicting the severity of liquefaction ejecta; magnitude of ground settlement; and infrastructure damage and loss, specifically for infrastructure founded on shallow foundation systems. Synthesizing insights gleaned from Chapters 3 and 4, overall conclusions are then presented, followed by recommendations for future research investment.

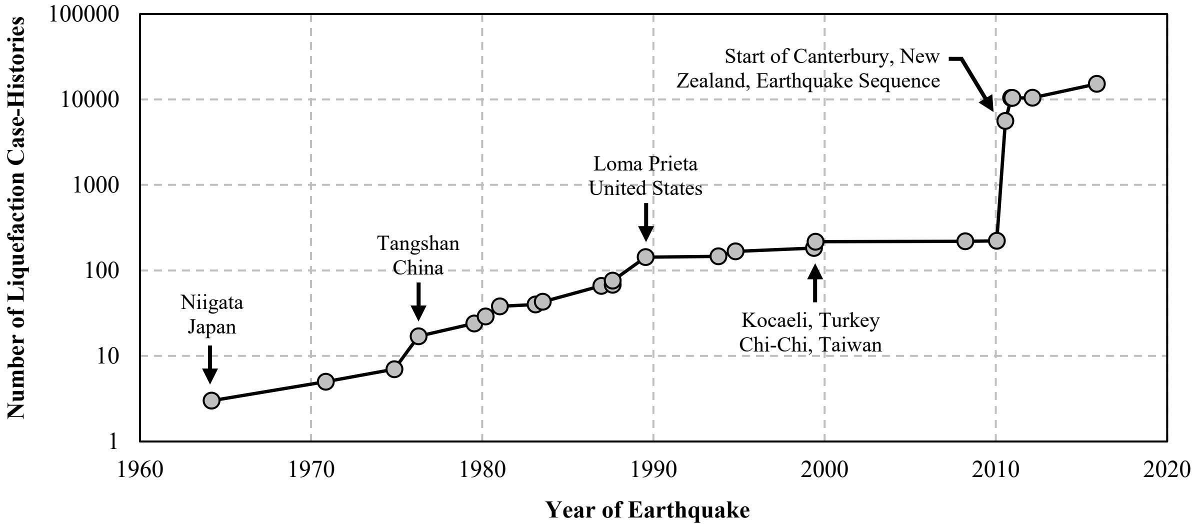

Figure 1.1 Chronology of CPT-based case histories, as compiled by Geyin et al. [2020].

2 Part One: Case History Compilation

Case histories were compiled from the September 2010 M_w7.1, February 2011 M_w6.2, and February 2016 M_w5.7 earthquakes. This effort built upon successive compilations [Maurer et al. 2014; 2015b], augmenting the largest by more than 50%. While data could potentially also be compiled from the aforementioned events of 13 June and 23 December 2011, these events are complicated by the occurrence of multiple, similar-magnitude ruptures only minutes-to-hours apart [Bradley 2016]. As a result, reconnaissance captured the compounded effects of multiple events (complicating observations of response) and pore pressures were elevated at the start of latter events (complicating predictions of response). We thus choose not to present these data, focusing instead on three events without this obfuscating circumstance.

2.1 CPT DATA AND PROCESSING

The CPT data was obtained from the New Zealand Geotechnical Database [NZGD 2020] at sites where liquefaction manifestations could be reliably classified. During this process, CPTs were rejected if inferred from geospatial autocorrelation analyses [Anselin 1995] to have terminated prematurely (e.g., due to impedance from gravel), such that liquefiable soils potentially exist at greater depth. The local geology of Christchurch is well characterized, with dense, non-liquefiable soils typically found at a certain depth and unlikely to be underlain by looser soils that contribute to liquefaction hazard. In particular, beach, estuarine, and coastal swamp sediments were deposited across Christchurch as the sea level rose during the late Pleistocene and Holocene, reaching a peak ~6,500 years before present, with the coastline located 1–2 km west of the present-day city center [Brown et al. 1995]. Since then, alluvial deposition has resulted in progradation of the coast to its present location [Brown et al. 1995]. Collectively, the deposits resulting from coastline transgression and progradation are known as the Christchurch formation and overlay Pleistocene gravels (i.e., the Riccarton Gravel formation). The terrestrial thickness of the Christchurch formation is greatest beneath the present-day coastline and tapers from east to west, terminating around the mid-Holocene coastal highstand, beyond which the surface geology is characterized by the Springston formation of alluvial gravels and sands [Begg and Jones 2012]. Thus, where the Springston formation dominates (and in some areas of the Christchurch formation), gravelly soils force CPT termination at shallow depth (< 20 m).

Figure 2.1 maps the expected, surficial geologic units as described in Table 2.1, and the locations and termination depths of CPT soundings. The termination-depth trends shown in Figure

2.1(b) generally agree with the known geologic profile, such that these depths diminish from east to west. While the possibility of liquefiable soils at greater depths exists, it was assumed for this study that their limits are generally defined by CPT termination depths. However, the database was first parsed using an Anselin Local Morans I analysis [Anselin 1995] to identify and remove outliers with sounding depths statistically less than the spatial average (i.e., soundings more likely to have prematurely terminated before reaching the Riccarton Gravel formation).

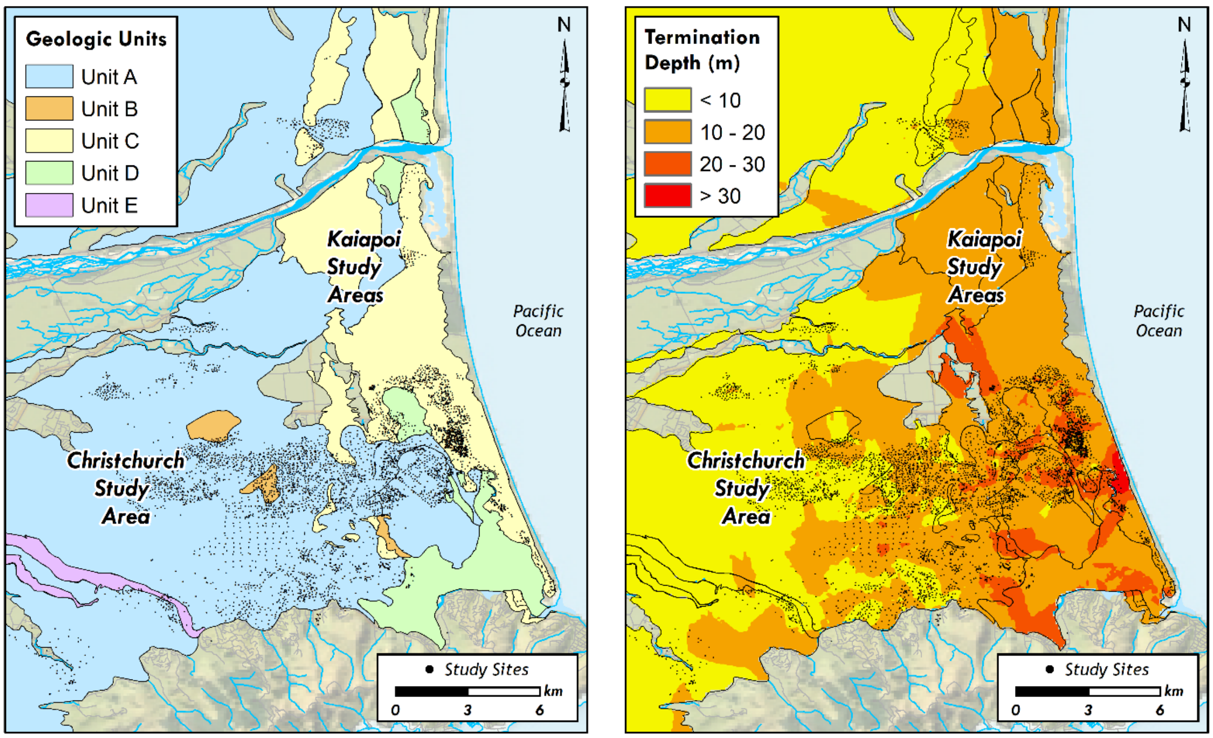

(a) (b)

Figure 2.1 **Case-history locations in context of: (a) surifical geologic units, as described in Table 1.1; and (b) CPT sounding termination depths.**

Table 2.1 Surficial geologic units of study area.

Geologic unit	Description	Source	Percent (%) of CPTs in units
A	Alluvial sand and silt of overbank deposits	Brown [1975]	59.39
B	Peat swamps now drained	Brown and Weeber [1992]	2.24
C	Fixed dune sand and beach deposits	Brown [1975]	35.34
D	Saline sand, silt and peat of drained lagoons and estuaries	Brown and Weeber [1992)	2.26
E	Fluviatile gravel, sand, and silt of historic river flood channels	Brown and Weeber [1992]	0.43

While the CPT offers advantages among *in situ* tests used to predict liquefaction, it is still limited by the volume of soil mobilized around the cone. As an intermediate-to-large-strain penetration test, this mobilized zone acts as a physical "low-pass filter" on the true soil stratigraphy, removing information from the low spatial wavelengths, such as the data defining a thin soil stratum or the interface between two disparate soils. These spatial smoothing effects, which are commonly referred to as "thin layer" and "transition" effects, have long been recognized and studied (e.g., Treadwell [1976]; Lunne et al. [1997]; Ahmadi and Robertson [2005]; Robertson [2011]; and van der Linden [2016]). While chart-based methods exist for manually correcting these effects on CPT data, Boulanger and DeJong [2018] proposed the first programmable procedure. This methodology, referred to as an "inverse filtering and interface detection" procedure, predicts the "true" CPT profile from measured CPT values. Since these measured values reflect a filtered view of reality, their correction would improve subsurface characterization. As a demonstration of the methodology, CPT data from Christchurch is shown in Figure 2.2, both with and without correction.

While the performance of Boulanger and DeJong's [2018] procedure is currently being evaluated (see Yost et al. [2020]), its use can change a site's perceived liquefaction hazard, with the direction and magnitude of change dependent on numerous factors. Considering this potential influence, and that the Boulanger and DeJong [2018] procedure might prove to be efficacious, both measured and "true" CPT data are provided in the database. While the reader is referred to Boulanger and DeJong [2018] for complete details, the procedure's "baseline" parameters were used to compute "true" CPT data. This was the case both for the methods that invert tip resistance and sleeve friction, and that which detects and corrects stratigraphic interfaces. Conceivably, these defaults can be calibrated via site-specific study (e.g., from borings adjacent to a CPT), but the information compiled for this study either was insufficient to attempt calibration or provided insufficient statistical support to justify it.

As part of the processing methodology, CPT tip- and sleeve-measurements were aligned using statistical cross-correlation [Buck et al. 2002], both for measured and "true" CPT data. In addition, CPT data was infilled in the "pre-drill" zone (i.e., where borings were used to safety bypass pavements or utilities, most often to a depth of ~1 m where applicable (~40% of CPTs were pre-drilled). In the absence of this correction, the recorded data is that of noise as the cone penetrates an open boring. Accordingly, CPT data was sampled 15 cm beyond the recorded depth of pre-drill, then uniformly applied to the pre-drill interval. While this provides reasonable data for approximating soil unit weights, and, by corollary, *in situ* stresses below the pre-drill zone, users should consider the relative depths of pre-drill and groundwater when analyzing case histories, as discussed herein. As part of this process, CPTs with unknown pre-drill depth were preemptively removed from the dataset, as were CPTs with pre-drill depth exceeding 2.5 m. All CPT processing was completed using the open-source software *Horizon* [Geyin and Maurer 2020].

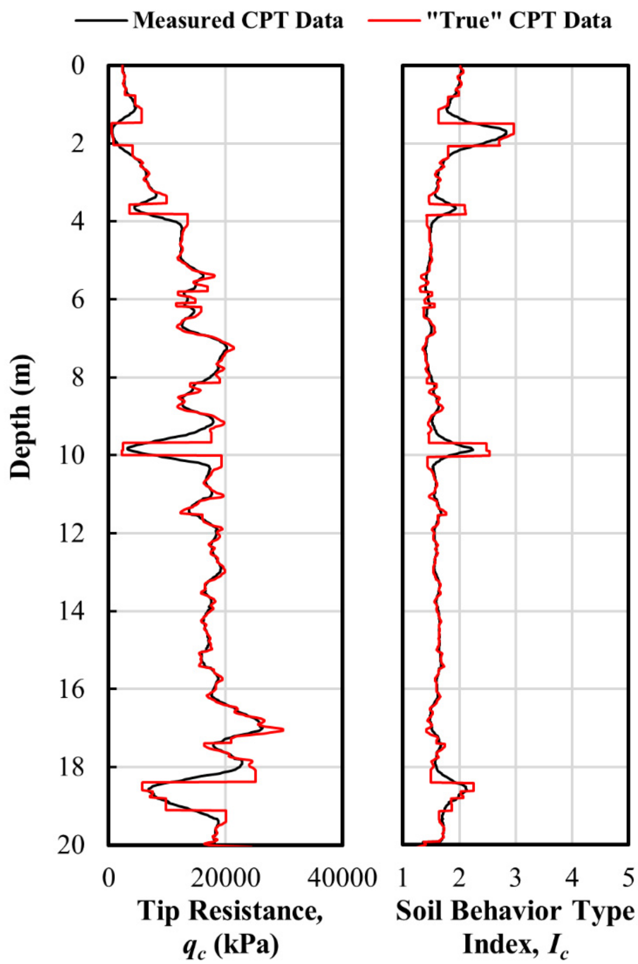

Figure 2.2 Example CPT with (i.e., "true") and without (i.e., "measured") inverse-filtering and interface correction via the Boulanger and DeJong [2018] method, as implemented in the software Horizon [Geyin and Maurer 2020].

2.2 LIQUEFACTION MANIFESTATIONS

Emphasis was placed on compiling case histories from free field level-ground sites, with the occurrence and severity of surface manifestation defined primarily by liquefaction ejecta. In this respect, sites with other indicators of liquefaction (e.g., evidence from ground-motions or foundation settlements) were expressly omitted. While ~7% of case histories were characterized by a predominance of lateral spreading, the majority were compiled from level-ground sites. In particular, surface manifestations were observed at CPT sites following at least one of the three aforementioned earthquakes and manually classified by the authors as "none," "marginal," "moderate," "severe," "lateral spreading," or "severe lateral spreading" using criteria modified from Green et al. [2014] and given in Table 2.2; the identifying codes assigned herein to each classification are also provided. This was accomplished using high-resolution satellite imagery and reconnaissance reports available in the NZGD [2020]. Classifications were based on a circular sample area centered on each CPT, with approximate radius of 15 m. Sites where surface manifestations could not be reliably classified following an event are denoted as "unknown" and coded "10" (i.e., sites where manifestations were classified following at least one earthquake, but not all three, which was the case for ~18% of study sites). Of the resulting 15,890 compiled case histories, 61% were classified as "none" and 39% are cases in which manifestations were observed and classified in accordance with Table 1.2. Owing to nuances that will be discussed subsequently, the quantity of data best suited for model training and testing is ultimately reduced to ~14,500–15,500 cases.

Table 2.2 Criteria used to classify liquefaction manifestations (after Green et al. [2014]).

Classification	Severity ID	Criteria
None	0	No observed liquefaction ejecta or lateral spreading
Minor	1	Small, isolated liquefaction features less than a vehicle width; < 5% of ground surface is covered by ejecta; no lateral spreading.
Moderate	2	Groups of liquefaction features greater than a vehicle width; 5–40% of ground surface is covered by ejecta; streets are generally passable; no lateral spreading.
Severe	3	Adjoining large liquefaction features that are greater than a vehicle width; > 40% of ground surface is covered by ejecta; streets are generally impassable; no lateral spreading.
Lateral spreading	4	Ejection of liquefied material at the ground surface may be observed, but lateral spreading is the predominant manifestation and damage mechanism of liquefaction. Measured crack-displacement widths are less than 200 mm.
Severe lateral spreading	5	Ejection of liquefied material at the ground surface may be observed, but lateral spreading is the predominant manifestation and damage mechanism of liquefaction. Measured crack-displacement widths exceed 200 mm.
Unknown	10	Insufficient information to reliably classify: out of bounds, no reliable documentation, obscured or otherwise ambiguous imagery.

2.3 HYDROLOGIC DATA

The GWT depths at CPT locations were obtained from the time-dependent models of van Ballegooy et al. [2014b]. These models, which reflect seasonal and local fluctuations across the region, were derived in part using long-term monitoring data from a network of ~1000 monitoring wells and provide a best estimate of GWT depths at the time of each earthquake. LiDAR Digital Elevation Models and physical surveys were used to correct well measurements for elevation changes caused by the earthquakes. River and coastline data were used to shape and position GWT contours at places of significant groundwater-surface water interaction [van Ballegooy et al., 2014b]. The median GWT diminishes from 10+ m elevation (relative to sea level) west of Christchurch to less than 1-m elevation in the eastern suburbs (i.e., near the coast), which were roughly consistent with the change in ground elevation. The GWT depth is generally 1–2.5 m beneath much of the study area but reaches 5 m west of the city center. A histogram of GWT depth for all compiled case histories is shown in Figure 2.3(a).

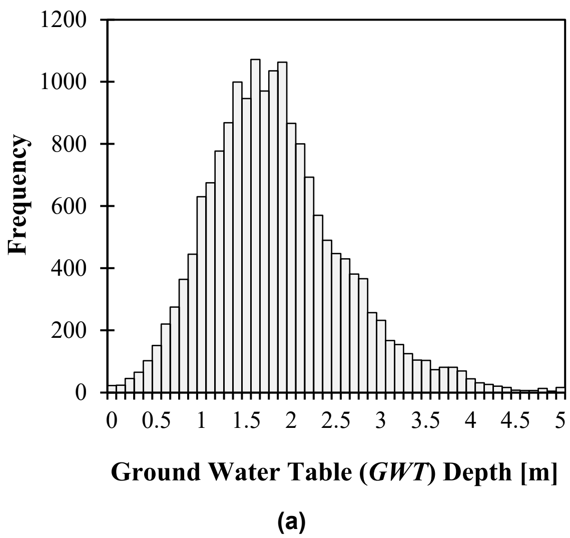

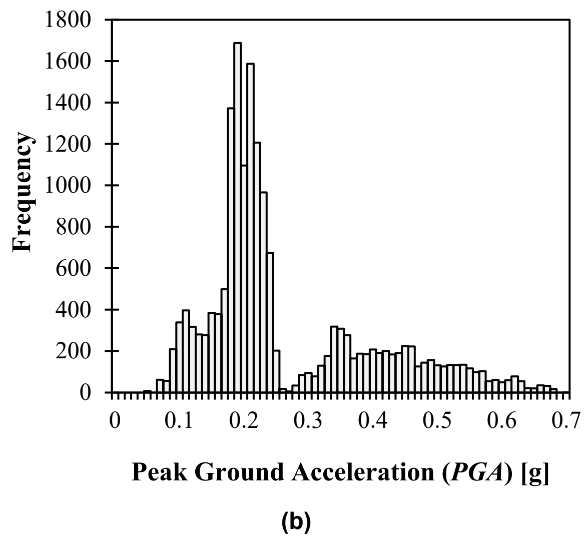

Figure 2.3 **Histograms of: (a) ground water table depth; and (b) peak ground acceleration for case histories compiled in the curated dataset.**

2.3.1 Peak Ground Accelerations

To date, peak ground acceleration (PGA) is the most common ground-motion intensity measure (IM) for quantifying seismic demand in liquefaction models. Among other standard IMs, it has been shown to be the most efficient predictor of pore-pressure generation and the initiation of liquefaction [Sideras 2019]. In this study, PGAs were estimated at CPT sites via the Bradley [2014] method, which has been used widely in research related to the Canterbury earthquakes (e.g., van Ballegooy et al. [2015]; Geyin et al. [2020]; and Geyin and Maurer [2021]). This method geostatistically coalesces instrumentally recorded PGAs with predictions from ground-motion models (GMMs), where the former were recorded by more than 20 near-source strong-motion stations (SMS) (e.g., Bradley and Cubrinovski [2011] and Bradley [2012]. Using this approach, the PGA at SMS, *i*, is expressed as:

$$\ln(\mathrm{PGA}_i) = \mu_{\ln \mathrm{PGA}_i}(\mathrm{Site}, \mathrm{Rup}) + \eta + \varepsilon_i \, , \tag{2.1}$$

where ln(PGA$_i$) is the natural logarithm of the observed PGA at SMS i; $\mu_{\ln \mathrm{PGA}_i}(\mathrm{Site}, \mathrm{Rup})$ is the mean of the natural logarithm of PGA at SMS i predicted by a GMM, which is a function of site and rupture parameters; η is the inter-event residual; and ε_i is the intra-event residual. Within Equation (2.1), a GMM predicts a PGA distribution:

$$\ln(\mathrm{PGA}_i) \sim N(\mu_{\ln \mathrm{PGA}_i}, \sigma_\eta^2 + \sigma_\varepsilon^2) \tag{2.2}$$

where $X \sim N(\mu_X, \sigma_X^2)$ is shorthand notation for X having a normal distribution with mean, μ_X, and variance, σ_X^2. By definition, all PGAs recorded in a given earthquake have the same interevent residual, η. Conversely, the intraevent residual, ε_i, varies from site to site but is correlated spatially due to similarities in path and site effects. Accordingly, PGAs at SMS locations can be used to compute conditional distributions of PGAs at CPT locations.

First, the Bradley [2013] New Zealand GMM was used to compute the unconditional distribution of PGAs at SMS locations. A mixed-effects regression was then used to determine the inter-event residual, η, and the intraevent residuals, ε_i's, for each strong-motion station (e.g., Abrahamson and Youngs [1992]; Pinheiro et al. [2008]). Second, the covariance matrix of intra-event residuals was computed by accounting for the spatial correlation between SMS locations and a test site of interest. The joint distribution of intra-event residuals at a site of interest and the SMS is given as:

$$\begin{bmatrix} \varepsilon^{\mathrm{site}} \\ \varepsilon^{\boldsymbol{SMstation}} \end{bmatrix} = N\left(\begin{bmatrix} 0 \\ \mathbf{0} \end{bmatrix}, \begin{bmatrix} \sigma^2_{\varepsilon^{\mathrm{site}}} & \boldsymbol{\Sigma_{12}} \\ \boldsymbol{\Sigma_{21}} & \boldsymbol{\Sigma_{22}} \end{bmatrix} \right) \tag{2.3}$$

where $X \sim N(\boldsymbol{\mu_X}, \Sigma)$ is shorthand notation for X having a multivariate normal distribution with mean $\boldsymbol{\mu_X}$ and covariance matrix Σ (i.e., same as above, but in vector form, with bold denoting vectors or matrices); and $\sigma^2_{\varepsilon^{\mathrm{site}}}$ is the variance of the intraevent residual at the site of interest. In Equation (2.3), the covariance matrix has been expressed in a partitioned fashion to elucidate the subsequent computation of the conditional distribution of $\varepsilon^{\mathrm{site}}$. The individual elements of the covariance matrix were computed from:

$$\Sigma(i,j) = \rho_{i,j} \sigma_{\varepsilon i} \sigma_{\varepsilon j} \tag{2.4}$$

where $\rho_{i,j}$ is the spatial correlation of intraevent residuals between two locations i and j; and $\sigma_{\varepsilon i}$ and $\sigma_{\varepsilon j}$ are the standard deviations of the intraevent residual at locations i and j. Based on the joint distribution of intraevent residuals given by Equation (2.3), the conditional distribution of $\varepsilon^{\mathrm{site}}$ was computed from Johnson and Wichern [2007]:

$$\varepsilon^{\text{site}} \big| \varepsilon^{\textit{SMstation}} = N\left(\Sigma_{12} \cdot \Sigma_{22}^{-1} \cdot \varepsilon^{\textit{SMstation}}, \sigma^2_{\varepsilon^{\text{site}}} - \Sigma_{12} \cdot \Sigma_{22}^{-1} \cdot \Sigma_{21} \right) = N\left(\mu_{\varepsilon^{\text{site}} | \varepsilon^{\textit{SMstation}}}, \sigma^2_{\varepsilon^{\text{site}} | \varepsilon^{\textit{SMstation}}} \right) \quad (2.5)$$

Using the conditional distribution of the intraevent residual given by Equation (2.5) and substituting into Equation (2.2), the conditional distribution of PGA at a site of interest, PGA_{site}, is:

$$\left[\ln \text{PGA}_{\text{site}} \big| \ln \text{PGA}_{\text{SMstation}} \right] = N\left(\mu_{\ln \text{PGA}_i} + \eta + \mu_{\varepsilon^{\text{site}} | \varepsilon^{\text{SMstation}}}, \sigma^2_{\varepsilon^{\text{site}} | \varepsilon^{\text{SMstation}}} \right) \quad (2.6)$$

That is, the conditional distribution of PGA at a site is a lognormal random variable completely defined by the conditional median and conditional uncertainty (i.e., lognormal standard deviation). Intuitively, in cases where a CPT is located far from any SMS, the conditional distribution (i.e., final estimate of PGA) is similar to the unconditional distribution (i.e., GMM estimate of PGA), and for a CPT very near to a SMS, the conditional distribution approaches the value observed at the SMS. The conditional median and conditional uncertainty of PGA were computed at CPT sites using the spatial correlation model of Goda and Hong [2008]. Both are given in the dataset. A histogram of these median PGA values for all case histories is shown in Figure 2.3(b).

2.4 DATA STRUCTURE

The compiled post-processed data is presented in a structure array (i.e., a single file), with each case history that includes: identifying information (e.g., ID, geographic coordinates); CPT data, both with and without inverse-filtering and interface correction; earthquake magnitude (M_w); the median and uncertainty (i.e., lognormal standard deviation) of the conditional PGA; GWT depth; and the classified occurrence and severity of surficial liquefaction manifestation.

The curated dataset is available via the NHERI DesignSafe Cyber-Infrastructure data depot at *https://doi.org/10.17603/ds2-tygh-ht91* and provided in both Matlab data format and as a python data frame. The data fields, classes, contents, and their units are described in Table 2.3 and its accompanying footnotes. The structure of the data array is depicted in Figure 2.4 and arranged such that case histories are principally sorted by a CPT identification (ID) number, wherein multiple liquefaction case histories may be accessed. Event-specific data fields (e.g., M_w and PGA) are 3×1 arrays containing information from the 2010, 2011, and 2016 earthquakes, respectively. The CPT measurements, which are depth-dependent but not event-specific, are $l_i \times 1$ arrays, where l_i is the length of CPT i. Other fields include CPT ID, geographic coordinates, pre-drill depth, and test date. Recommendations for analyzing these data are discussed next, including important nuances and limitations that users should consider prior to analysis.

Table 2.3 Data fields, typologies, descriptions, and units.

Field	Class	Content
ID	cell	[1]CPT identifier for reference
CPTname	char	Name of the CPT
FILEname	char	Name of the CPT
Date	datetime	Date CPT conducted
NorthingNZMG	double	NZMG – y coordinate
EastingNZMG	double	NZMG – x coordinate
NorthingWGS84	double	WGS – y coordinate
Easting WGS84	double	WGS – x coordinate
depth	double	Depth below the ground surface [m]
qc	double	Measured tip resistance [kPa]
qc_inv	double	[2]True tip resistance [kPa]
fs	double	Measured sleeve friction resistance [kPa]
fs_inv	double	[2]True sleeve friction resistance [kPa]
u2	double	CPT pore pressure measurement, if present [kPa]
pd	double	Pre-drill depth [m]
Magnitude	struct	[3]Earthquake moment magnitude (M_w)
PGA	struct	[3]Event-specific conditional median peak ground acceleration (g)
PGAsigma	struct	[3]Event-specific conditional uncertainty of peak ground acceleration (g)
GWT	struct	[3]Event-specific groundwater table depth (m)
Manifestation	struct	[3,4]Classified type/severity of surface manifestation

[1]CPT IDs from original CPT data (.csv or .xlsx files; identifiers recorded by the field engineers).

[2]Processed per the Boulanger and DeJong [2018] procedure; specifically, using the "baseline" inversion model.

[3]There are three earthquakes within the fields from which event-specific data is compiled: M_w7.1 4 September 2010 (Yr2010), M_w6.2 22 February 2011 (Yr2011), and M_w5.7 14 February 2016 (Yr2016).

[4]The occurrence/severity of surface manifestation was manually classified for each CPT location in each earthquake per the criteria in Table 1.2. Classifications are based on a circular sample area, centered on each CPT, with approximate radius of 15 m.

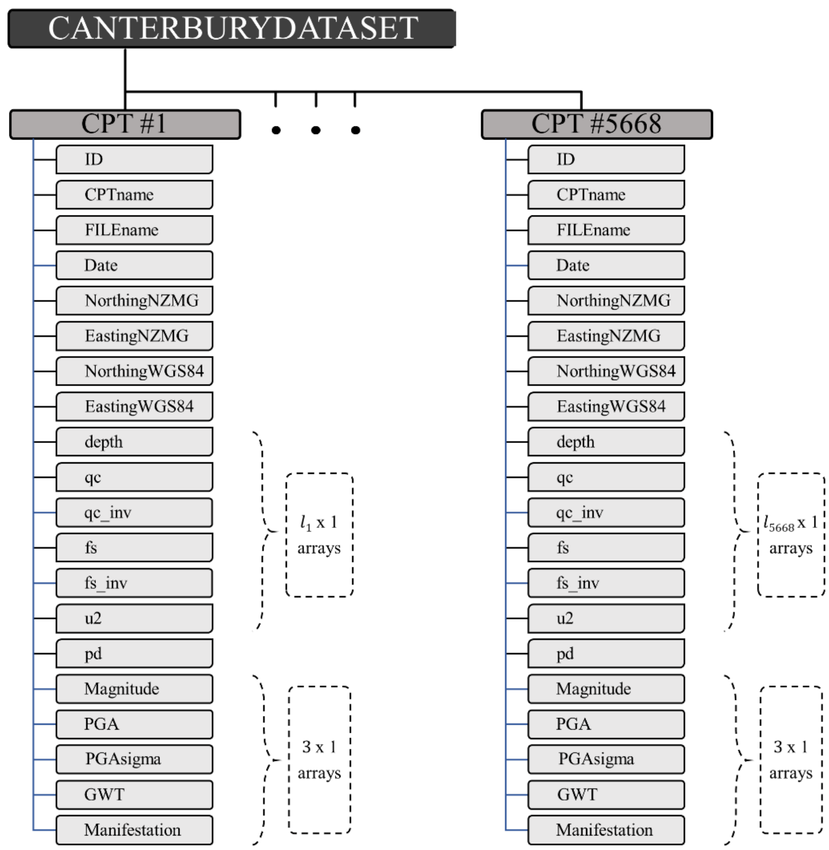

Figure 2.4 Depiction of the Canterbury case-history dataset structure array.

2.5 DISCUSSION: DATA NUANCES, ALTERNATIVES, AND ANALYSIS

The compiled, post-processed data allows researchers to easily access and analyze a wealth of information pertinent to *in situ* site characterization and free-field liquefaction response (i.e., triggering and surface manifestation). Research opportunities using this data include but are not limited to:

(i) methods for quantifying/simulating subsurface spatial variability;

(ii) training or testing of new and existing liquefaction-prediction models;

(iii) temporal assessment of CPT data during shaking sequences, including use of aging-correction factors for liquefaction prediction (i.e., K_{DR}); and

(iv) evaluation of CPT inversion filters in the context of liquefaction model performance.

Prior to such analyses, however, users should carefully consider several important data nuances, alternatives, and limitations. These topics are discussed as follows and ordered by:

(i) additional data exclusion criteria;

(ii) alternative sources of data;

(iii) correlations and decisions for analysis; and

(iv) lingering uncertainties.

2.5.1 Additional Data Exclusion Criteria

GWT and CPT Pre-Drill Depths

As discussed previously, CPTs where the pre-drill depth exceeded 2.5 m were preemptively removed from the dataset. For the remainder of CPTs, the pre-drill interval (typically ~1 m when present) was infilled with CPT data from just below the pre-drill (i.e., where the sensors began penetrating undisturbed soil). While this provides reasonable data for estimating *in situ* stresses, users performing liquefaction studies should consider the relative depths of pre-drill and groundwater. Case histories in which the depth of pre-drill exceeds that of the groundwater have additional uncertainty, given that CPT data below the expected water table is extrapolated rather than measured. A histogram of the GWT depth minus pre-drill depth is shown in Figure 2.5 for the 15,890 compiled case histories. Of these, 1503 have pre-drill depth exceeding the GWT depth; however, this differential exceeds 0.5 m for just 420 cases and exceeds 1 m for just 52 cases. Nonetheless, analysts might exclude some or all such cases to avoid near-surface site-characterization uncertainty. For example, some 1D liquefaction manifestation models are especially sensitive to this uncertainty owing to depth-weighting functions (e.g., Ballegooy et al., [2014a] and Maurer et al. [2015b]).

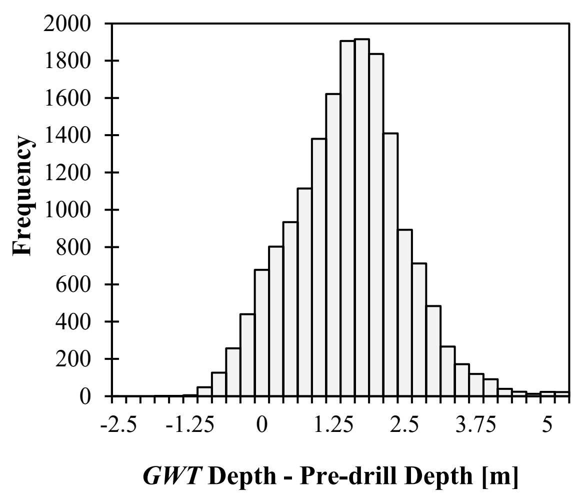

Figure 2.5 Histogram of ground water table depth minus pre-drill depth, for compiled case histories.

Peak Ground Accelerations

Profiles subjected to a PGA less than the expected threshold for inducing pore pressure [Dobry et al. 1982] might not provide meaningful data for testing liquefaction analytics. That is, if the expected peak strain is less than the volumetric threshold shear strain for a very loose soil, the absence of liquefaction is easily predicted by judgment. Using such cases to test liquefaction models could thus increase the prediction efficiency in a misleading manner. Accordingly, analysts might select a site-specific PGA threshold for excluding data or a general threshold considering the most susceptible soil that could be encountered (e.g., de Magistris et al. [2013]). Considering all compiled cases, 0.096*g* was the lowest PGA for which surface manifestation of liquefaction was observed, albeit this is distinctly different from that which may induce pore pressure at depth. Of the 15,890 compiled case histories, 98 had a PGA less than 0.075*g*; see Figure 1.4(b).

Model Applicability

Lateral spreading is a distinct manifestation of liquefaction influenced by topographic factors that were not compiled in this study, but which could be sampled (e.g., ground slope, distance to free face). However, users should consider whether such case histories are appropriate for model training or testing. As an example, 1D liquefaction manifestation models may not fully account for the factors known to cause lateral spreading, resulting in poor predictions (e.g., Maurer et al. [2015c] and Rashidian and Gillins [2018]). Thus, for some purposes, it may be most appropriate to exclude such cases from analysis. Of the 15,890 compiled case histories, 1110 were cases in which lateral spreading was the predominant manifestation of liquefaction. For further coverage of lateral spreading in Canterbury, see Cubrinovski and Robinson [2016].

2.5.2 Alternative Sources of Data

Ground Motions

As previously outlined, PGAs were obtained by statistically coalescing strong-motion records with GMM predictions [Bradley 2014], the general concept of which is common, and which could be used to obtain other IMs of interest. Notably, liquefaction likely occurred at some SMS sites during the Canterbury earthquakes, potentially effecting measured PGAs and, in turn, the adopted approach. In particular, evidence of liquefaction was observed in several SMS records from the 22 February 2011 earthquake (e.g., Bradley and Cubrinovski [2011]), namely: (i) high-frequency acceleration spikes, inferred to result from cyclic mobility/dilation response [Kramer et al. 2016]; and (ii) subsequent reduction in high-frequency motion, inferred to result from the softening of liquefaction [Kramer et al. 2016].

One such example is shown in Figure 2.6. It can be seen that a recorded PGA—if associated with a high-frequency dilation spike—could exceed the peak acceleration prior to liquefaction, and possibly that which would have occurred in its absence (i.e., from the time of liquefaction onward). Wotherspoon et al. [2015] identified four such SMS records (station codes CBGS, CCCC, NNBS, and REHS) and proposed reducing PGAs to those observed prior to interpreted dilation spikes. Adopting these values within a liquefaction analysis, Upadhyaya et al. [2019] suggested that existing prediction models performed slightly better when using the corrected values. However, given that liquefaction obscures SMS records following its onset, the "true" PGAs cannot be known. Whereas dilation spikes may inflate the PGA, selecting a peak value prior to any evidence of liquefaction may artificially depress it. Nonetheless, users should be aware of this issue.

Regardless of which PGAs are used within the adopted Bradley [2014] approach, they could be less accurate when complex local phenomena are not captured by empirical predictions (e.g., the effects of rupture directivity, basin-generated surface waves, and near-surface stratigraphic and topographic features). In contrast, physics-based simulations can provide insight into these phenomena via explicit modeling of kinematic fault rupture, wave propagation, and the subsurface velocity structure, thereby predicting IM patterns more accurately. Users may thus be interested in the physics-based simulations of Bradley et al. [2017], which predict both common IMs and full acceleration time series for each of the three earthquakes in the dataset. These may be obtained at case-history coordinates via the SeisFinder [2020] web portal.

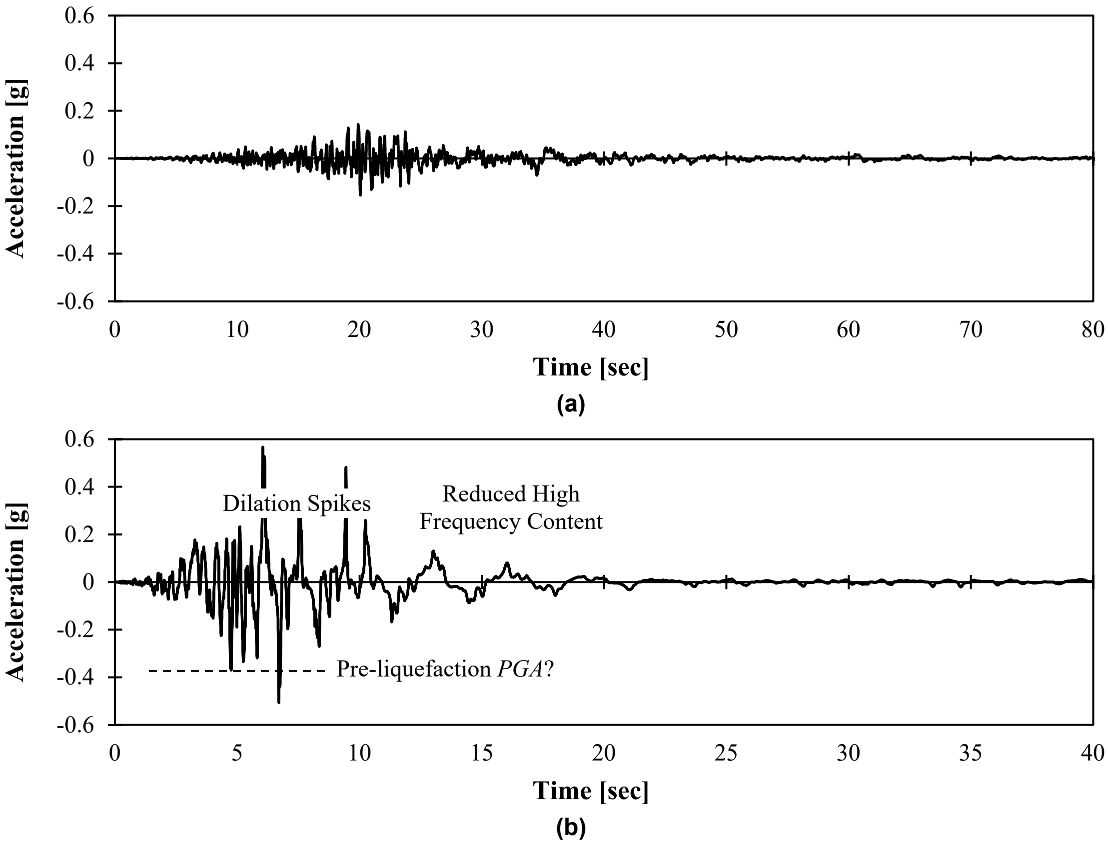

Figure 2.6 **Ground-motion records (SMS code NNBS) during the: (a) M_w7.1 September 2010 Darfield; and (b) M_w6.2 February 2011 Christchurch earthquakes, showing the effects of liquefaction on recorded PGAs.**

Liquefaction Manifestations

As previously discussed, surface manifestations were manually classified at individual CPT sites using a circular sample with 15-m radius. Inherent to this process, which required hundreds-to-thousands of hours to complete, sites where manifestations could not be reliably classified are denoted "unknown." These sites either lacked ground reconnaissance data, were beyond the bounds of high-resolution satellite imagery, had obscured or otherwise ambiguous imagery, or lacked sufficient and consistent information to support classification. Following a similar approach, but without concern for CPT locations or compiling case histories, Townsend et al.

[2016] presented GIS files for the September 2010 and February 2011 earthquakes wherein observed manifestations were mapped by polygon and assigned a confidence rating of "certain," "probable," "possible," or "uncertain." These polygons could supplement/replace the classifications made herein or could provide additional quality control. While Townsend et al. [2016] provide a high-quality dataset, caveats for use include:

> (i) polygons and ratings are for positive observations only (i.e., they do not explicitly delineate negative observations or assign the confidence therein, although a lack of liquefaction may be inferred where polygons are not present);
>
> (ii) the mapping does not classify the severity of liquefaction, which may be useful for model training/testing; and
>
> (iii) due to the scale of polygons (e.g., that of building parcels), a polygon may be classified as positive but lack manifestations over some or much of its surface area.

For these reasons, the classifications made herein may differ from those of Townsend et al. [2016]. Nonetheless, users should be aware of this excellent database and consider its use.

2.5.3 Correlations and Decisions for Analysis

Liquefaction Susceptibility

Existing "simplified stress-based" triggering models (e.g., Robertson and Wride [1998]; Moss et al. [2006]; Boulanger and Idriss [2014]; and Green et al. [2019]) are not intended to be applied to high plasticity, fine grained, "non-liquefiable" soils, which could result in less accurate predictions of cyclic response, and for which other, more appropriate methods exist (e.g., Boulanger and Idriss [2007]). Soils not susceptible to liquefaction triggering are thus generally identified and screened from analysis, consistent with the development of the models. Various criteria based on lab indices have been proposed for this purpose (e.g., Polito [2001]; Seed et al. [2003]; Bray and Sancio [2006]; and Boulanger and Idriss [2006]); an overview is given by Green and Ziotopoulou [2015]. However, while soil samples may be obtained using a CPT push-sampler, continuous sampling and testing to assess susceptibility is prohibitively expensive. For this reason, the CPT soil-behavior-type index (I_c)—proposed by Jeffries and Davies [1993] and modified by Robertson and Wride [1998]—is generally used to assess susceptibility by way of correlations with lab criteria. For example, an I_c = 2.6 threshold is common, such that soils with I_c < 2.6 are inferred to be liquefiable [Robertson and Wride 1998]. However, because I_c boundaries between soil types are approximate, regional refinement may be needed for optimal efficiency (e.g., Pease [2010]). Accordingly, analysts of the data compiled herein may be interested in the susceptibility correlations of Maurer et al. [2019], which were developed specifically for soils in Christchurch. Using these correlations, the probability that a soil is "susceptible" to liquefaction is:

$$P_{\text{susceptible}}\left(I_c\right) = 1 - \Phi\left[\frac{\ln\left(I_c/x_m\right)}{\beta}\right] \tag{2.7}$$

where Φ is the Gaussian cumulative distribution function; x_m is the median value of the distribution (the value of I_c corresponding to 50% probability); and β is the logarithmic standard deviation.

Using this form, Maurer et al. [2019] correlated I_c to four criteria based on Atterberg limits, the coefficients for which are provided in Table 2.4, and an example of which is shown in Figure 2.7. Here, "susceptible" generically refers to the varying definitions adopted by the respective works. For example, the Boulanger and Idriss [2006] criterion was explicitly developed to determine the most appropriate analysis procedure for predicting cyclic response based on whether the soil's expected behavior is "sand-like" or "clay-like." For deterministic analyses in which a single I_c threshold is desired, the median value of the probability distribution (x_m) is recommended, such that soils with I_c exceeding x_m are not susceptible per the underlying criterion.

Table 2.4 Model coefficients for I_c-susceptibility relationship (Eq 7) [Maurer et al. 2019].

Susceptibility criterion	β	x_m
Boulanger and Idriss [2006]	0.0851	2.5031
Polito [2001]	0.0988	2.5474
Seed et al. [2003]	0.1348	2.6214
Bray and Sancio [2006]	0.1275	2.7315

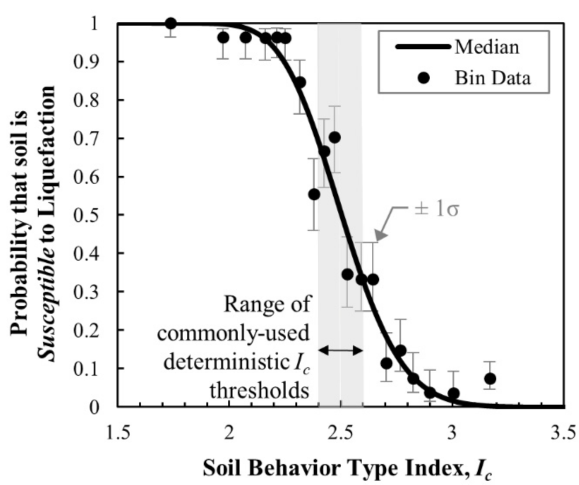

Figure 2.7 The probability of liquefaction susceptibility per the Boulanger and Idriss [2006] criterion as a function of measured I_c. The range of deterministic I_c thresholds common in practice is also highlighted [Maurer et al. 2019].

Fines Content

Some liquefaction models use fines content (FC) as a predictive variable. As with liquefaction susceptibility, FC is best measured directly, but continuous sampling and measurement is not feasible for a large CPT campaign. Accordingly, CPT correlations developed from global data are commonly used to estimate FC but can often be improved via regional calibration. Analysts testing or training response models may thus be interested in the regional I_c–FC correlations of Lees et al.

[2015a] and Maurer et al. [2019]. Lees et al. [2015a] calibrated the general I_c–FC correlation of Boulanger and Idriss [2014], wherein FC (%) is estimated as:

$$\mathrm{FC} = 80\left(I_c + \mathrm{C_{FC}}\right) - 137 \tag{2.8}$$

where $\mathrm{C_{FC}}$ is a calibration parameter that may adjust the general correlation (i.e., $\mathrm{C_{FC}} = 0$) to region-specific conditions. Analyzing 2600 FC measurements from Canterbury, Lees et al. [2015a] proposed that $\mathrm{C_{FC}} = 0.2$ was optimal. Using a similar amount of data but different processing and regression methods, Maurer et al. (2019) proposed that FC be estimated as:

$$\mu_{\mathrm{FC}} = 80.645 \cdot I_c - 128.5967 \tag{2.9}$$

where μ_{FC} is the mean estimate of FC (%), limited to 0% ≤ FC (%) ≤ 100%. Guidance on using this correlation probabilistically is given in Maurer et al. [2019]. A comparison of the Maurer et al. [2019] correlation and others, along with data from Christchurch, is shown in Figure 2.8.

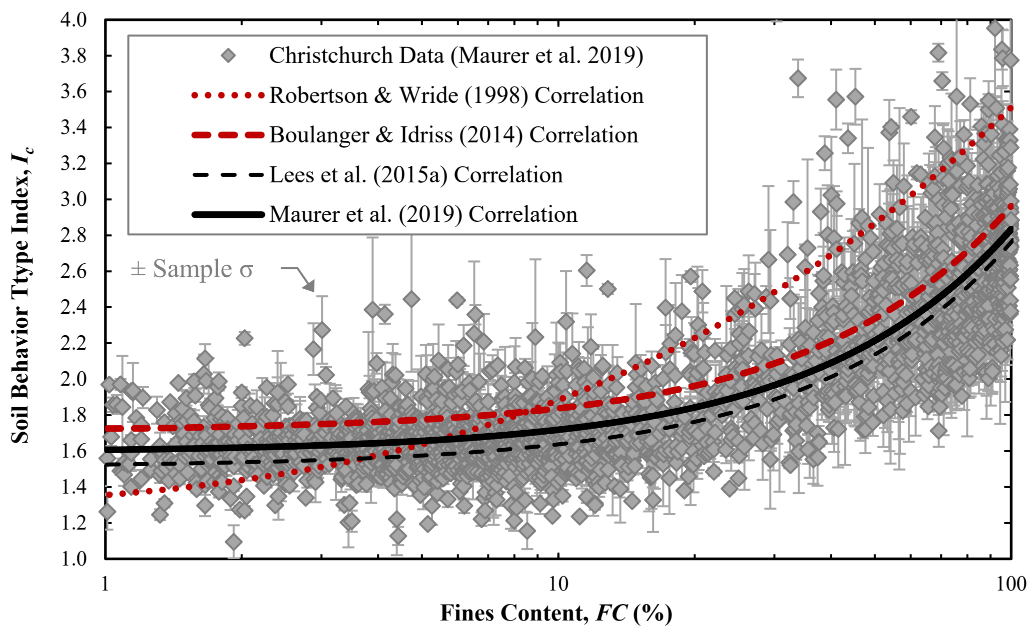

Figure 2.8 **Canterbury I_c—FC data and correlations [Lees et al. 2015a; Maurer et al. 2019], and comparison with the generic Robertson and Wride [1998] and Boulanger and Idriss [2014] correlations.**

Soil Density

Total and effective vertical stresses are integral to CPT data processing and a common input to liquefaction models. While the authors are unaware of calibrated, Canterbury-specific correlations for estimating soil unit weights, several global correlations are available, including Mayne et al. [2010] and Robertson and Cabal [2010], with the latter being used in previous Canterbury earthquake research by the authors (e.g., Green et al. [2018] and Geyin and Maurer [2019]). While liquefaction models may be relatively insensitive to the adopted correlation, users should consider constraints, as needed and reasonable, to limit physically indefensible values.

GWT at Time of Testing

As discussed, the database contains event specific GWT depths, which are an estimate of conditions immediately prior to each earthquake. These may be used to infer the depth of saturation for assessing liquefaction susceptibility (to be further discussed) but may differ from the GWT depths at the time of testing, which are needed for CPT stress-normalization as part of routine data processing. While regional hydrologic models are unavailable for CPT test dates, which are shown in Figure 2.9(a), most CPTs (~90%) were performed between 22 February 2011 and 30 September 2013. In addition, it can be seen in Figures 2.9(b) and (c) that GWT depths in February 2011 were typically ~1% shallower relative to September 2010 and ~14% deeper relative to February 2016. In the absence of more rigorous modeling, adopting a GWT depth either interpolated from the three estimates available, or simply averaged from the February 2011 and February 2016 values (since most CPTs were performed during this time), may provide a reasonable estimate for CPT stress normalization. Estimates could also be obtained from analyses of the CPT u2 data, although the reliability of this data due to issues with porous stone saturation, etc. is unknown for the compiled database.

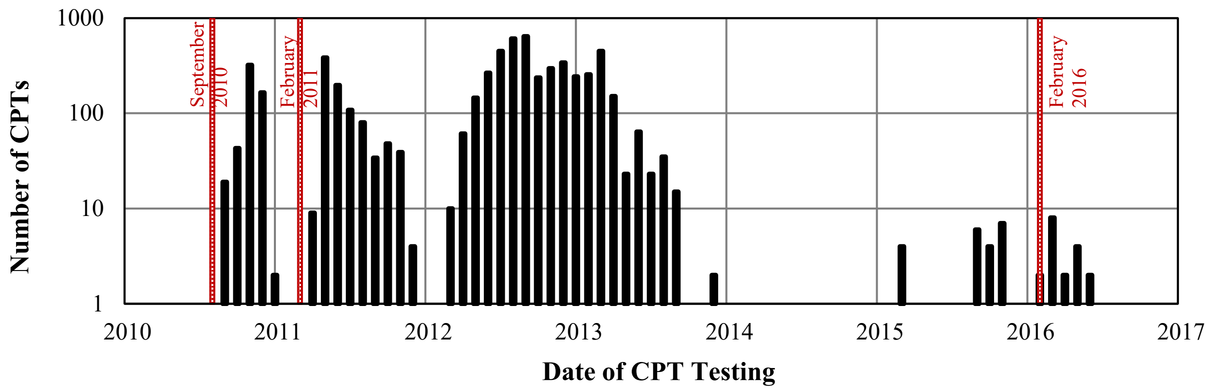

(a)

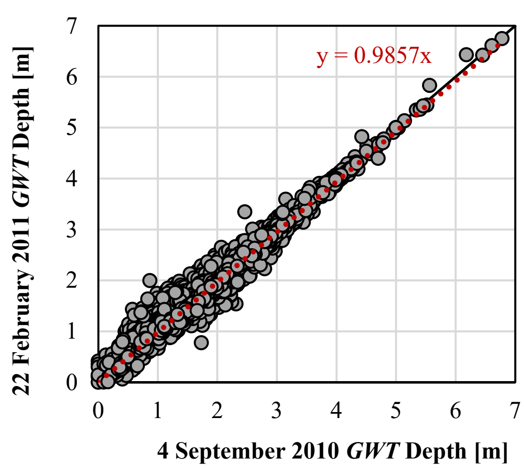

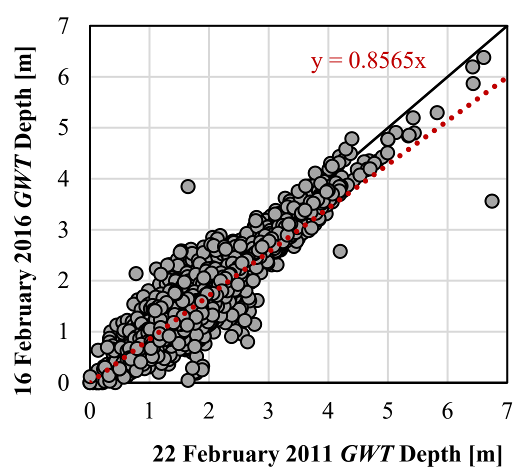

(b) (c)

Figure 2.9 Case-history database statistics: (a) monthly histogram of CPT test dates; (b) GWT depths from September 2010 versus February 2011; and (c) GWT depths from February 2011 versus February 2016.

Model Training, Testing, and Bias

Historically, publications proposing, calibrating, or evaluating liquefaction models often lack standard test metrics (e.g., Maurer et al. [2015d]), hindering quantifications and comparisons of model performance. Receiver-operating-characteristic (ROC) analyses (e.g., Fawcett [2006]) are ubiquitous in medical diagnostics and data science [Zou 2007], and increasingly, are being adopted in geotechnical modelling (e.g., Oommen et al. [2010]; Zhu et al. [2017]; Green et al. [2017]; and Upadhyaya et al. [2020]). The ROC analyses provide a standard and objective assessment of prediction efficiency via the area-under-the-ROC-curve (AUC) and are relatively insensitive to sampling imbalance (i.e., unequal positives and negatives). Analysts using the curated data to test or train liquefaction models should similarly adopt standard, objective, and repeatable measures of performance, be it ROC analyses or some other. In addition, while the Canterbury earthquakes resulted in a wealth of data, this data nonetheless samples the geologic and seismologic setting of one region, the findings from which may or may not translate elsewhere. Analysts should carefully consider sampling bias and weigh results from Canterbury with those from global case histories (e.g., Brandenberg et al. [2020]). Given that the compiled Canterbury database is much larger than that resulting from all other earthquakes combined, the finite-sample uncertainty of model performance should be computed for each respective database (e.g., via bootstrap sampling) and used to test for statistical significance. That is, to illustrate the sensitivity of performance to the data available for analysis and to assess whether differences could arise from chance (i.e., due to finite sampling), and not because one model is better than another. As an example, *p*-values specific to ROC analyses may be computed per DeLong et al. [1998], an application of which is presented in Geyin et al. [2020] for liquefaction case-history data.

2.5.4 Lingering Uncertainties

GWT Depth and Saturation

It is established that liquefaction resistance and degree of saturation are inversely related, all else being equal (e.g., Ishihara and Tsukamoto [2004] and Hossain et al. [2013]), and that soil beneath the apparent GWT can conceivably be less than 100% saturated (e.g., due to seasonal or tidal fluctuations, or to biologic activity). This phenomenon has been inferred from crosshole *p*-wave velocities [Cox et al. 2018] at select locations in Christchurch and investigated as a possible cause of observed mispredictions of liquefaction by popular models [McLaughlin 2017; Boulanger et al. 2018; Yost et al. 2019; and Ntritsos and Cubrinovski 2020].

One detailed study of this issue is that of McLaughlin [2017], who analyzed 31 cases in Christchurch and computed liquefaction potential index (LPI) values with and without various corrections. These included corrections for partial saturation, site-specific FC, and inverse filtering and interface correction. While evidence of partial saturation was found at some locations, the corrections to the LPI were typically minor compared to those made for FC and inverse filtering. The results of McLaughlin [2017] indicate that partial saturation beneath the GWT could potentially be important at some sites, but in general, does not sufficiently or consistently explain mispredictions of liquefaction. Nonetheless, uncertainties pertaining to partial saturation persist, but could only be adequately addressed via extensive additional *in situ* testing and/or regional hydrologic modeling. Owing to the rarity of *p*-wave measurements in parallel with CPTs, it is unknown whether partial saturation beneath the GWT is present in other case histories, previously collected elsewhere globally.

CPT Spacing in Time

As discussed, multiple case-histories were often developed from a single site (i.e., CPT) affected by multiple earthquakes, wherein the event-specific GWT, PGA, and response were known. This raises the question of whether a CPT performed at one moment in time [predominantly between February 2011 and September 2013; see Figure 2.9(a)] is representative of a soil profile at multiple other times when earthquakes occurred? This will be addressed in three parts.

First, does the approach taken break from precedent? When considering all liquefaction case histories published to date (e.g., Boulanger and Idriss [2014]), *in situ* testing has been performed:

(i) well in advance of an earthquake;

(ii) months-to-years after an earthquake;

(iii) decades after an earthquake; and

(iv) all scenarios in between.

Additionally, between the time of *in situ* testing and the occurrence of an earthquake, or between the time of the occurrence of an earthquake and *in situ* testing, it is often the case that multiple other earthquakes of varying intensity have affected a site. In the authors' opinion, there has historically been no standard or best practice for the relative timing of *in situ* testing when publishing liquefaction case histories. The Boulanger and Idriss [2014] global database contains cases representing each of the four scenarios above, with multiple case histories based on the same CPT. Of the 255 case histories compiled therein, 25% are cases in which one CPT was used to develop multiple case histories. As an example, four case histories were developed from one CPT affected by earthquakes occurring over a 10-year span.

Second, does CPT data change over time once deposited or disturbed? Increases in the strength and stiffness of sands over time, or "aging effects," have been widely investigated. Temporal gains have been discerned both from penetration resistance, with reported gains of 3–7% per log-cycle in years [Mesri et al. 1990; Kulhawy and Mayne 1990], and from liquefaction resistance (i.e., CRR), with reported gains of 9–17% per log-cycle in years [Arango et al. 2000; Hayati and Andrus 2009; and Saftner et al. 2015]. It has thus been proposed that aging effects may be resolved into gains measurable by intermediate-to-large-strain penetration data and gains in liquefaction resistance, where the latter is influenced by small-strain fabric phenomena difficult to detect at large strains [Leon et al. 2006]. Of relevance to the compilation of case histories, CPT measurements could conceivably vary with time, particularly over short time scales following liquefaction. For example, assuming the rates above, and that a soil is "reset" following liquefaction, CPT resistance measured one month after an earthquake could be 3–7% less than if measured one year later. While such changes are plausible, they would be difficult to distinguish from site variability and measurement uncertainty, and to-date, have not been considered in case-history publications.

Third, does CPT data change due to repeated disturbance from shaking, and if so, does the magnitude and direction of change (e.g., an increase or decrease in penetration resistance) depend on whether liquefaction did or did not occur? A closely related, but different question, is whether liquefaction resistance changes due to prior shaking/liquefaction, even if CPT data does not change? Researchers have sought answers to these questions using a variety of approaches:

(i) CPT testing in the field before and after shaking/liquefaction (e.g., Lees et al. [2015b] and Finno et al. [2016]);

(ii) CPT testing in centrifuge and shaking-table models, before and after shaking/liquefaction (e.g., Darby et al. [2016] and Dobry et al. [2019]); and

(iii) cyclic triaxial and cyclic simple-shear tests wherein samples were subjected to multiple shaking/liquefaction sequences (e.g., Ha et al. [2011] and Wang et al. [2013]).

Various conclusions were collectively drawn from these experiments, including:

(i) penetration resistance increases;

(ii) penetration resistance decreases;

(iii) penetration resistance does not change, even after severe liquefaction;

(iv) penetration resistance changes in some parts of the profile but not others;

(v) the magnitude and direction of the change in penetration resistance depends on the number of previous shaking cycles, and on the pore pressure generated by those cycles; and

(vi) liquefaction resistance may change, independent of whether this change is detected via CPT data.

Currently, most relevant to the current effort, perhaps, is the work of Lees et al. [2015b], who studied pairs of CPTs performed at 30 locations before and after the 22 February 2011 Christchurch earthquake, and concluded that CPT measurements did not change in a statistically significant manner.

In summary, the approach taken by this study is consistent with past precedent. Additionally, questions pertaining to CPT data and soil response during earthquake sequences—which are very worthy of investigation—have not been adequately resolved to suggest when CPTs should or should not be used to compile liquefaction case histories. However, the compiled dataset could potentially be analyzed to further study these issues in the field, making use of the provided CPT coordinates and test dates.

2.6 CONCLUSIONS

Earthquakes occurring over the last decade in Canterbury, New Zealand, resulted in liquefaction case-history data of unprecedented quantity. Accordingly, this report discusses a curated dataset containing ~15,000 CPT-based liquefaction case-histories compiled from three earthquakes in this sequence. The compiled, post-processed data has been provided in a dense array structure, allowing researchers to easily access and analyze information pertinent to CPT-based site characterization and free-field liquefaction response. Research opportunities using this data may include, but are not limited to, the training or testing of new and existing liquefaction-prediction models. The many methods used to obtain and process the case-history data have been detailed herein, as is the structure of the compiled file. Numerous recommendations for analyzing the data have been outlined, including nuances and limitations that users should carefully consider prior to analysis.

2.7 DATA AVAILABILITY

The Canterbury dataset is available in digital format through the NEHRI DesignSafe Data Depot at https://doi.org/10.17603/ds2-tygh-ht91.

3 Part Two: Field Assessment of Liquefaction Prediction Models Based on Geotechnical vs. Geospatial Data, With Lessons for Each

Semi-empirical models based on in-situ geotechnical tests have been the standard-of-practice for predicting soil liquefaction since 1971. More recently, prediction models based on free, readily available data were proposed. These "geospatial" models rely on satellite remote sensing to infer subsurface traits without *in situ* tests. Using 15,223 liquefaction case histories from 24 earthquakes, this study assesses the performance of 23 models based on geotechnical or geospatial data using standardized metrics. Uncertainty due to finite sampling of case histories is accounted for and used to establish statistical significance. Geotechnical predictions are significantly more efficient on a global scale, yet successive models proposed over the last twenty years show little or no demonstrable improvement. In addition, geospatial models perform equally well for large subsets of the data—a provocative finding given the relative time- and cost-requirements underlying these predictions. Through this performance comparison, lessons for improving each class of model are elucidated in detail.

3.1 INTRODUCTION

Since the inception of the so-called "simplified stress-based procedure" for predicting liquefaction triggering [Seed and Idriss 1971; Whitman 1971], variants based on several *in situ* geotechnical measurements have been developed. These include CPT indices, standard penetration test (SPT) blow counts, and shear-wave velocity (V_s), among others. In conjunction with such measurements, "simplified" liquefaction triggering models have been used in virtually every seismic zone on Earth. The outputs from these triggering models are also often used cooperatively with other models that predict surface manifestations, such as ground settlement (e.g., Cetin et al. [2009]), lateral spreading (e.g., Zhang et al. [2004]), liquefaction ejecta (e.g., Maurer et al. [2017]), and foundation movements (e.g., Bray and Macedo [2017] and Bullock et al. [2018]. While this approach to modeling liquefaction occurrence and consequence is popular worldwide, it requires field measurements that can be costly and time consuming to perform, especially over large areas.

More recently, "geospatial" models have been proposed to predict liquefaction using data that is freely available via satellite remote sensing [Zhu et al. 2015; 2017]. Like the geotechnical approach, geospatial models characterize liquefaction demand using ground-motion IMs. In lieu of characterizing liquefaction resistance via *in situ* measurements, geospatial models use surface parameters to infer subsurface traits. Examples include surface slope, mineralogy, roughness, and wetness; distance to and elevation above rivers, streams, and other water bodies; and compound-topographic-index; all can be derived from satellite data. Geospatial models are particularly suited for applications where time- and cost-considerations outweigh the required, expected model accuracy (e.g., regional earthquake simulations; planning and policy development; post-event response and reconnaissance; and hazard assessments in regions that lack geotechnical testing). Implicit to this statement is the assumption that geotechnical models are more accurate than geospatial models. But are they?

The efficacies of these two model classes (i.e., geotechnical and geospatial) have not been directly compared using a consistent set of case histories and standardized performance metrics. Such an assessment could elucidate pathways to improve each model class (e.g., what can each class teach the other?) and inform ensemble-modeling approaches that statistically coalesce multiple predictions [Bradley et al. 2018]. In addition, while numerous "simplified" geotechnical models have been proposed over the last twenty years, the popular question of "which performs best?" remains contentious—the answer obscured, in part, by prior paucity and inconsistency of test cases, as well as use of differing, non-standard, non-objective performance metrics. Further, though often ignored, the performance of any model is intimately tied to the site-specific consequences, or "economies" of misprediction. Thus, we should ask not only "which model performs best?" but also "which model performs best for particular misprediction economies?"

Accordingly, the objective of this study was to rigorously assess and compare the performance of 18 geotechnical models and 5 geospatial models using 15,223 liquefaction case-histories compiled from 24 earthquakes in 9 countries. As part of this assessment, standardized and objective metrics were used to evaluate model performance, both in an overall, comprehensive sense, as well as for particular misprediction economies that may be encountered.

3.2 GEOTECHNICAL AND GEOSPATIAL LIQUEFACTION MODELS

The hierarchy of liquefaction models may be loosely defined by three tiers: (T1) wholly-empirical models that require only geologic or geospatial data and are accessible to a broad userbase (e.g., Youd and Hoose [1977]; Kramer [2008]; FEMA [2013]; and Zhu et al. [2017]); (T2) semi-mechanistic "simplified stress-based" models that require *in situ* measurements and are generally limited to use by geoengineers (e.g., Kayen et al. [2013] and Boulanger and Idriss [2014]); and (T3) wholly-mechanistic constitutive models, which typically require many soil and model parameters, and which are generally limited to use by geoengineers trained in computational mechanics (e.g., Cubrinovski and Ishihara [1998]; Byrne et al. [2004]; and Ziotopoulou and Boulanger [2016]). While advances to "T3" models and the enabling technologies have grown their use, their application to predicting liquefaction triggering remains relatively rare. This is due to the required inputs and operator skill, but also to uncertainties about model adequacy and the interpretation of results [NRC 2016]. As such, these models are not evaluated in this study, but are mentioned to provide proper context to the assessment of "T1" and "T2" models presented herein.

For brevity, the "T2, simplified stress-based models" are henceforth referred to as "geotechnical models." Six liquefaction triggering models were used in this study: Robertson and Wride [1998], Architectural Institute of Japan [2001], Moss et al. [2006], Idriss and Boulanger [2008], Boulanger and Idriss [2014], and Green et al. [2018]. All six are based on the CPT, which offers significant advantages over other in-situ tests [NRC 2016]. Because triggering models predict liquefaction at-depth within a soil profile, an evaluation of their performance requires direct investigation of the subsurface (i.e., to assess the agreement between predicted and actual responses in various strata). This might be accomplished proactively using downhole instrument-arrays (e.g., Holzer et al. [2007]) or reactively using vision penetrometers [Raschke and Hryciw 1997] or geoslicers [Nakata and Shimazaki 1997]. Yet, such investigations are generally expensive, exceedingly rare, and may not result in definitive interpretations (e.g., Takada and Atwater [2004]).

Thus, nearly all existing case-histories simply document whether manifestations of liquefaction were observed at the surface. Accordingly, to compare predictions of liquefaction at-depth against surface observations, the six triggering models will each be used in series with three separate manifestation models: Iwasaki et al. [1978], van Ballegooy et al. [2014a], and Maurer et al. [2015a], who respectively proposed models named LPI, LSN, and LPI_{ISH}. It must therefore be understood that "geotechnical model" refers to the combined use of a triggering model and a manifestation model. There is simply no practical or objective way to isolate and assess the independent performance of triggering models. While LPI, LSN, and LPI_{ISH} were each proposed as general "ground failure" predictors, they have been calibrated almost exclusively on the observed occurrence or non-occurrence of liquefaction ejecta.

The 18 CPT-based geotechnical models (6 triggering models and 3 manifestation models) were tested against the performance of 5 "T1" geospatial models. While several types of "T1" model exist, those of Zhu et al. [2015; 2017] are arguably the most rigorously formulated and well-trained to date; they were also recently implemented into U.S. Geological Survey post-earthquake data products to provide automated content on possible impacts (e.g., Allstadt et al. [2019]). These models were trained on observations of ground failure and thus inherently merge liquefaction triggering and manifestation. Three of the five models to be assessed are region specific—developed specifically for Canterbury, New Zealand—and will be referred to as regional geospatial models (RGMs). The remaining two were trained on successively larger datasets from global earthquakes and will be referred to as global geospatial models (GGMs). A summary of the 23 models to be evaluated, and the symbols henceforth used to identify them, is provided in Table 2.1. Additional model details are provided subsequently in Section 3.4.

Table 3.1 Summary of geotechnical and geospatial liquefaction models evaluated in this study.

Geotechnical models (18)			
Triggering model	**Symbol**	**Manifestation model**	**Symbol**
Robertson and Wride [1998]	RW98	Iwasaki et al. [2015]	LPI
Arch. Intitute, Japan [2001]	AIJ01		
Moss et al. [2006]	Mea06	Van Ballegooy et al. [2014a]	LSN
Idriss and Boulanger [2008]	IB08		
Boulanger and Idriss [2014]	BI14	Mauer et al. [2015a]	LPI_{ISH}
Green et al. [2019]	Gea19		

Geospatial models (5)	
Triggering/manifestation model	**Symbol**
Zhu et al. [2015] Regional 1	RGM1
Zhu et al. [2015] Regional 2	RGM2
Zhu et al. [2015] Regional 3	RGM3
Zhu et al. [2017] Global 1	GGM1
Zhu et al. [2015] Global 2	GGM2

3.3 DATA

This study analyzed 15,223 liquefaction case histories resulting from 24 earthquakes, as summarized in Table 3.2. However, because most of these cases were compiled from three earthquakes in the Canterbury region of New Zealand, results are separately presented for these and the other 21 earthquakes, henceforth respectively referred to as the “Canterbury dataset” and “global dataset.” The details of these case-history datasets are discussed next.

Table 3.2 Summary of liquefaction case-histories analyzed.

Date	Earthquake	Country	Magnitude (M_w)	Number of case histories
16/6/1964	Niigata	Japan	7.60	3
9/2/1971	San Fernando	USA	6.60	2
4/2/1975	Haicheng	China	7.00	2
27/7/1976	Tangshan	China	7.60	10
15/10/1979	Imperial Valley	USA	6.53	7
9/6/1980	Victora (Mexicali)	Mexico	6.33	5
26/4/1981	Westmoreland	USA	5.90	9
26/5/1983	Nihonkai-Chubu	Japan	7.70	2
28/10/1983	Borah Peak	USA	6.88	3
2/3/1987	Edgecumbe	New Zealand	6.60	23
24/11/1987	Elmore Ranch	USA	6.22	2
24/11/1987	Superstition Hills	USA	6.54	8
18/10/1989	Loma Prieta	USA	6.93	67
17/1/1994	Northridge	USA	6.69	3
16/1/1995	Hyogoken-Nambu	Japan	6.90	21
17/8/1999	Kocaeli	Turkey	7.51	16
20/9/1999	Chi-Chi	Taiwan	7.62	34
8/6/2008	Achaia-Ilia	Greece	6.40	2
4/4/2010	Baja	Mexico	7.20	3
4/10/2010	Darfield	New Zealand	7.10	5371
22/2/2011	Christchurch	New Zealand	6.20	4806
11/3/2011	Tohoku	Japan	9.00	7
20/5/2012	Emilia	Italy	6.10	46
14/2/2016	Christchurch	New Zealand	5.70	4771
			Total	**15,223**

3.3.1 Canterbury Earthquake Dataset

Earthquakes occurring over the last decade in the Canterbury region of New Zealand have resulted in case-history data of unprecedented quantity and quality. A comprehensive summary of these earthquakes, to include tectonic and geologic settings, seismology, and effects, is provided by Quigley et al. [2016]. The present study compiles case-histories from the M_w7.1, 4 September 2010 Darfield earthquake, the M_w6.2, 22 February 2011 Christchurch earthquake, and the M_w5.7, 14 February 2016 Christchurch earthquake. This effort built upon a series of successive compilations [Maurer et al. 2014; 2015b; 2019], augmenting the largest of these by more than 50% and resulting in a total of 14,948 case histories. These consist of ground-motion IMs, geotechnical and hydrological data, readily available geospatial information, and classifications of liquefaction manifestations. These components are succinctly summarized as follows.

3.3.1.1 Liquefaction Manifestations

All liquefaction models will be evaluated on their ability to predict free-field surface manifestations on level ground—specifically liquefaction ejecta—rather than any other indicator, such as evidence from ground motions, foundation movements, or lateral spreading. Sites with these indicators were expressly removed from the study because the models to be evaluated are not intended to predict such indicators. Observations of the occurrence and severity of liquefaction ejecta were compiled by the authors and classified as "none," "minor," "moderate," and "severe" using criteria from Green et al. [2014] and a 15-m sampling radius centered on each CPT site. This was accomplished using ground-reconnaissance reports and high-resolution satellite imagery available in the New Zealand Geotechnical Database [CERA 2012]. Cases in which manifestations could not be reliably classified were not included herein. To facilitate model assessment, the cases are reclassified binomially as "No Manifestation" and "Manifestation," where the latter are sites with at least "minor" manifestations per Green et al. [2014]. Of the resulting 14,948 case histories compiled from Canterbury, 65% are "No Manifestation" and 35% are "Manifestation."

3.3.1.2 Ground-Motion Intensity Measures

The 23 liquefaction models use either PGA (all geotechnical models and some geospatial models) or peak ground velocity (PGV) (some geospatial models). For this study, PGAs were estimated with the Bradley [2013] procedure, which has been used in previous Canterbury earthquake research (e.g., van Ballegooy et al. [2015]), and which geostatistically merges PGAs recorded at strong-motion stations with PGAs estimated by ground-motion prediction equations. The PGVs were estimated using USGS ShakeMap [Worden and Wald 2016], consistent with the formulation of geospatial liquefaction models that use PGV.

3.3.1.3 Geotechnical, Hydrological, and Geospatial Data

This study analyzes CPT soundings available in the New Zealand Geotechnical Database [CERA 2012] and performed at sites where liquefaction manifestations were classified as described above. In the process of compiling case histories, CPTs were rejected if: (1) the depth of "pre-drill" significantly exceeded the depth of the ground water table; and (2) were inferred to have prematurely terminated on shallow gravels from a geospatial autocorrelation analysis [Anselin 1995]. Prior to processing, CPT tip- and sleeve-measurements were aligned using cross-correlation [Buck et al. 2002]. Extended coverage of CPT data and the exclusion criteria summarized above is provided in Maurer et al. [2014, 2015b]. Ground water table depths were sourced from the robust, event-specific regional models of van Ballegooy et al. [2014b]. Various geospatial parameters—to be identified subsequently in Section 3.4—were computed at each case-history location following the exact methods of Zhu et al. [2015; 2017] (i.e., the developers of the geospatial models to be evaluated).

3.3.2 Global Earthquake Dataset

To compare findings in Canterbury with regions worldwide, 275 case histories were compiled from 21 global earthquakes and assessed in parallel. These cases, sourced from the literature, included observations of manifestation severity, CPT soundings, and estimation of GWT depth and ground-motion IMs, as generally reported by original investigators. When available, recent refinements were adopted from the literature. Whereas liquefaction was intensively cataloged via reconnaissance and remote sensing in Canterbury, the global cases are often documented in less detail, occasionally with scant information about the nature or severity of manifestation. Accordingly, while the Green et al. [2014] criteria were again used to binomially classify manifestations based on ejecta (while excluding cases with other expressions of liquefaction), there is inevitably some uncertainty. Of the 275 global cases, 58% are "Manifestation" and 42% are "No Manifestation." To properly recognize all sources of data used to compile this dataset, a separate reference list parsed by earthquake appears near the end of this chapter; a table of data for each case history is also provided in Appendix A. In this regard, the case-history assemblages of Moss et al. [2003] and Boulanger and Idriss [2014] are acknowledged for greatly assisting the present study. Lastly, various geospatial parameters (identified in Section 3.4) were computed at each case-history location per Zhu et al. [2015; 2017].

3.4 METHODOLOGY

The 23 liquefaction models to be evaluated in this study were identified in Table 3.1. Additional details are now presented, followed by methods that will be used to analyze model performance.

3.4.1 Geotechnical Model Methodology

The CPTs were analyzed using six triggering models, all of which compute factor-of-safety against liquefaction (FS_{liq}) vs. depth. While the reader is referred to the model publications for complete details, nuances pertinent to this study are as follows. First, prior to using any of the six models, liquefaction-susceptible soils were inferred from the CPT soil-behavior-type index (I_c) [Robertson and Wride 1998], such that soils with $I_c < 2.50$ were assumed susceptible. This criterion was developed specifically for Christchurch soils from extensive lab and field testing [Maurer et al. 2019]. However, because an I_c threshold of 2.50 is within the range of generic values commonly used in practice (e.g., 2.4–2.6), this criterion was also used in all analyses of the global dataset. Ultimately, the results of these analyses were found to be insensitive to this threshold. Second, for liquefaction-susceptible soils, the IB08, BI14, and Gea19 models compute liquefaction resistance as a function of fines-content (FC). Accordingly, the FC was estimated for the Canterbury dataset using a Christchurch-specific I_c–FC correlation [Maurer et al. 2019], and for the global dataset using a general I_c–FC correlation [Boulanger and Idriss 2014], with the former estimating FC to be approximately 10% higher for a given I_c.

Next, the outputs from triggering analysis were input to the LPI, LSN, and LPI_{ISH} manifestation models. The Liquefaction Potential Index (LPI) is defined as [Iwasaki et al. 1978]:

$$\text{LPI} = \int_0^{20\text{ m}} F\left(FS_{\text{liq}}\right) \cdot w(z)\, dz \tag{3.1}$$

where $F(FS_{\text{liq}})$ and $w(z)$ are functions that weight the respective influences of FS_{liq} and depth, z, on surface manifestation. Specifically, $F(FS_{\text{liq}}) = 1 - FS_{\text{liq}}$ for $FS_{\text{liq}} \leq 1$ and $F(FS_{\text{liq}}) = 0$; otherwise $w(z) = 10$. Thus, the LPI assumes that surface manifestation depends on the thickness of all liquefied strata in a profile's upper 20 m, their proximity to the ground surface, and the amount by which FS_{liq} in each stratum is less than 1.0. Given this definition, the LPI can range from zero to 100.

A modified LPI was proposed by Maurer et al. [2015a] and inspired by Ishihara [1985], who proposed limit-state curves for predicting manifestations as a function of the "crust" thickness

(H_1), among other factors. Using these curves, Maurer et al. [2015a] modified the LPI to include the observed influence of H_1. Given its provenance, the result was termed LPI_{ISH} and is defined by:

$$\text{LPI}_{\text{ISH}} = \circ \int_{H_1}^{20\circ\text{m}} F\left(FS_{\text{liq}}\right) \cdot w\left(z\right) dz \tag{3.2a}$$

where

$$F\left(FS_{\text{liq}}\right) = \begin{cases} 1 - FS_{\text{liq}} \text{ if } FS_{\text{liq}} \leq 1 \circ \text{andandand} \cap \circ H_1 \cdot \text{m}\left(FS_{\text{liq}}\right) \leq 3 \\ 0 \text{ otherwise} \end{cases} \tag{3.2.b}$$

$$\text{m}\left(FS_{\text{liq}}\right) = \exp\left(\frac{5}{25.56\left(1 - FS_{\text{liq}}\right)}\right) - 1 \tag{3.2c}$$

In Equation (3.2a), $F(FS_{\text{liq}})$ and $w(z)$ have the same objective as in the LPI, but are functionally different, such that $F(FS_{\text{liq}})$ accounts for the crust thickness via the parameter H_1 and $w(z)$ is defined by $w(z) = 25.56 \cdot z^{-1}$. Maurer et al. [2015a] recommended a minimum H_1 of 0.4 m be used, even if liquefiable soils are present at shallower depths. Given this constraint, LPI_{ISH} can range from zero to 100.

The Liquefaction Severity Number (LSN) is an adaptation of methods for estimating post-liquefaction volumetric strain (e.g., to predict ground settlement), modified to include a power-law depth weighting function (van Ballegooy et al. [2014a]:

$$\text{LSN} = \int_0^{20\text{m}} \varepsilon_v \cdot w\left(z\right) dz \tag{3.3}$$

where ε_v is volumetric strain (%), and $w(z) = 10 \cdot z^{-1}$. For a given value of FS_{liq}, ε_v is inversely related to the soil's initial relative density (D_r). By corollary, surface manifestations should diminish as the D_r of liquefying soil increases. While there are several approaches to estimating ε_v [Geyin and Maurer 2019; van Ballegooy et al. 2014a], we adopted that of Zhang et al. [2002]. The LSN values can far surpass 100 when liquefiable soils are present at the surface, but typically are between zero and 100. These values are not quantities of predicted settlement, but are index values á la LPI and LPI_{ISH} that correlate to the likelihood of surface manifestation.

3.4.2 Geospatial Model Methodology

The five geospatial models have the general form $P(X) = (1 + e^{-X})^{-1}$ where X is a series of geospatial variables and model coefficients, and $P(X)$ is the likelihood of surface manifestation. In conjunction with this equation, the three region-specific and two global geospatial models are defined in Table 3.3. The variables are as follows:

- PGA_{M} = magnitude-weighted peak ground acceleration (g) using the weighting of Youd et al. [2001]
- PGV = peak ground velocity (cm/sec)

- d_{r3} = distance (km) to a stream of order three or greater [Strahler 1952]
- V_{s30} = shear-wave velocity of the upper 30 m (m/sec), inferred from surface topography [Wald and Allen 2007]
- d_r = shortest distance to a river (km) cataloged by Lehner et al. [2006]
- CTI = compound topographic index [Beven and Kirkby 1979]
- d_c = distance to coast (km)
- *precip* = mean annual precipitation (mm) [Fick and Hijmans 2017]
- ND = d_c divided by the distance from the coast to the edge of the sedimentary basin
- wtd = water table depth (m)

The GGM2 has variants for coastal and inland locations, the distinguishing threshold being d_c = 20 km. All variables were computed in accordance with Zhu et al. [2015; 2017], to which the reader is referred for additional information. Geospatial model predictions were generated at 30-m resolution, commensurate with the sampling area over which liquefaction manifestations were classified.

Table 3.3 Geospatial liquefaction model equations.

Model	Model Parameter X
RGM1	$2.053 + 1.267 \cdot \ln(PGA_M) - 0.239 \cdot d_{r3} - 9.191 \cdot ND$
RGM2	$0.316 + 1.225 \cdot \ln(PGA_M) + 0.145 \cdot CTI - 9.708 \cdot ND$
RGM3	$25.45 + 2.476 \cdot \ln(PGA_M) - 0.323 \cdot d_{r3} - 4.241 \cdot \ln(V_{s30})$
GGM1	$24.10 + 2.067 \cdot \ln(PGA_M) + 0.355 \cdot CTI - 0.4784 \cdot \ln(V_{s30})$
GGM2 (coastal)	$12.435 + 0.301 \cdot \ln(PGV) - 2.615 \cdot \ln(V_{s30}) + 5.556 \times 10^{-4} \cdot precip - 0.0287 \cdot (d_c)^{0.5} + 0.0666 \cdot d_r - 0.0369 \cdot d_r \cdot (d_c)^{0.5}$
GGM2 (inland)	$8.801 + 0.334 \cdot \ln(PGV) - 1.918 \cdot \ln(V_{s30}) + 5.408 \times 10^{-4} \cdot precip - 0.2054 \cdot d_w - 0.0333 \cdot wtd$

3.4.3 Performance-Evaluation Methodology

Standardized and objective methods are needed to analyze model efficacy (i.e., the ability to predict whether sites have liquefaction manifestations). Receiver-operating-characteristic analyses, which are widely used in biostatistics and medical diagnostics (e.g., Fawcett [2006] and Zou [2007], were adopted herein. In any ROC analysis, the distributions of "positives" (e.g., manifestations are observed) and "negatives" (e.g., no manifestations are observed) overlap when the frequencies of the distributions are expressed as a function of a diagnostic test index (e.g., LPI, LSN, etc.).

To demonstrate, two such distributions are shown in Figure 3.1(a), plotted as a function of LPI. The ROC curves plot the rates of true-positive predictions (R_{TP}) (i.e., manifestations are observed as predicted) and false-positive predictions (R_{FP}) (i.e., manifestations are predicted but not observed) as a function of classification "thresholds." These thresholds are used to predict outcomes, such that index values above and below a threshold respectively predict positives and negatives. Figure 3.1(b) illustrates the relationship among the positive and negative distributions, the threshold values, and the ROC curve. Low thresholds result in a high R_{FP}, while high thresholds result in a low R_{TP}, equivalent to a high rate of false-negative predictions (R_{FN}), where $R_{FN} = 1 - R_{TP}$. In general, neither of these situations is desirable.

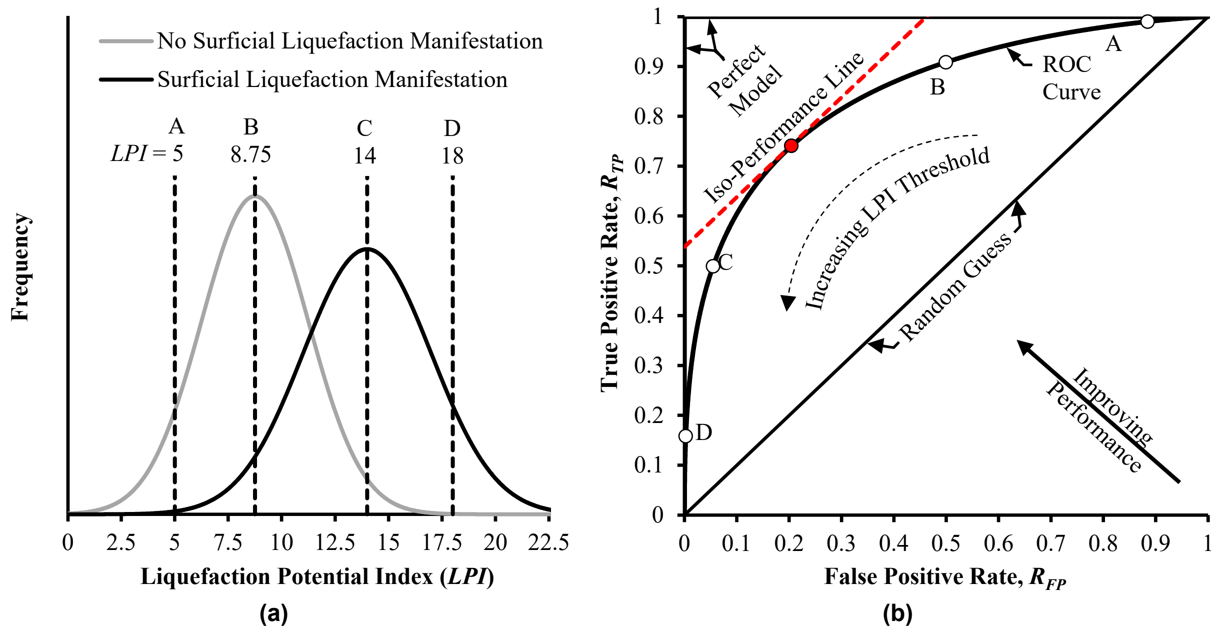

Figure 3.1 **ROC analyses: (a) frequency distributions of liquefaction manifestation and no liquefaction manifestation as a function of LPI; and (b) corresponding ROC curve, and illustration of how a ROC curve is used to assess the efficiency of a diagnostic test.**

The optimal threshold may be defined as that which minimizes the prediction cost:

$$\text{Cost} = C_{FP} \times R_{FP} + C_{FN} \times R_{FN} \tag{3.4}$$

where C_{FP} and R_{FP} are respectively the cost and rate of false-positive predictions, and C_{FN} and R_{FN} are respectively the cost and rate of false-negative predictions. Examples of false-positive costs include superfluous spending on design and construction (e.g., ground improvement costs), while false-negative costs are those resulting from liquefaction (e.g., property damage and lost productivity, among others). Normalizing by C_{FN}, Equation (3.4) is alternatively expressed as:

$$\text{Cost}' = \text{Cost}/C_{FN} = R_{FP} \times CR + R_{FN} \tag{3.5}$$

where $CR = C_{FP}/C_{FN}$ and is the "cost ratio" representing different misprediction economies. Low-CR scenarios with are those where the costs of liquefaction far outweigh the costs of mitigation (e.g., a critical facility), while high CR scenarios are those where the costs of mitigation far outweigh the costs of liquefaction (e.g., a car park). It follows from Equations (3.4) and (3.5) that two points in ROC space, (R_{FP1}, R_{TP1}) and (R_{FP2}, R_{TP2}), have equivalent performance if:

$$\frac{R_{TP1}\text{-}R_{TP2}}{R_{FP1}\text{-}R_{FP2}} = \frac{C_{FP}}{C_{FN}} = \text{CR} = m \tag{3.6}$$

Equation (3.6) defines the slope, m, of an iso-performance line, such that all points defining the contour have equal Cost′. Thus, each CR corresponds to a unique contour in ROC space. One such line is shown in Figure 3.1b. With 1:1 slope, it corresponds to the case where false positives and false negatives have equal costs. Points tangent to this line on the ROC curve correspond to threshold values at which Cost′ is minimized.

To evaluate model efficacy, two different ROC-based methods were used. The first quantified comprehensive performance via the area under a ROC curve (AUC). While no single parameter fully characterizes performance, the AUC is commonly used for this purpose due to its statistical significance and objectivity (e.g., Fawcett [2006]). Here, AUC is the probability that sites with manifestations have higher computed index values (e.g., LPI) than sites without manifestations. Better prediction models thus have a higher AUC. As shown in Figure 3.1b, random guessing is depicted in ROC space by a 1:1 line through the origin, for which AUC = 0.5. A perfect model, for which AUC = 1.0, plots as a point at (0,1), indicating the existence of a threshold value that perfectly separates the two distributions. To account for finite sampling of case histories, bootstrap simulations were performed to quantify ROC uncertainty, and in turn, to compute confidence intervals on each model's AUC. This illustrates the sensitivity of model performance to the case histories compiled for analysis. To assess whether differences in AUC could arise from chance (i.e., due to finite sampling), tests of statistical significance were performed per the method of DeLong et al. [1988], which is specific to ROC analyses. All models were compared to one another to determine which, if any, were statistically better.

While AUC is widely used, it reflects overall performance across all misprediction economies. As a result, the model with highest AUC, the model with lowest misprediction rate (R_{FN} + R_{FP}), and the model most optimal when $C_{FN} \neq C_{FP}$ could conceivably all be different. This is shown in Figure 3.2(a), where models A and B have identical AUC. If CR = 1/5, iso-performance lines have slope of 1/5 and define points with equal prediction cost. What that cost *is* depends on the lines of the R_{TP} intercepts and is given by Equation (3.6) (the greater the R_{TP} intercept, the lower the cost). Since an iso-performance line tangent to curve B has a greater R_{TP} intercept than one tangent to curve A, model B is more optimal. That is, B is better in the "conservative" region, where models correctly classify most positives, but at the expense of high R_{FP}. Conversely, and by the same logic, A is optimal when CR = 5 and is better in the "liberal" region, where models correctly classify most negatives, but at the expense of low R_{TP}. Lastly, when CR = 1, A and B perform equally well. By similar logic, a model with higher AUC could be less efficient in a specific region of ROC space than a model with lower AUC. This is shown in Figure 3.2(b): model A has higher AUC and is optimal when CR > 0.27, but model B is optimal for all other CR. Thus, AUC reflects overall performance, but not the nuances described above. Accordingly, a second ROC-based analysis will identify the optimal model as a function of CR. Cost′ will be computed by Equation (3.5) for each model over the domain 0 < CR < 2; that with lowest Cost′ at a given

CR is most optimal, which is equivalent to the graphical analysis shown in Figure 3.2. Together, these methods will assess model performance, both in a comprehensive sense, and for various misprediction economies of interest.

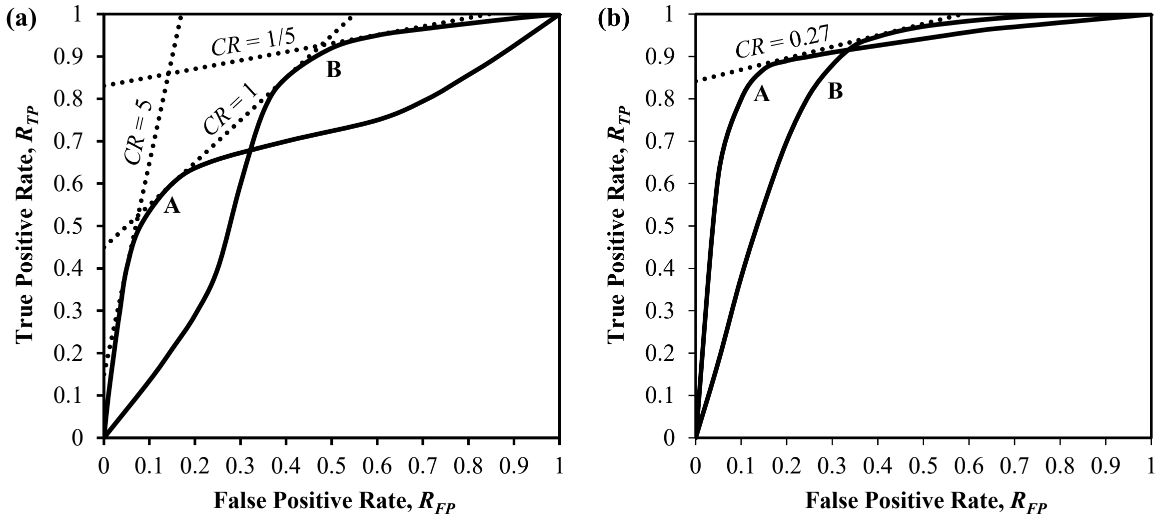

Figure 3.2 The ROC analyses demonstrating that: (a) classifiers with equivalent AUC (i.e., equal overall efficiency) can perform very differently in specific regions of ROC space; and (b) classifiers with higher AUC can, in specific regions of ROC space, perform worse than classifiers with lower AUC.

3.5 RESULTS AND DISCUSSION

Utilizing the data and methodology above, 23 models were used to predict liquefaction manifestations for 15,223 case histories. To illustrate how ROC analyses and bootstrap simulations were used to study model-performance, results for one model were presented in detail; summary statistics from analyses of all 23 models were then provided. In Figure 3.3, ROC analyses of the BI14–LPI geotechnical model (i.e., the BI14 triggering model used with the LPI manifestation model) are presented for the Canterbury and global datasets, respectively. In each case, a total of 10,000 bootstrap simulations were performed, from which 95%-confidence intervals (CIs) were computed. The 50th percentile ROC curve is equivalent to that resulting from an analysis of all case histories without resampling.

Two observations are made from this figure: (1) the BI14-LPI model performs better on the Canterbury dataset than the global dataset, with respective median AUCs of 0.83 versus 0.77; and (2) finite-sample uncertainty is considerably larger for the global dataset. The 95% CI on *AUC* is 0.828 to 0.841 for the Canterbury dataset, and 0.709 to 0.826 for the global dataset. Each of these observations will be discussed further in the context all models.

From replicate ROC analyses of all 23 prediction models, AUC summary statistics are compiled and presented in Figure 3.4 for the Canterbury and global datasets, respectively. Shown are each model's median AUC and 95% CI, with results ordered by the year in which each model was proposed. In this regard, geotechnical models are dated in accordance with the triggering model but are grouped/symbolized by manifestation model. Thus, Figure 3.4 allows for assessments to be made regarding the evolution of performance (i.e., prediction efficiency) through twenty years of model research and development.

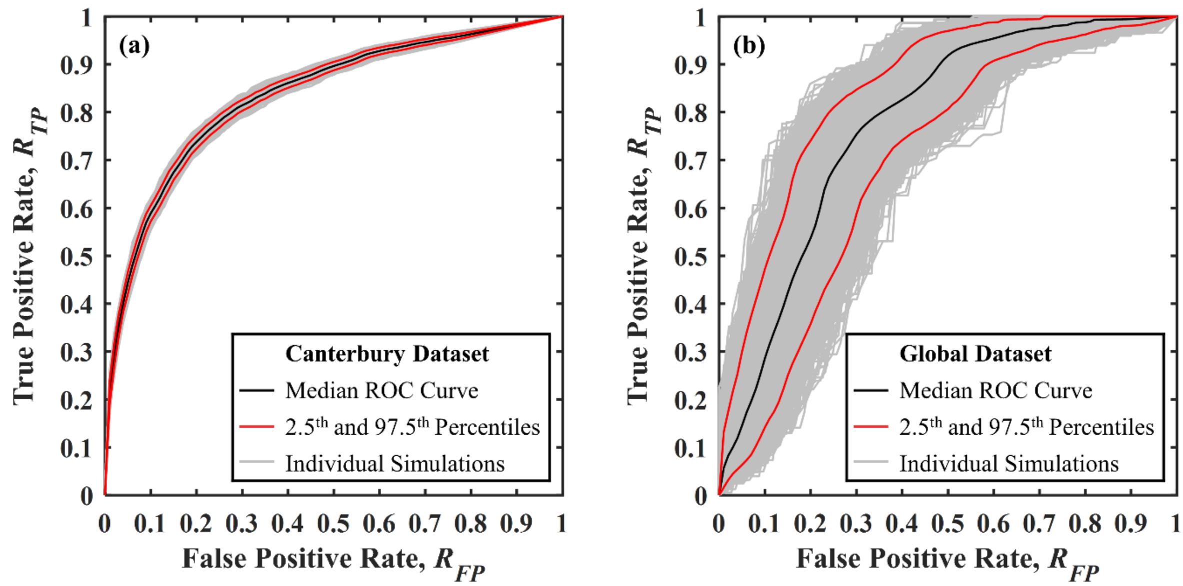

Figure 3.3 **ROC analysis of BI14-*LPI* performance in predicting liquefaction surface manifestation for the: (a) Canterbury dataset; and (b) global dataset.**

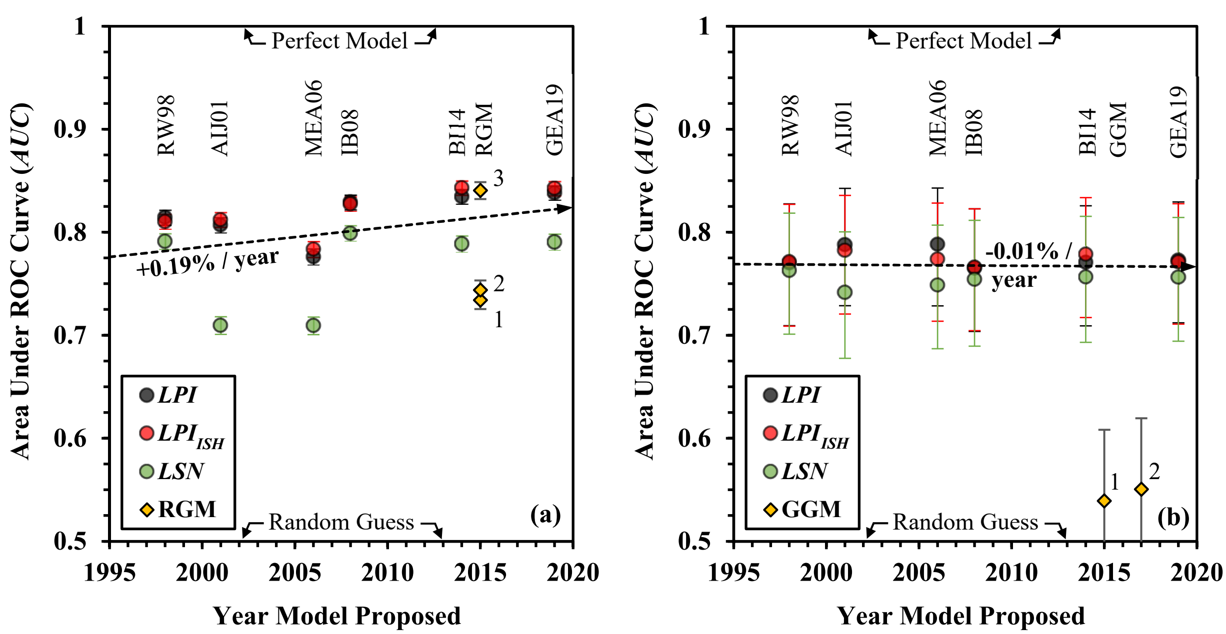

Figure 3.4 **Summary of liquefaction-model performance—quantified by AUC—or 23 models, ordered by year proposed: (a) Canterbury dataset; and (b) global dataset. Markers = median AUC; bars = 95% confidence intervals on *AUC*; all model acronyms are identified in Table 2.1. Trendlines are developed from linear regression and do not include RGM or GGM data points.**

With respect to Figure 3.4, several observations are made as follows:

1. The two trends identified in Figure 3.3 for BI14-LPI are true of most geotechnical models. That is: their performance on the Canterbury dataset tends to be marginally better and much less uncertain, relative to the global dataset. Considering all 18 geotechnical models, the average AUCs are 0.80 and 0.77, respectively, for the Canterbury and global datasets, indicating also that the models are nearer to perfection (AUC = 1.0) than to random guessing (AUC = 0.5). The average 95% CIs are respectively 0.015 and 0.118 for the Canterbury and global datasets. These differences may be attributable to the global dataset's greater seismologic, geologic, and geomorphic diversity and/or because the global field-data (e.g., ground-motion IMs, CPTs) were collected over many decades using different means and methods. There are also far fewer global case-histories; all else being equal, greater finite-sample uncertainty is thus expected;
2. As shown in Figure 3.4, trendlines were fit to the AUC values for all geotechnical models; these regressions did not include the regional or global geospatial models, as discussed below. Through 20 years of model research and development, the trendlines suggest improvements to AUC of 0.19% per year and -0.01% per year for the Canterbury and global datasets, respectively. When considering these trends, it should be noted that: (i) the BI14 and Gea19 triggering models, when developed, were trained on a case-history dataset in which 20% of data was from Canterbury, so their evaluation in Figure 3.4(a) is not completely unbiased, unlike the other models; and (ii) some of the global case-histories compiled to test performance in Figure 3.4b( )were also used to train triggering models during their respective developments. Specifically, of the 275 global test cases, the portion used in training ranges from 0% (RW98) to 75% (e.g., BI14). Nevertheless, successive models proposed over the last twenty years show little or no demonstrable improvement for the two datasets analyzed, as shown in Figure 3.4. This is despite: (i) ever-increasing data that can be used to train and validate models; and (ii) greater knowledge of liquefaction mechanics, embodied by new and revised model components (e.g., magnitude scaling; depth-stress reduction; overburden correction). Of course, greater performance variation might result if the models were tested on data outside the parameter space of that used to train them (e.g., liquefaction-susceptible soils with atypical density, depth, fines-content, age, etc.). However, liquefaction case histories tend to have much in common, so such data is not easily obtained;
3. It can be seen in Figure 3.4(a) that the three regional geospatial models perform remarkably well for the Canterbury dataset, with average AUC of 0.77 (versus 0.80 for all geotechnical models). One geospatial model—RGM3—outperforms 16 of the 18 geotechnical models, a provocative result given the relative costs and complexities of the required model inputs. While differences in model specificity must be acknowledged (RGM3 is region-specific, while the geotechnical models are not), it is nonetheless surprising that an empirical model based on surface

parameters could outperform a semi-mechanistic model based on subsurface measurements. However, as shown in Figure 3.4(b), geospatial models do not perform as well on the global dataset, with global models GGM1 and GGM2 having median AUCs of 0.54 and 0.55, respectively (the 95% CIs are 0.47 to 0.61 and 0.48 to 0.62, respectively). Thus, while the geospatial models *do* tend to be useful (e.g., performing better than random guessing for the compiled test cases), the geotechnical models are significantly more efficient. This is unsurprising when considering: (i) the geomorphic, topographic, and climatic diversity of the global dataset; and (ii) the difficulty, given this diversity, of accurately inferring below-ground conditions from above-ground parameters. Inherently, the geotechnical models—being based on direct measurements of the subsurface—should have better portability across environs. Nonetheless, the results from Canterbury in Figure 3.4(a) demonstrate the provocative potential of geospatial modeling. As more test data become available, and as better geospatial predictors are identified, improved global performance should result. In contrast, considering the 20-year trendlines in Figure 3.4, it appears less likely that geotechnical models will soon improve greatly should the status quo continue. Neither fine-tuning of model parameters nor incremental grown in training data are likely to inflect these trends upwards. Arguably, this would occur only with disruptive innovation (e.g., to the *in situ* characterization method, or to the fundamental modeling approach); and

4. The top-performing models, as quantified via median AUC, are: (i) Canterbury dataset: BI14-LPI_{ISH} (AUC = 0.843), Gea19-LPI_{ISH} (AUC = 0.843), and RGM3 (AUC = 0.841); and (ii) global dataset: Mea06-LPI (AUC = 0.788), AIJ01-LPI (AUC = 0.788), and AIJ01- LPI_{ISH} (AUC = 0.782). Thus, the top-performing models appear to be different for the two datasets. However, given the uncertainties of AUC values—particularly for the global dataset—it should be determined whether the measured differences in performance are statistically significant.

Using the method of DeLong et al. [1988], *P*-values were computed to compare each of the 23 models to all others. These values are presented in Tables 3.4 and 3.5 for the Canterbury and global datasets, respectively, and are the probabilities that AUC samples for two models could have come from the same distribution (i.e., that the observed difference in performance arose from chance and not because one model is better). Large *P*-values can be expected when (i) differences between two AUC values are small; and (ii) the uncertainty of one or more of the AUC values is large. The popular significance level of 0.05 of adopted herein, such that *P*-values below 0.05 denote that models have significantly different performance. Using this criterion, Tables 3.4 and 3.5 compare all model pairs and identify which model, if any, is statistically better.

As seen in Table 3.4, instances of large *P*-values are rare for the Canterbury dataset, which can be partly attributed to the large number of case histories. In fact, nearly every model performs statistically differently than all others. Notable observations from Table 3.4 are: (i) among all 23 models evaluated, no model is statistically better than all others; but (ii) three models are either statistically better, or not statistically different, than all others. In other words, three models are never bested. These are BI14-LPI_{ISH}, Gea19-LPI_{ISH}, and RGM3. Most striking is that no geotechnical model is statistically better than geospatial model RGM3.

In contrast to the Canterbury dataset, few P-values are below 0.05 for the global dataset, indicating that performance-differences between models are typically not statistically significant. Notable observations from Table 3.5 are: (i) all geotechnical models are statistically better than both global geospatial models; and (ii) no model is statistically superior. The previously identified top-performing model globally – Mea06-LPI – is statistically better than nine other models, but is statistically indifferent from eight others, including the top-performing models in Canterbury (BI14-LPI_{ISH} and Gea19-LPI_{ISH}). Thus, once statistical significance is considered, the global results are largely inconclusive due to the large finite-sample uncertainties of *AUC* values. Consequently, the top-performing geotechnical models in Canterbury may also be the top-performing models globally, but more global data would be needed to confirm this or to draw other conclusions about model performance.

Table 3.4 ***P*-value matrix to compare model performance for the Canterbury dataset.**

Statistically better*	↑	LPI						LPI_{ISH}						LSN						RGM		
←		RW98	AIJ01	Mea06	IB08	BI14	Gea19	RW98	AIJ01	Mea06	IB08	BI14	Gea19	RW98	AIJ01	Mea06	IB08	BI14	Gea19	1	2	3
LPI	RW98		0.000	0.000	0.000	0.000	0.000	0.000	0.018	0.000	0.000	0.000	0.000	0.000	0.000	0.000	0.000	0.000	0.000	0.000	0.000	0.000
	AIJ01			0.000	0.000	0.000	0.000	0.177	0.001	0.000	0.000	0.000	0.000	0.000	0.000	0.000	0.000	0.000	0.000	0.000	0.000	0.000
	Mea06				0.000	0.000	0.000	0.000	0.000	0.000	0.000	0.000	0.000	0.000	0.000	0.000	0.000	0.000	0.000	0.000	0.000	0.000
	IB08					0.000	0.000	0.000	0.000	0.000	0.013	0.000	0.000	0.000	0.000	0.000	0.000	0.000	0.000	0.000	0.000	0.002
	BI14						0.000	0.000	0.000	0.000	0.000	0.000	0.000	0.000	0.000	0.000	0.000	0.000	0.000	0.000	0.000	0.082
	Gea19							0.000	0.000	0.000	0.000	0.004	0.023	0.000	0.000	0.000	0.000	0.000	0.000	0.000	0.000	0.362
LPI_{ISH}	RW98								0.530	0.000	0.000	0.000	0.000	0.000	0.000	0.000	0.000	0.000	0.000	0.000	0.000	0.000
	AIJ01									0.000	0.000	0.000	0.000	0.000	0.000	0.000	0.000	0.000	0.000	0.000	0.000	0.000
	Mea06										0.000	0.000	0.000	0.000	0.000	0.000	0.000	0.023	0.002	0.000	0.000	0.000
	IB08											0.000	0.000	0.000	0.000	0.000	0.000	0.000	0.000	0.000	0.000	0.000
	BI14												0.271	0.000	0.000	0.000	0.000	0.000	0.000	0.000	0.000	0.943
	Gea19													0.000	0.000	0.000	0.000	0.000	0.000	0.000	0.000	0.823
LSN	RW98														0.000	0.000	0.000	0.043	0.399	0.000	0.000	0.000
	AIJ01															0.760	0.000	0.000	0.000	0.000	0.000	0.000
	Mea06																0.000	0.000	0.000	0.000	0.000	0.000
	IB08																	0.000	0.000	0.000	0.000	0.000
	BI14																		0.000	0.000	0.000	0.000
	Gea19																			0.000	0.000	0.000
RGM	1																				0.026	0.000
	2																					0.000
	3																					

*Cell values are the probabilities that AUC samples for two models could have come from the same distribution. Values less than 0.05 are deemed "significant", in which case the model with significantly better performance is indicated via the cell shading.

Table 3.5 *P*-value matrix to compare modelperformance for the global dataset.

Statistically better*	↑	LPI						LPI_{ISH}						LSN						GGM	
←		RW98	AIJ01	Mea06	IB08	BI14	Gea19	RW98	AIJ01	Mea06	IB08	BI14	Gea19	RW98	AIJ01	Mea06	IB08	BI14	Gea19	1	2
LPI	RW98		0.166	0.046	0.446	0.933	0.682	0.898	0.467	0.759	0.696	0.435	0.894	0.571	0.224	0.263	0.244	0.377	0.369	0.000	0.000
	AIJ01			0.978	0.105	0.211	0.255	0.245	0.439	0.368	0.137	0.500	0.248	0.092	0.004	0.031	0.032	0.051	0.052	0.000	0.000
	Mea06				0.040	0.135	0.162	0.120	0.657	0.135	0.066	0.441	0.186	0.026	0.020	0.004	0.009	0.021	0.021	0.000	0.000
	IB08					0.355	0.101	0.582	0.338	0.565	0.887	0.144	0.521	0.857	0.346	0.420	0.400	0.569	0.555	0.000	0.000
	BI14						0.358	0.975	0.525	0.824	0.678	0.379	0.944	0.596	0.259	0.290	0.231	0.328	0.329	0.000	0.000
	Gea19							0.870	0.598	0.931	0.466	0.511	0.855	0.461	0.205	0.220	0.140	0.224	0.224	0.000	0.000
LPI_{ISH}	RW98								0.458	0.759	0.490	0.472	0.973	0.544	0.181	0.240	0.245	0.380	0.367	0.000	0.000
	AIJ01									0.582	0.301	0.815	0.475	0.247	0.005	0.074	0.113	0.163	0.157	0.000	0.000
	Mea06										0.527	0.787	0.819	0.361	0.077	0.070	0.165	0.250	0.240	0.000	0.000
	IB08											0.053	0.353	0.790	0.285	0.368	0.354	0.521	0.504	0.000	0.000
	BI14												0.076	0.319	0.134	0.154	0.097	0.158	0.154	0.000	0.000
	Gea19													0.557	0.206	0.256	0.215	0.325	0.313	0.000	0.000
LSN	RW98														0.258	0.154	0.142	0.362	0.321	0.000	0.000
	AIJ01															0.657	0.551	0.461	0.470	0.000	0.000
	Mea06																0.678	0.493	0.510	0.000	0.000
	IB08																	0.451	0.498	0.000	0.000
	BI14																		0.792	0.000	0.000
	Gea19																			0.000	0.000
GGM	1																				0.779
	2																				

*Cell values are the probabilities that *AUC* samples for two models could have come from the same distribution. Values less than 0.05 are deemed “significant”, in which case the model with significantly better performance is indicated via the cell shading.

As discussed, an AUC is widely used to study model behavior, but it reflects overall performance across all misprediction economies. To identify the most efficient model for particular economies, Cost′ is computed for each model at different CR values. The model with lowest Cost′ is identified in Figure 3.5 for CRs ranging from 0.01 to 2; results are presented for the Canterbury and global datasets in Figures 3.5(a) and 3.5(c), respectively. Also, because multiple models could have nearly equivalent Cost′, and thus, be equally optimal, any model whose Cost′ is within 1% of minimum is identified as "optimal." To assess the sensitivity of results to this criterion, analyses were repeated by relaxing the threshold to 10%, as shown in Figures 3.5(b) and 3.5(d).

While the models with highest AUC (see Figure 3.4) tend to appear in Figure 3.5 (i.e., they are optimal for some range of CR), the results convey more nuanced information than an AUC alone. For example, as seen in Figure 3.5(a) for the Canterbury dataset, geospatial model RGM3 is optimal in both the conservative, or "northeast," region of ROC space (low CR), and in the liberal, or "southwest", portion of ROC space (high CR). Thus, for scenarios in which either false negatives or false positives are relatively inconsequential, model RGM3 outperforms all others. While this may sound abstract, it is exactly the misprediction economy for critical facilities (e.g., powerplants, hospitals, etc.) in which C_{FN} tends to far exceed C_{FP}, making avoidance of the former paramount.

Conversely, geotechnical models BI14-LPI_{ISH} and Gea19-LPI_{ISH} are optimal in the range of $0.25 < CR < 1.75$, or scenarios in which C_{FN} and C_{FP} are relatively more similar. It can also be seen that models with lower AUC are sometimes optimal in specific regions of ROC space. For example, most striking is that geospatial model GGM2 is the most optimal model for the global dataset at low CR. This is despite the fact that its AUC, or overall prediction efficiency, was significantly lower than all geotechnical models. Extending the threshold for identifying "optimal" models to 10%, it can be seen that each of the 23 models evaluated is "optimal" for some range of CR. Thus, Figure 3.5 provides additional performance insights and demonstrates how misprediction economies may be considered when assessing or selecting prediction models.

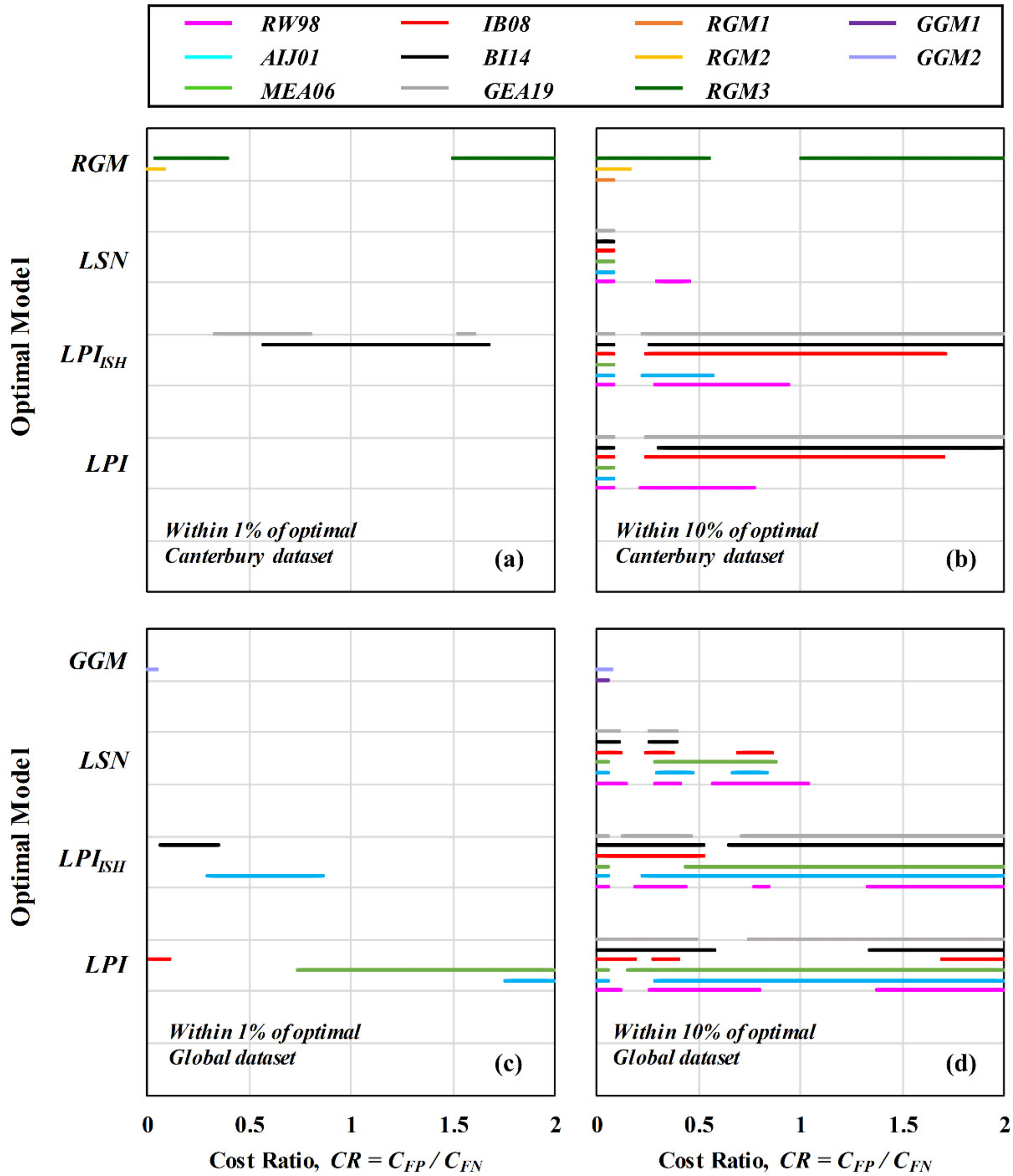

Figure 3.5 **Optimal liquefaction model as a function of CR, as determined from ROC analyses of the Canterbury dataset, where "optimal" models are those within (a) 1% and (b) 10% of optimal; analogous analyses are presented in panels (c) and (d) for the global dataset.**

3.5.1 Lessons for Geotechnical and Geospatial Models

Informed by the preceding analyses, four lessons for improving model performance are next highlighted.

1. First, while obvious, it is worth contextualizing the importance of interevent model stability. Given imperfect models "A" and "B", A may outperform B on all events individually, but B may outperform A when the data from all events is combined.

This is true of models tested here (e.g., BI14-LPI vs. RGM3). For the 2010 Darfield and 2011 Christchurch earthquakes, BI14-LPI has event-specific AUCs of 0.61 and 0.73, respectively. The threshold LPI values that minimize mispredictions in these events are 2.82 and 8.67, respectively. In contrast, the RGM3 event specific AUCs and threshold values for these respective earthquakes are 0.53 and 0.68, and 11.7 and 11.8. While BI14-LPI has better AUC in each individual event (i.e., better segregating sites with and without manifestations), the inter-event instability of its scaling, or the LPI value at which segregation is maximum, leads to it performing no better than RGM3 when the events are analyzed together. The relative success of geospatial models is due at least partly to this phenomenon. Thus, as demonstrated by BI14-LPI, identifying and addressing factors which cause inter-event instability is central to improving model performance;

2. Geospatial models have a difficult task: to accurately infer below-ground conditions from above-ground parameters. In this respect, the inability to predict soil type (and by corollary, liquefaction susceptibility) was a common cause of mispredictions for the models and cases studied herein. As seen in Table 3.3, these models generally expect ground to be susceptible to liquefaction if it is flat, saturated, and near rivers, streams, or coasts. However, as identified from global testing, such sites may consist predominately of soils less- or un-susceptible to liquefaction (e.g., clays, peats, or gravels). Moreover, we find in many of these cases that surface-geology maps accurately predict the predominance of such soils. Geospatial models could thus benefit from including mapped geologic data, when available, as well as other, yet unidentified proxies of soil type. In addition, the coarse resolution of some geospatial inputs (e.g., mapped rivers) hinders performance at the site-specific scale. Being central to their performance, more efficient and higher resolution predictors of subsurface properties must be identified for geospatial models to improve; and

3. Geospatial models inherently merge liquefaction triggering and manifestation. This calls attention to the "simplified" framework for developing geotechnical triggering models [Seed and Idriss 1971; Whitman 1971]—specifically to the interdependent relationship between triggering and manifestation. While the six triggering models tested herein have several post-1971 improvements (e.g., new or modified terms that account for influential factors), the fundamental approach to developing these models has never changed. Using this approach, an *in situ* test is performed where liquefaction was observed to have triggered or inferred to have not triggered. An analyst interprets the test data and ties the observed response of the profile to a "critical" stratum. For "no" cases—where no manifestation is observed—the "critical" stratum is the most susceptible stratum which, if liquefied, is conjectured to manifest at the surface. This is repeated for many case histories, and for each, the cyclic-stress demand in the critical stratum is plotted vs. a measured proxy of soil density (e.g., CPT resistance). Lastly, a "triggering curve" is regressed to define the relationship between the cyclic demand imposed on a soil and its capacity to

resist liquefaction. Within this process, the use of surface observations is problematic, since such observations are a function both of factors influencing triggering and factors influencing manifestation. To select the critical stratum, the analyst must therefore use a manifestation model in reverse (i.e., a model relating surface observations to triggering at-depth). This selection must be made such that the critical stratum's thickness, depth, density, fines content, plasticity, and strain-potential, in addition to considering all properties of all overlying strata, is consistent with the surface observation. If this is not achieved, then embedded in the derivative triggering curve will be factors that relate not only to liquefaction triggering, but also to the post-triggering manifestation of liquefaction. Thus, the manifestation model used by all analysts to date when developing triggering models has been personal judgement, rather than a defined analytical model, which is inherently problematic. Meanwhile, and predicated on the accuracy and "purity" of triggering models, a different set of researchers has separately proposed manifestation models that predict surface expressions from triggering (e.g., LPI, LSN) by considering the cumulative response of a profile. By inputting the results from triggering analysis (i.e., FS_{liq} vs depth) into manifestation models, the latter may be trained using case-history data (note that such data was also used to train triggering models, albeit using different, undefined manifestation models). Given that: (i) an effective manifestation model is required in order to formulate an effective triggering model, and (ii) an effective triggering model is required in order to formulate an effective manifestation model, it follows that (iii) these models should be developed harmoniously and iteratively within a consistent framework, just as required for inverse problems. Failure to do so potentially leads to the omission, double counting, and general obscuration of the mechanics controlling triggering and manifestation. While the effect on performance is unknown, the development of geotechnical triggering and manifestations models has been both historically and presently less than completely rational; and

4. Within the broader shortcomings just described, the multi-scale interactions that influence surface manifestation must be understood and modeled more completely. For example, it is known that low-permeability soils within or atop a profile can influence the morphology of manifestations (e.g., by effecting pore-pressure development and transmission). This has been documented in laboratory, numerical, and field research (e.g., Fiegel and Kutter [1994]; Ozutsumi et al. [2002]; Brennan and Madabhushi [2005]; Juang et al. [2005]; Özener et al. [2008]; Maurer et al. [2015b]; and Cubrinovski et al. [2019]). Despite this, only one of the manifestation models tested, LPI_{ISH}, considers the influence of soils expected not to liquefy, and it does so in a way that is insufficient for capturing their total influence. Other factors likely pertinent to surface manifestation (e.g., strata thickness, depth, sequencing, and permeability, among others) are either modeled in a generally heuristic manner or are not considered by LPI, LSN, and LPI_{ISH}. Accordingly, the performance of geotechnical models would surely benefit from a

more rigorous understanding of the mechanics and interactions that drive a soil profile's cumulative response.

3.6 SUMMARY AND CONCLUSIONS

Using 15,223 case-histories from 24 earthquakes, this study evaluated the performance of 23 liquefaction models based on geotechnical or geospatial data. Case histories were parsed into the "Canterbury" and "global" datasets and finite-sample uncertainty was used to test for significance. The most salient findings are as follows:

(i) For the Canterbury dataset, three models were either statistically better or not statistically different compared to all others: BI14-LPI_{ISH}, Gea19-LPI_{ISH}, and RGM3;

(ii) For the global dataset, the top-performing models were Mea06-LPI and AIJ01-LPI, yet finite-sample uncertainties yield these results inconclusive. The top-performing models in Canterbury may also be the top-performing models globally, but more global case-history data is needed to confirm this supposition or to draw other conclusions about performance;

(iii) Successive "simplified" geotechnical models proposed over the last 20 years show little or no demonstrable improvement. It is unlikely that fine-tuning of model parameters or incremental grown in training data will inflect this trend upwards. More likely, this would occur only with disruptive innovation to the *in situ* test method or fundamental modeling approach;

(iv) Geospatial models performed remarkably well for the Canterbury dataset, with one such model performing significantly better than most geotechnical models—a provocative result given the relative costs of model inputs;

(v) For the global dataset, all geotechnical models performed significantly better than all geospatial models, with the latter performing only marginally better than random guessing. This highlights the difficulty of inferring below-ground conditions from above-ground parameters, especially across diverse geomorphic, topographic, and climatic environs; and

(vi) Informed by the presented analyses, four paths to improving the performance of geotechnical or geospatial models were highlighted. These include: (a) identifying and addressing sources of interevent instability; (b) identifying better geospatial proxies of soil type, and by corollary, liquefaction susceptibility; (c) developing geotechnical triggering and manifestation models within a more rational and internally consistent framework; and (d) more rigorous investigation and modelling of the multi-scale interactions which drive a soil profile's cumulative response.

The findings of this study are tied to the data analyzed, which in effect is the present sum of CPT case histories. The applicability of these findings to other case-history data—particularly that with different parameter space (e.g., soils with unusual minerology, composition, age, etc.; earthquakes of large or small magnitude)—or to other models and methodologies, is unknown. In addition, the presented findings should be considered in the context of model regionality and potential bias. Ultimately, additional data will confirm or update the conclusions drawn above.

3.7 DATA

The global dataset was compiled from the following sources, parsed by event, and may soon be available in full or part from the Next-Generation Liquefaction project (e.g., Zimmaro et al. [2019]:

Table 3.5 Sources of global dataset parsed by year and event.

Year	Event	Sources
1964	M_w 7.6 Niigata, JPN	Ishihara and Koga [1981], Farrar [1990], Moss et al. [2003]
1971	M_w6.6 San Fernando, USA	Bennett et al., [1998], Toprak and Holzer [2003]
1975	M_w7.0 Haicheng, CHN	Arulandan et al. [1986], Shengcong and Tatsuoka [1984]
1976	M_w7.6 Tangshan, CHN	Shibata and Teparaska [1988], Moss et al. [2009; 2011]
1979	M_w6.53 Imperial Valley, USA	Diaz-Rodriguez [1984], Diaz-Rodriguez and Armijo-Palaio [1991], Moss et al. [2003]
1981	M_w5.9 Westmoreland, USA	Bennett et al. [1984], Seed et al. [1984], Cetin et al. [2000], Moss et al. [2005]
1983	M_w 7.7 Nihonkai-Chubu, JPN	Farrar [1990]
1983	M_w6.88 Borah Peak, USA	Andrus [1986], Andrus and Youd [1987], Moss et al. [2003]
1987	M_w6.6 Edgecumbe, NZ	Christensen [1995], Moss et al. [2003]
1987	M_w6.54 Superstition Hills, USA	Bennett et al. [1984], Cetin et al. [2000], Toprak and Holzer [2003], Moss et al. [2005], Holzer and Youd [2007]
1989	M_w6.93 Loma Prieta, USA	Mitchell et al. [1994], Pass [1994], Bennett and Tinsely [1995], Boulanger et al. [1995; 1997], Kayen et al. [1998], Toprak and Holzer [2003], Youd and Carter [2005]
1994	M_w6.69 Northridge, USA	Abdel-Haq and Hryciw [1998], Bennett et al., 1998, Holzer et al. [1999], Moss et al. [2003]
1995	M_w6.9 Hyogoken-Nambu, JPN	Suzuki et al. [2003]
1999	M_w7.51 Kocaeli, TUR	PEER [2000a], Youd et al. [2009]
1999	M_w7.62 Chi-Chi, TWN	Lee et al. [2000], PEER [2000b]
2008	M_w6.4 Achaia-Ilia, GRC	Batilas et al. [2014]
2008	M_w7.2 El Mayor-Cucapah, MEX	Moss et al. [2005]; CESMD [2016], Turner et al. [2016]
2011	M_w9 Tohoku, JPN	Cox et al. [2013], Boulanger and Idriss [2014]
2012	M_w6.1 Emilia, ITA	Papathanassiou et al. [2015], Facciorusso et al. [2015], Servizio Geologico [2016]

4 Part Three: On the Extension of Geospatial Liquefaction Models to Predict Magnitude of Ground Failure, Infrastructure Damage, and Economic Loss

While geospatial models have limitations that can and should be addressed via future research, their capacity for predicting liquefaction is promising, as demonstrated in Part Two. Accordingly, Part Three explores the extension of the Zhu et al. [2015; 2017] models to predict:

- the severity of liquefaction ejecta
- magnitude of ground settlement
- infrastructure damage and loss

With respect to infrastructure damage and loss, this study focused on structures built atop shallow foundation systems, which are common worldwide. These analyses focused on the Canterbury dataset, for which geospatial models performed well (i.e., the locations to be studied are those where geospatial models, in general, correctly predicted the occurrence and non-occurrence of liquefaction). These efforts represent a best-case scenario for predicting liquefaction consequences using geospatial models. Should this effort fail in Canterbury, it is unlikely that attempts elsewhere would prove successful. The formulation of damage and loss models is facilitated by unprecedented data resulting from the Canterbury earthquakes. In particular, 62,009 foundation-damage surveys and 53,940 insurance loss assessments are utilized. Geospatial models were found to efficiently predict not only the occurrence of liquefaction manifestation, but also its severity. In addition, it was found that geospatial models were relatively useful for predicting some modes of damage (e.g., global settlement), but not for predicting other significant modes (e.g., stretching, twisting, and separation of foundations). These failure modes are presumably dependent on asset- and site-specific details that geospatial models do not consider. Owing to this limitation, geospatial models are found to be incapable of predicting monetary loss. In all cases where the developed models may be useful to forward predictions, compete model details are provided.

4.1 PREDICTING SEVERITY OF LIQUEFACTION MANIFESTATIONS

While the binomial prediction of surficial liquefaction manifestation is important, the severity of such manifestation is likely a more useful predictor of damage to civil infrastructure. In other words, is minor, sporadic liquefaction predicted, or will it be severe and widespread? Clearly, the impact of these scenarios on civil infrastructure can be expected to differ greatly. Thus, the utility of geospatial models can be increased through the development of fragility functions that predict the specific severity of ground deformation. In this study, fragility functions were developed using the approach outlined below, similar to that described by Porter et al. [2006] for predicting damage to structural elements.

The probability of the surface manifestation of liquefaction reaching or exceeding a manifestation severity, MS, given a computed geospatial liquefaction index (GLI) value, is herein denoted F_{MS}(GLI) and idealized by a lognormal distribution, as is typical for fragility functions (e.g., Bradley, [2010]):

$$F_{\mathrm{MS}}(\mathrm{GLI}) = \Phi\left[\frac{\ln\left(\frac{\mathrm{GLI}}{x_m}\right)}{\beta}\right] \tag{4.1}$$

where Φ denotes the Gaussian cumulative distribution function; GLI is the probability (fractional form) of liquefaction manifestation computed by a geospatial model (i.e., the "geospatial liquefaction index"); x_m is the distribution median, and β is the logarithmic standard deviation.

While several approaches exist for fitting functions to data, this study utilized the maximum likelihood method described in Porter [2016], which identifies the model parameters with the highest likelihood of producing the observed data. Specifically, the case histories are grouped into *m* bins of similar GLI, where bins have index *i,* average value GLI_i, and contain n_i cases, of which f_i are cases in which observed manifestations reached or exceeded MS. Assuming quantity f_i can be estimated from a binomially distributed random variable, F_i, Equation (4.2) gives the probability of observing quantity f_i among n_i cases, if the probability of an individual case exceeding MS is given by Equation (4.1).

$$P\left[F_i = f_i\right] = \frac{n_i!}{f_i!\left(n_i - f_i\right)!} \cdot p_i^{f_i} \cdot \left(1 - p_i\right)^{n_i - f_i} \tag{4.2}$$

In Equation (4.2), p_i is defined by Equation (4.1), evaluated at the GLI_i. Lastly, the values of parameters x_m and β that maximize the likelihood of producing the observed data are determined. This likelihood is given by the product of the probabilities in Equation (4.2), multiplied over all bins:

$$L\left(X_m, \beta\right) = \prod_{i=1}^{\mathrm{m}} P\left[F_i = f_i\right] \tag{4.3}$$

Using this approach and approximately 15,000 case-histories compiled from the Canterbury earthquakes, fragility functions were developed for two geospatial models: GGM2 and

RGM3. These models were chosen because they were the best-performing models for the global and Canterbury datasets, respectively, as determined from ROC analyses presented in Part 1 of this report. Also as described in Part Two, the severity of liquefaction manifestation was classified for each of the ~15,000 case-histories using the Green et al. [2014] criteria, which classifies the severity of liquefaction ejecta as either: “none”, “minor”, “moderate”, or “severe”.

The resulting fragility functions are shown in Figure 4.1 for geospatial models GGM2 and RGM3, respectively. In addition, coefficients (i.e., X_m and β values) are provided in Table 4.1 for all functions graphed in Figure 4.1. These functions compute the probabilities of reaching or exceeding three manifestation severities (MS), where the MS is that classified per the Green et al. [2014] criteria. Using the coefficients provided in Table 4.1, analysts may extend the Zhu et al. [2015; 2017] geospatial models to predict MS.

It can be seen in Figure 4.1 that each of these geospatial models are capable of predicting not only the binomial occurrence of liquefaction ejecta, but also its severity (i.e., extent and intensity), which should better relate to damage potential. In other words, as the GLI increases, so too does the probability of exceeding a given MS. It should be emphasized that these functions were developed from and apply to the Canterbury dataset. Discretion should be used when applying these functions to other locales (i.e., to earthquakes worldwide).

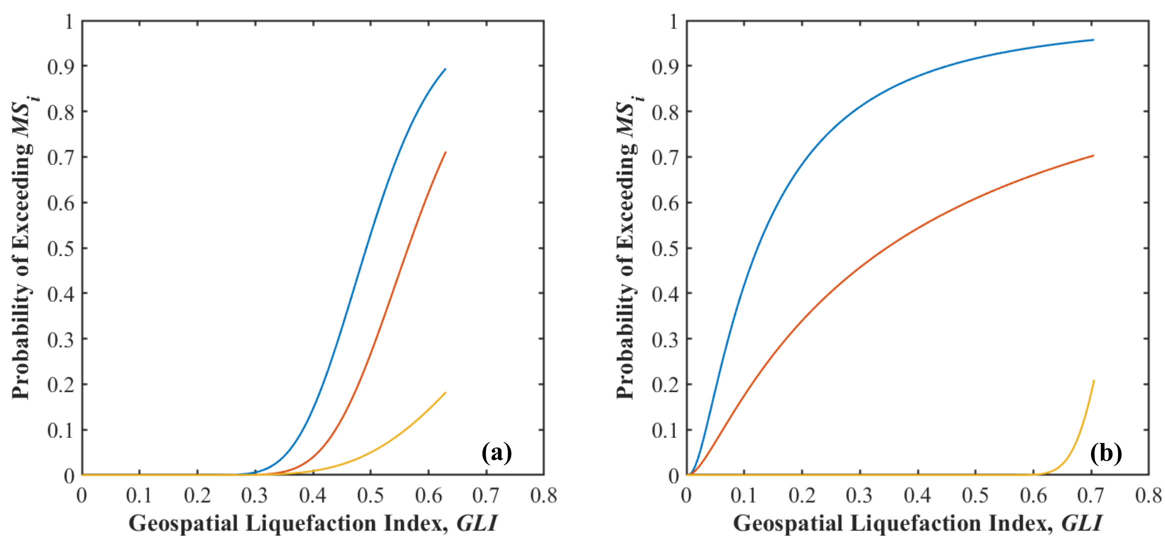

Figure 4.1 **Fragility functions for predicting the severity of ground failure using the: (a) GGM2 global geospatial model; and (b) RGM3 region-specific geospatial model.**

Table 4.1 Fragility-function coefficients for geospatial models GGM2 and RGM3 (plotted in Figure 4.1), which can be used to predict the probability of exceeding a given severity of liquefaction manifestation.

	GGM2		RGM3	
Manifestation severity (*MS*)	x_m	β	x_m	β
Minor	0.4924	0.1970	0.1231	1.0141
Moderate	0.5659	0.1963	0.3467	1.3303
Severe	0.8359	0.3121	0.7457	0.0694

4.2 PREDICTING GROUND SETTLEMENT

Vertical and horizontal ground deformation data was obtained from the New Zealand Geotechnical Database (NZGD, 2012) for the M_w6.2, 22 February 2011 Christchurch earthquake. These deformations were measured via airborne LIDAR following the earthquake and include local liquefaction-induced movements as well as regional tectonic movements associated with the event. To isolate liquefaction-induced deformations, tectonic movements [NZGD 2012] were first subtracted from LIDAR measurements. While airborne LIDAR enabled deformations to be efficiently measured across a very large area, it comes with the trade-off of a +/- 7-cm measurement accuracy [NZGD 2015]. Due to this uncertainty, many negative settlements (i.e., inferred ground heave) were observed across the study area that may not reflect actual conditions. Despite this relatively large measurement uncertainty, the LIDAR data allows for significantly more settlement case histories to be compiled than in all previous earthquakes combined.

While settlement data is available from four major Canterbury earthquakes—the four September 2010 M_w7.1, 22 February 2011 M_w6.2, 13 June 2011 M_w5.9, and 23 December 2011, M_w5.9 earthquakes—we choose to focus only on the February 2011 earthquake for the following reasons. First, the 13 June and 23 December data are complicated by the fact that multiple, similar-magnitude events occurred only minutes-to-hours apart. As a result, pore pressures were elevated at the time of latter events (complicating predictions), and LIDAR data captured the effects of multiple earthquakes, which complicated analysis of the measurements. Second, because pre-earthquake reference LIDAR is of lower quality, the measurement uncertainty of settlements induced by the 4 September event (15 cm) is twice that of subsequent events (7 cm). Therefore, the settlement case histories compiled from the February 2011 event represent the highest quality data available.

Using this data, observed settlements were plotted as a function of geospatial model values (i.e., the computed probability of liquefaction manifestation) in Figures 4.2 and 4.3 for models GGM2 and RGM3, respectively. It can be seen the correlation between observed settlement and geospatial model values is relatively weak; moreover, the settlements are predicted even for geospatial model values of zero. Thus, even though these same models performed well in predicting manifestations of liquefaction, they appear to be poor predictors of free-field ground settlement. Note: popular geotechnical models developed specifically for predicting ground settlement have previously been shown to also perform very poorly on this dataset [Geyin and Maurer 2019a]. Accordingly, the poor correlation between settlement and geospatial model-predictions could be due to the large (and potentially biased) uncertainty in "observed" settlements. Unfortunately, given the means of data collection and processing, it is not straightforward to evaluate whether the observed measurements are in fact biased; in the authors' opinion, this is likely. Nonetheless, from this analysis of the Canterbury dataset, it must be tentatively concluded that while geospatial models can efficiently predict liquefaction ejecta (both its occurrence and severity), they are relatively incapable of predicting the magnitude of ground settlement. While functions for predicting settlement are defined in Figures 4.2 and 4.3, they are not recommended for use in forward analyses.

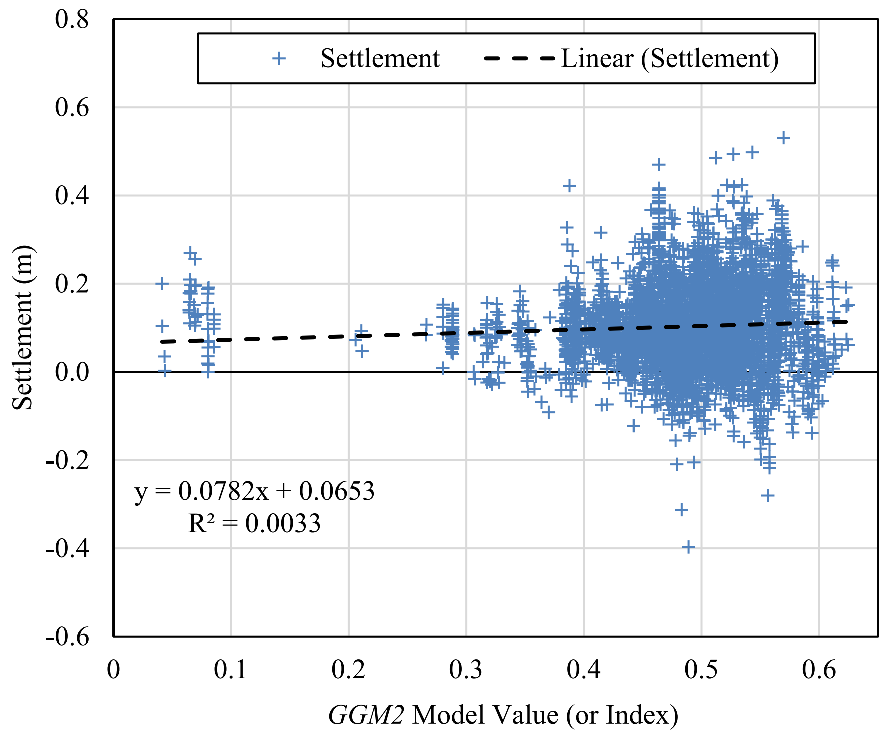

Figure 4.2 GGM2 model value vs. measured ground settlement.

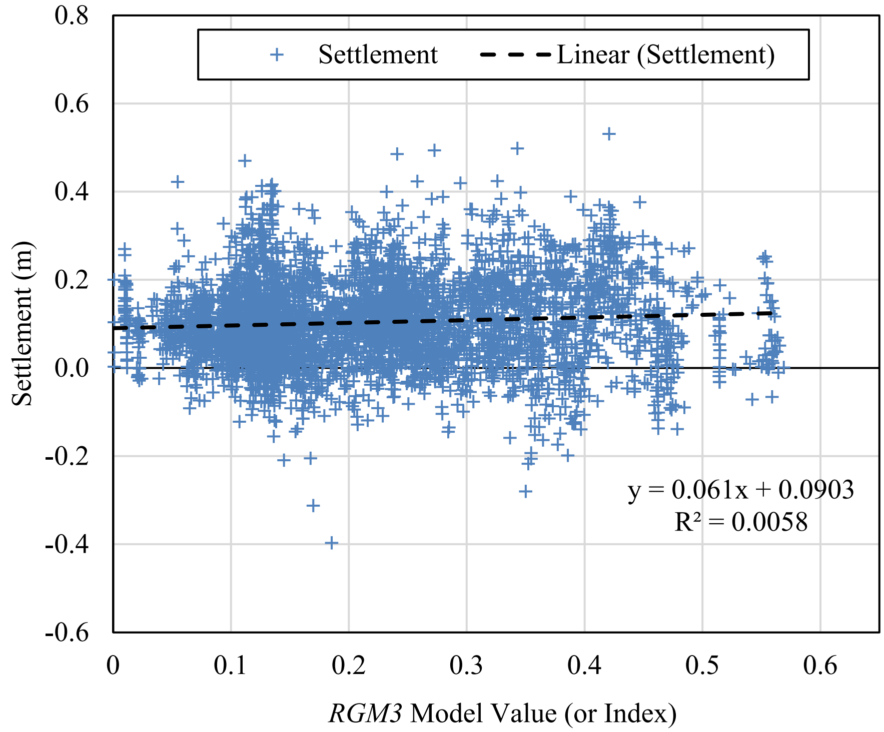

Figure 4.3 RGM3 model value vs. measured ground settlement.

4.3 PREDICTING PHYSICAL DAMAGE TO INFRASTRUCTURE

While predicting the manifestation of liquefaction in the free field (e.g., sand boils or ground settlement) is an important component of liquefaction hazard assessment, the ensuing physical damage and monetary loss are arguably of greatest importance. Accordingly, fragility functions were developed using post-earthquake performance data from the Canterbury earthquakes. In this regard, the present study focused on the performance of structures founded atop shallow foundation systems, which are common worldwide and particularly prone to liquefaction damage. The realization of these functions was facilitated by post-earthquake damage surveys of 62,000 structures founded on several variants of shallow foundation and overlying potentially liquefiable soils. These surveys were performed under the auspices of the New Zealand Earthquake Commission (EQC) and were compiled by Taylor and Tonkin, Ltd. A team of more than 400 engineers performed the surveys throughout the Canterbury earthquake sequence, documenting both the mechanism (i.e., mode) and magnitude of damage observed.

The shallow foundations were categorized into four variants:

- timber floors on shallow piles
- timber floors on internal shallow piles with perimeter concrete footings
- concrete slab-on-grade
- mixed or unknown shallow foundations

Surveyors parsed damages into seven different modes, as depicted in Figure 4.4:

- stretching
- hogging
- dishing
- twisting
- tilting
- discontinuous foundation
- global settlement

Each mode of damage was also classified as “minor”, “moderate”, or “severe” based on the measured magnitude of deformation. As shown in Figure 4.4, global settlements were deemed “minor” if less than 5 cm; “moderate” if between 5 and 10 cm; and “major” if exceeding 10 cm. In some instances, multiple modes of damage were observed and recorded. In total, 62,000 unique sites were inspected for foundation damage.

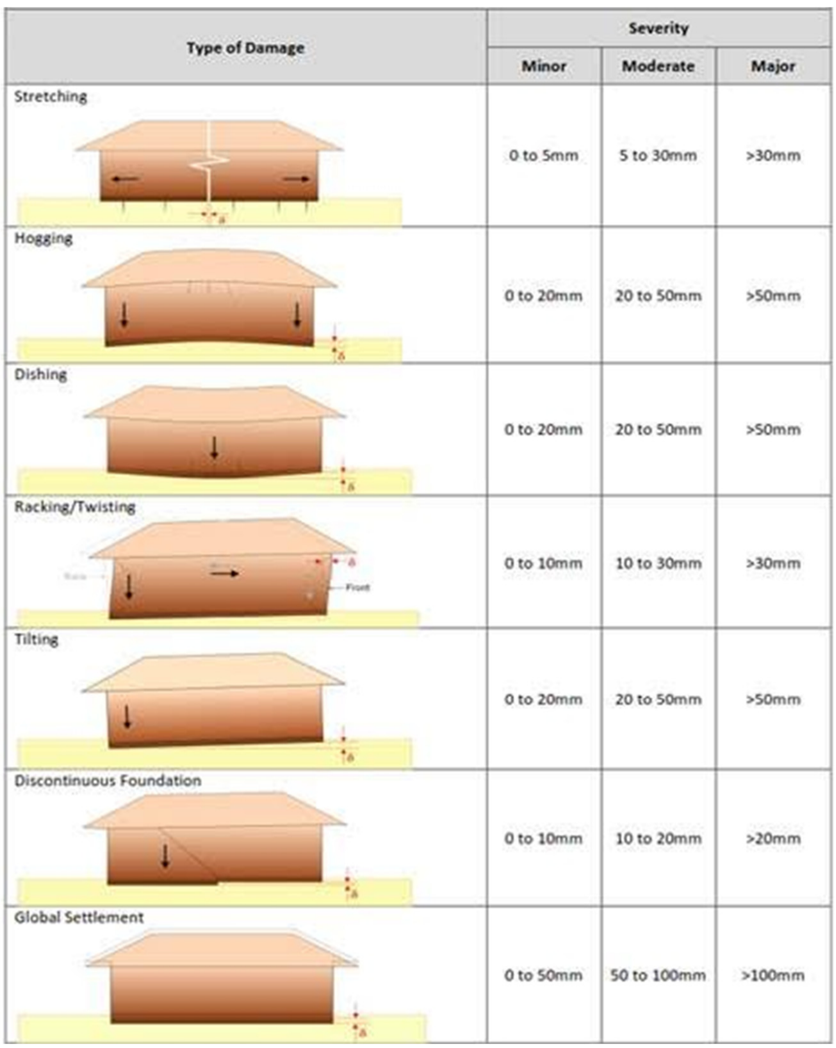

Type of Damage	Severity		
	Minor	Moderate	Major
Stretching	0 to 5mm	5 to 30mm	>30mm
Hogging	0 to 20mm	20 to 50mm	>50mm
Dishing	0 to 20mm	20 to 50mm	>50mm
Racking/Twisting	0 to 10mm	10 to 30mm	>30mm
Tilting	0 to 20mm	20 to 50mm	>50mm
Discontinuous Foundation	0 to 10mm	10 to 20mm	>20mm
Global Settlement	0 to 50mm	50 to 100mm	>100mm

Figure 4.4 Foundation-damage mechanisms and severity classifications.

While many properties were inspected multiple times, most were not inspected after every individual earthquake comprising the Canterbury sequence. In the cases where inspections were repeated multiple times for a given foundation (e.g., an inspection was performed after the September 2010 event *and* after the February 2011 event), the results were compared to account for compounding damages. In other words, if a foundation was classified as having "moderate" damage after both the September and February earthquakes, it was assumed that the February earthquake did not contribute any new damage. Similarly, later inspections with a greater severity of classified damage than a previous inspection were reduced in accordance with the previous classification damage was "minor" after the September 2010 earthquake and "moderate" after the February 2011 earthquake, it was assumed that the latter was responsible for the difference. Additionally, some foundations were only inspected once, or were only inspected after experiencing multiple earthquakes, in which case the observe damage could have conceivably occurred in one of several earthquakes. In these cases, the observed damage severity was distributed among prior events using the computed geospatial model values:

$$\text{Event severity} = \text{survey severity} * \frac{\text{event GLI}}{\sum(\text{previous event GLI}' + \text{survey event GLI})} \quad (4.4)$$

where the GLI is the computed geospatial model value, or "geospatial liquefaction index," which ranges from 0 to 1. Thus, Equation (4.4) assumes that events in which the GLI was greater were responsible for more damage, and vice-versa. While these assumptions are less than ideal, they allow for a significantly larger dataset to be analyzed.

Using this dataset, a total of 240 fragility functions were developed using the same methodology previously described in this report. In particular, functions were formulated for the seven damage modes and three damage severities shown in Figure 4.4. In addition, functions were developed for predicting the severity of damage, independent of damage mode (i.e., the greatest severity of damage, regardless of which mode it was associated with). These efforts were repeated for the four types of shallow foundation system named previously, and for the case where all variants of shallow foundation were grouped together. These latter functions may be more desirable for general, large-scale analyses in which parcel-specific information is unavailable, but where it may be reasonably assumed that most structures are on some variant of shallow foundation. As was done previously for MS and ground settlement, two geospatial models were evaluated for predicting foundation damage: GGM2 and RGM3. These models were chosen because they were the best-performing models for the global and Canterbury datasets, respectively, as determined from ROC analyses; see Part 2.

The resulting fragility functions for RGM3 are presented in Figure 4.5 for the case where all variants of shallow foundation are grouped together. In many ways, the findings to be discussed with respect to Figure 4.5 are also representative of those for the GGM2 model, and for specific foundation types. The coefficients for all fragility functions shown in Figure 4.5 are provided in Table 4.2, allowing analysts to use the developed functions in forward analyses. However, as can be seen in Figure 4.5, the utility of these functions is generally limited. For most damage modes, the functions indicate very low probabilities of exceedance, even when geospatial models predict severe liquefaction. In other words, the geospatial model is not well-correlated to the occurrence or severity of foundation damage. In some cases, fragility functions could not be fit to the data using the lognormal CDF, which requires a positive correlation between the predictive index (geospatial model) and the outcome (foundation damage). In these cases, the data to be fit is shown, but fragility functions are not provided.

This lack of correlation might be attributable to the fact that some failure modes strongly depend on “meso scale” details (e.g., asset- and site-specific features) that are inadequately predicted by relatively coarser, “macro scale” geospatial data. As an example, damage modes like stretching and dishing likely depend on the exact geometry of the foundation, the quality of its construction, and the spatial variability of the subsurface. If so, these factors are obviously not considered by the geospatial model; therefore, they should not be expected to accurately predict response. In contrast, some of the developed functions (e.g., global settlement) do appear useful. That is, the geospatial model demonstrates a capability to predict damage. This distinction may arise from the fact that some damage modes are less dependent on site- and asset-specific features. If the subsurface is relatively homogeneous and liquefiable (and we know geospatial models can predict liquefaction), then the models appear relatively more capable of predicting damage if it manifests in the form of global settlements or tilting (which tend to be strongly correlated).

Provided in Appendix B of this report are the complete set of 240 fragility functions for specific foundation types and for the GGM2 model. Coefficients are also provided in Appendix B for each of the 240 functions, provided the data could be fit with the lognormal CDF. When this effort failed, it generally indicates that little-to-no correlation exists between the outcome and predictor. From the functions presented in Appendix B, findings for specific foundation types were generally the same as when all foundation variants were combined. This is somewhat surprising, given the expectation that different shallow foundation designs could be expected to perform differently (i.e., sustain lesser or greater damage when liquefaction occurs). Similarly, the functions for global model GGM2 were likewise mixed but generally limited in their success. As was the case with the regional model, damage modes that were less dependent on site- and asset-specific features (e.g., structural geometry, construction quality, subsurface variability, ground slope) were apparently easier to predict via geospatial data.

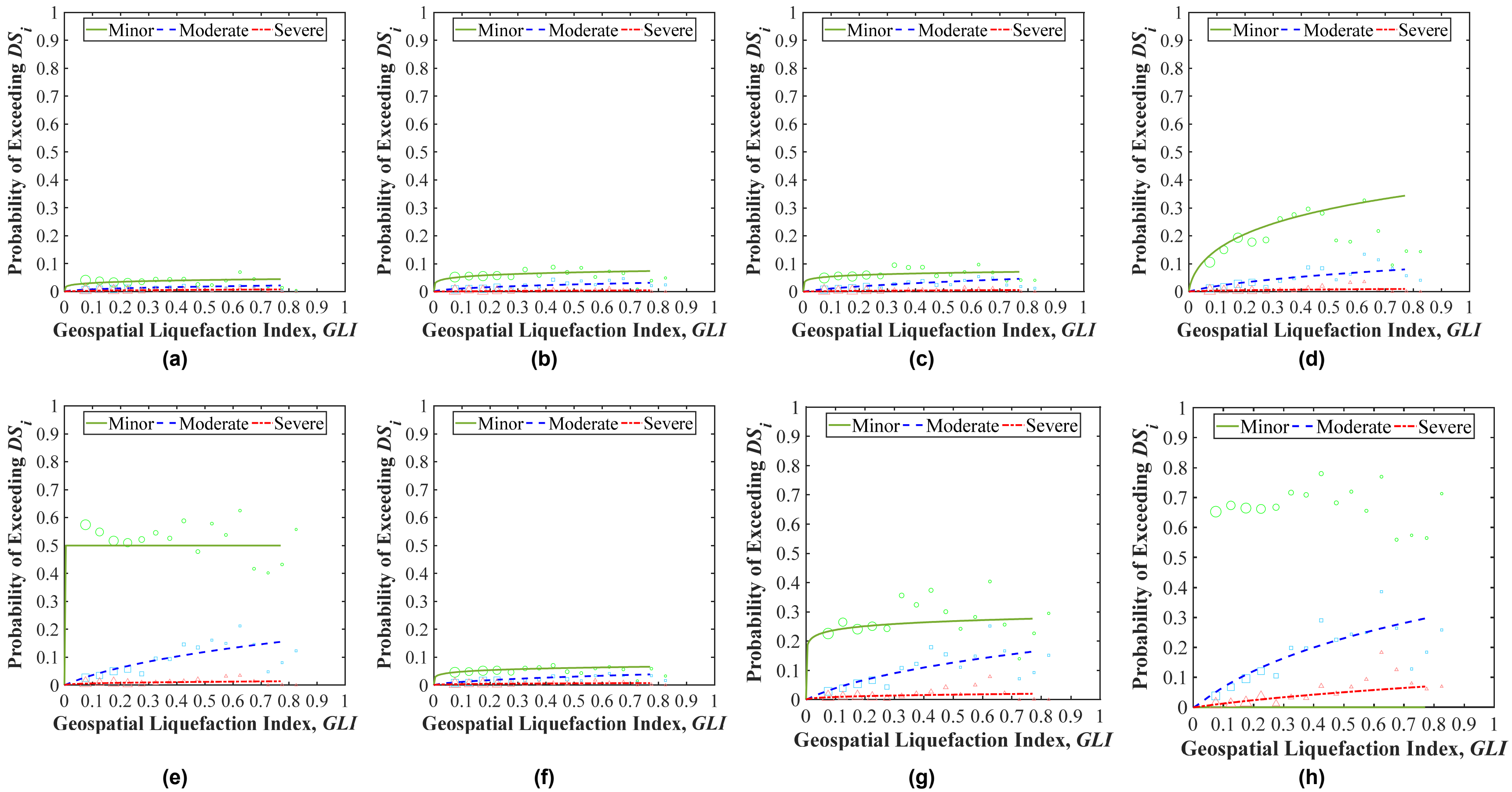

Figure 4.5 **Fragility functions for predicting the probability of damage to shallow foundations (all variants) using regional geospatial model RGM3: (a) stretching failure; (b) hogging failure; (c) dishing failure; (d) global settlement failure; (e) twisting failure; (f) discontinuous foundation failure; (g) tilting failure; and (h) the greatest observed damage severity, independent of failure mode.**

Table 4.2 Fragility-function coefficients for geospatial model RGM3 (plotted in Figure 4.5), which can be used to predict the probability of liquefaction-induced foundation damage exceeding a given severity, as defined in Figure 3.4).

			Stretching	Hogging	Dishing	Twisting	Tilting	Discontinuous foundation	Global settlement	Worst (all)
Timber floor on piles (Type A)	Minor	β	0.078	16.930	15.290	-	24.548	-	4.954	-
		x_m	1.449	3579715134.903	1464296169.904	-	365609.132	-	17.761	-
	Moderate	β	5.133	5.209	7.830	2.899	1.884	4.903	2.818	2.370
		x_m	73527.350	7220.297	3529586.069	15.665	3.151	8470.387	38.399	3.084
	Severe	β	6.846	0.117	0.117	6.754	7.110	0.117	8.984	3.630
		x_m	34879262.158	16.153	16.153	2811468.136	4142715.733	16.153	2866924982.818	230.295
Timber on internal piles with perimeter concrete footing (Type B)	Minor	β	10.877	12.375	12.237	-	10.348	11.452	3.451	-
		x_m	60115066.790	8700668.925	17676579.826	-	179.343	16802492.747	5.717	-
	Moderate	β	8.781	5.681	4.344	2.926	3.162	5.451	3.038	2.231
		x_m	155216559.280	25013.577	1864.084	16.269	23.475	24604.890	58.448	2.560
	Severe	β	8.305	6.676	8.399	9.131	7.449	11.491	6.037	2.615
		x_m	596434178.231	19365811.836	1346455813.461	446729231.433	4123055.832	1232641633278.430	2067746.754	31.646
Concrete Ssab on grade (Type C)	Minor	β	15.790	10.109	-	-	16.962	10.422	3.895	-
		x_m	284531612543.277	11115828.039	-	-	13054.515	4562906.457	4.141	-
	Moderate	β	3.659	3.500	2.013	2.755	3.569	4.339	2.193	2.397
		x_m	757.466	653.472	13.199	18.869	45.746	2741.985	9.329	4.062
	Severe	β	1.946	3.087	5.077	2.732	5.871	2.297	4.450	2.975
		x_m	35.695	1576.805	143309.416	250.134	132947.483	127.870	20176.974	85.422
Mixed foundations (Mixed foundations)	Minor	β	15.062	10.181	-	-	8.452	11.966	3.677	-
		x_m	5103886.446	88898.082	-	-	1.419	178572.180	1.896	-
	Moderate	β	13.861	11.181	5.656	7.154	3.366	6.183	5.249	2.469
		x_m	75906344189.413	315569458.331	7939.727	3453.424	10.297	10804.985	1102.818	1.773
	Severe	β	0.117	6.439	5.688	14.389	8.516	12.585	8.772	2.385
		x_m	16.153	2401770.649	864209.823	389815492927.571	961245.538	289653696327.526	55254278.802	9.426
All Foundations	Minor	β	12.013	11.999	14.918	-	17.147	13.108	3.219	-
		x_m	546198426.962	26795894.400	2530161618.342	-	19932.695	291675689.965	2.810	-
	Moderate	β	5.318	4.829	3.428	2.602	2.610	4.095	3.163	2.117
		x_m	34125.943	5985.564	247.960	10.802	9.882	1075.954	65.977	2.385
	Severe	β	6.514	4.972	5.670	6.946	6.632	8.743	6.132	2.688
		x_m	5165746.808	302650.524	1232623.327	3420789.598	628953.677	1429244855.777	1299018.521	41.231

4.4 Predicting Monetary Loss

Whereas insurance loss assessments are typically private and closely guarded, the unique role of the New Zealand government as a land insurer led to their assessment of losses for 53,940 structures affected by liquefaction. To assist with processing insurance claims during the Canterbury sequence, assessors were sent to every insured property to assess the repair/rebuild cost. In conjunction with the replacement cost, the cost of liquefaction-induced damage can be computed as a fraction of replacement cost, defined herein as the building damage ratio (BDR). Accordingly, if the BDR equals 1, the cost of repairing damage is equal to the cost of replacing the structure. Larger BDRs therefore indicate greater losses. Accordingly, using methodology and reasoning similar to that presented in the previous section of this report, the development of functions for predicting BDR, conditioned on the RGM3 or GGM2 geospatial models, was explored. In performance-based earthquake engineering lexicon, these are often referred to as "vulnerability" functions; if successful, they allow losses from liquefaction to be rapidly estimated in near-real-time after an earthquake.

Considering all variants of shallow foundation, BDR values were plotted versus RGM3 and GGM2 geospatial model values in Figures 4.6 and 4.7, respectively. Using linear regression, functions were fit the medians of the binned data; the 16th and 84th percentile values from each BDR bin are also shown and indicate a large degree of uncertainty. As an example, at an RGM3 value of 0.6, the 16th–84th percentile range of BDR is 0.05 to 0.53. Moreover, it can be seen in Figure 4.6 that the correlation between BDR and RGM3 is relatively weak and only slightly positive. As the geospatial model predicts increasingly more severe liquefaction, the expected monetary loss should likewise increase, but it does not. The situation is worse for global geospatial model GGM2, which is negatively correlated to BDR, meaning that as the expected severity of liquefaction increases, the expected monetary loss from liquefaction decreases.

While these results are disappointing, they are unsurprising when considering the inability of the geospatial models to predict all modes of damage. It was previously shown that while geospatial models are relatively useful for predicting some modes (e.g., global settlement of foundations), they appear not to capture other significant and very costly modes (e.g., stretching, twisting, and separation of foundations), which are presumably dependent on asset- and site-specific details that geospatial models do not consider. Given the inability of the RGM3 and GGM2 models to predict all modes of damage, they cannot be expected to accurately predict loss, given that some component of loss is associated with damage modes that were poorly predicted. Accordingly, while functions are provided in Figures 4.6 and4.7 for extending geospatial models to predict loss, they are not recommended for use at the present time.

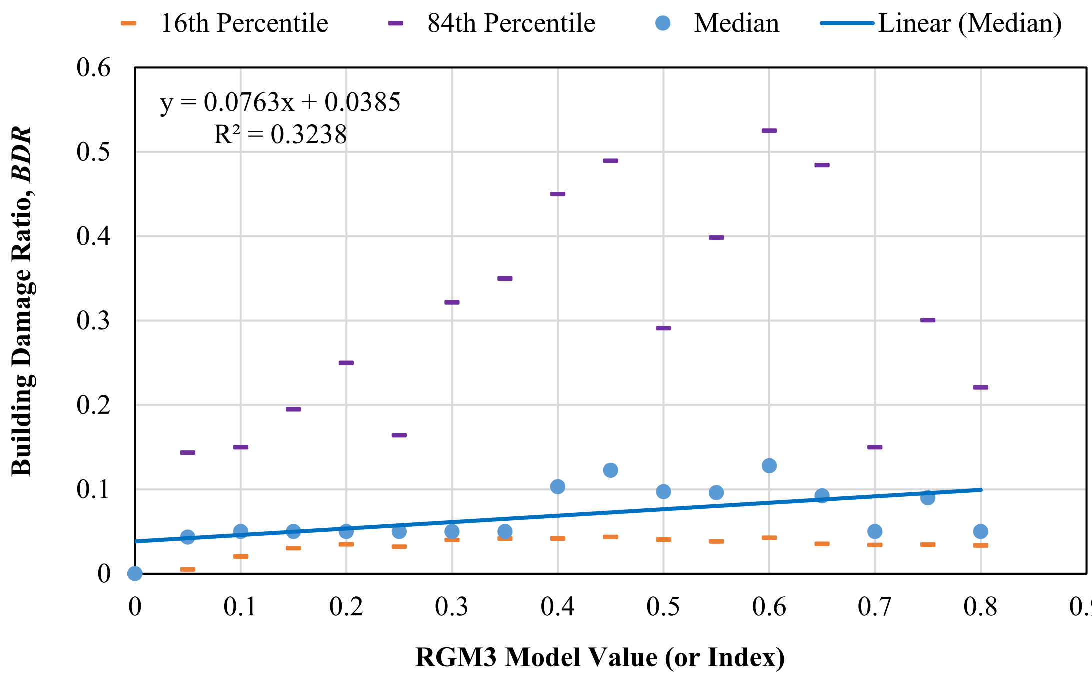

Figure 4.6 RGM3 model value vs. building damage ratio, which can be used to predict monetary loss resulting from liquefaction-induced damage.

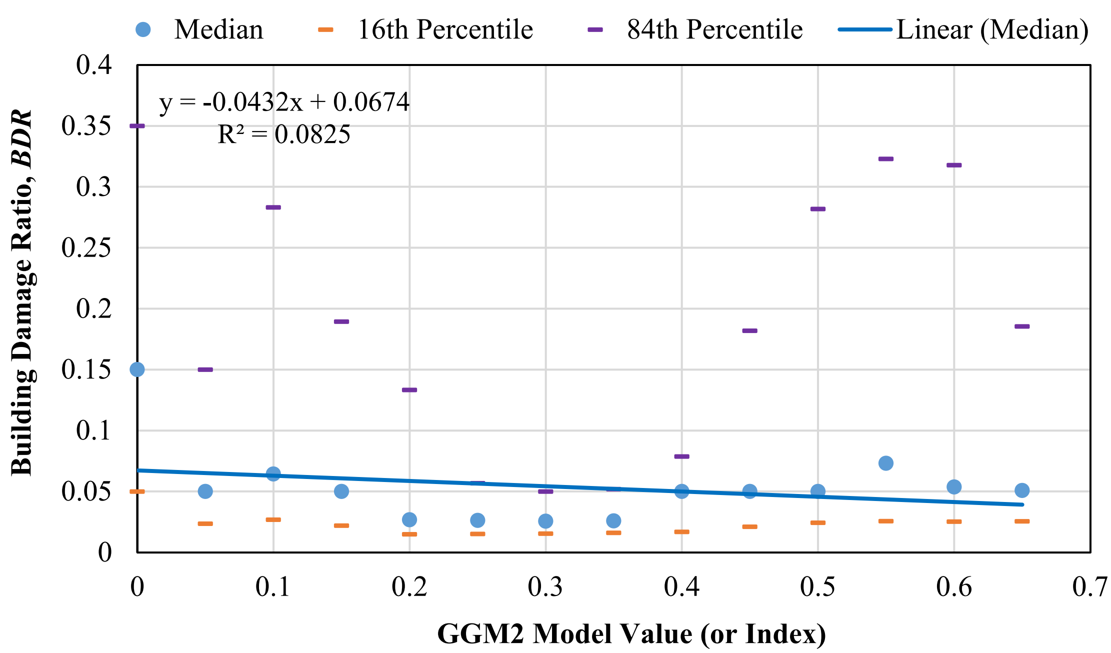

Figure 4.7 GGM2 model value vs. building damage ratio, which can be used to predict monetary loss resulting from liquefaction-induced damage.

4.5 Overall Project Conclusions and Recommendations

The most salient conclusions of this study are summarized as follows:

1. Geospatial models demonstrate provocative potential for predicting the occurrence and severity of surficial liquefaction manifestations in the free field. Moreover, these models outperform geotechnical models (which are far costlier and time-consuming to implement) for large subsets of the data analyzed;
2. Geospatial models were significantly less efficient on a global scale (i.e., when considering all case histories worldwide) and provided predictions much closer to random guessing than to perfection. This highlights the inherent difficulty of predicting what is *below* the ground using only information from *above* the ground. Efficient geospatial models may be developed for certain locales, but the development of a single model that efficiently predicts subsurface traits across various seismological, geological, geomorphic, and climatic settings is inherently challenging. Given these findings, the global "portability" of geospatial models must be improved and should be a future research priority. Results from the testing of geotechnical vs. geospatial models provide useful insights for improving the latter. Specific lessons and pathways for achieving this have been presented herein;
3. Functions were developed to predict infrastructure damage and loss using geospatial models. These functions were developed for several specific types of shallow foundation and for several specific modes of foundation failure. In addition, functions combining all foundation types and all modes of failure were developed. These broadly applicable functions do not require asset-specific information (i.e., the specific type of foundation) and attempt to predict the severity of damage independent of the associated failure mode. These functions may be more desirable for general, large-scale analyses. However, the utilities of the developed functions are generally limited, regardless of whether asset-specific information is available. This may be attributable to the fact that some failure modes strongly depend on "meso-scale" details (e.g., building geometry, construction quality, subsurface variability) that are inadequately captured by "macro-scale" geospatial data;
4. Lastly, considering (a) the relatively poorer performance of geospatial models globally; (b) the relative inability of the models to predict liquefaction consequences (even when the models efficiently predict liquefaction); (c) the primary applications of the models (e.g., post-earthquake reconnaissance and response; regional simulations); and (d) the seminal state of geospatial model-development, it is the authors' opinion that near-term investment should focus on model improvement, rather than model extension. Research that improves the capacity to predict liquefaction (e.g., via development of new models or modification of existing models) is likely to be more impactful than research that adapts existing models for prediction of downstream consequences. Geospatial

liquefaction models have demonstrated surprising and provocative potential, but also significant room for improvement.

REFERENCES

Abdel-Haq A., Hryciw R.D. [1998]. Ground settlement in Simi Valley following the Northridge earthquake, *J. Geotech. Geoenviron. Eng.,* 124(1):80–89, https://doi.org/10.1061/(ASCE)1090-0241[1998]124:1(80).

Abrahamson N.A., Youngs R.R. (1992). A stable algorithm for regression analyses using the random effects model, *Bull. Seismol. Soc. Am.* 82(1):505–510.

Ahmadi M.M., Robertson P.K. [2005]. Thin-layer effects on the CPT q_c measurement, *Can. Geotech. J.,* 42(5):1302–1317, https://doi.org/10.1139/t05-036.

Allstadt K.E., Thompson E.M., Hearne M., Wald D.J., Fee J.M., Martinez E.M., Hunter E., Brown J.D. (2019). The new USGS near-real-time ground failure product and its performance for recent earthquakes. *Seismological Society of America Annual Meeting*, Seattle, WA.

Andrus R.D., Youd T.L. (1987). Subsurface investigation of a liquefaction-induced lateral spread Thousand Springs Valley, Idaho, *Misc. Paper GL-87-8*, U.S. Army Corps of Engineers, Waterways Experiment Station, Vicksburg, MS.

Andrus R.D., (1986). *Subsurface Investigations on a Liquefaction Induced Lateral Spread, Thousand Springs Valley, Idaho: Liquefaction Recurrence and a Case History in Grave*l, M.S. Thesis, Dept. of Civil Engineering, Brigham Young University, Provo, Utah.

Anselin L. (1995). Local indicators of spatial association—LISA, *Geogr. Anal.,* 27(2):93–115, https://doi.org/10.1111/j.1538-4632.1995.tb00338.x.

Arango I., Lewis M.R., Kramer C. (2000). Updated liquefaction potential analysis eliminates foundation retrofitting of two critical structures, *Soil Dyn. Earthq. Eng*., 20:17–25, https://doi.org/10.1016/S0267-7261(00)00034-8.

Architectural Institute of Japan (200). *Recommendations for Design of Building Foundations*, 486 pgs.

Arulanandan K., Yogachandran C., Meegoda N.J., Ying L., Zhauji S. (1986). Comparison of the SPT, CPT, SV and electrical methods of evaluating earthquake induced liquefaction susceptibility in Ying Kou City during the Haicheng earthquake, *Geotechnical Special Publication,* 6:389–415, ASCE.

Batilas A., Pelekis P., Vlachakis V., Athanasopoulos G. (2014). Soil liquefaction/nonliquefaction in the Achaia-Ilia (Greece) 2008 earthquake: Field evidence, site characterization and ground motion assessment, *Inter. J. Geoeng. Case Hist*., 2(4):270–287, https://doi.org/10.4417/IJGCH-02-04-03.

Begg J., Jones K. (2012). 20,000 years of time in Christchurch, *Presentation to New Zealand Geotechnical Society*, Canterbury Branch, June 28, 2012, New Zealand Geotechnical Society, Wellington, NZ.

Bennett M.J., Tinsley J.C. III (1995). Geotechnical data from surface and subsurface samples outside of and within liquefaction-related ground failures caused by the October 17, 1989, Loma Prieta earthquake, Santa Cruz and Monterey Counties, California, *U.S. Geological Survey Open-File Report 95-663*, Menlo Park, CA, https://doi.org/10.3133/ofr95663.

Bennett M.J., McLaughlin P.V., Sarmiento J.S., Youd T.L. (1984). Geotechnical investigation of liquefaction sites, Imperial Valley, California, *U.S. Geological Survey Open-File Report 84-252*, https://doi.org/10.3133/ofr84252.

Bennett M.J., Ponti D.J., Tinsley J.C., III, Holzer, T.L., and Conaway, C.H., [1998]. Subsurface geotechnical investigations near sites of ground deformations caused by the January 17, 1994, Northridge, California, earthquake, *U.S. Geological Survey, Open-File Report 98-373*, https://doi.org/10.3133/ofr98373.

Beven K.J., Kirkby M.J. (1979). A physically based, variable contributing area model of basin hydrology, *Hydrol. Sci. Bull.*, 24:43–69, https://doi.org/10.1080/02626667909491834.

Boulanger R.W., DeJong J.T. (2018). Inverse filtering procedure to correct cone penetration data for thin-layer and transition effects, *Proceedings, Cone Penetration Testing 2018*, M.A. Hicks, F. Pisano, and J.P. Peuchen, eds., Delft University of Technology, The Netherlands, pp. 25–44.

Boulanger R.W., Idriss I.M. (2006). Liquefaction susceptibility criteria for silts and clays, *J. Geotech. Geoenviro. Eng*., 132(11):1413–1426, https://doi.org/10.1061/(ASCE)1090-0241(2006)132:11(1413).

Boulanger R.W., Idriss I.M. (2007). Evaluation of cyclic softening in silts and clays, *J. Geotech. Geoenviro. Eng*., 133(6): 641–652, https://doi.org/10.1061/(ASCE)1090-0241(2007)133:6(641).

Boulanger R.W., Idriss I.M. (2014). CPT and SPT-based liquefaction triggering procedures*, Report No. UCD/CGM-14/01*, Center for Geotechnical Modeling, University of California, Davis, CA.

Boulanger R.W., Idriss I.M., Mejia L.H. (1995). Investigation and evaluation of liquefaction related ground displacements at Moss Landing during the 1989 Loma Prieta earthquake, *Report No. UCD/CGM-95/02*, Center for Geotechnical Modeling, University of California, Davis, 231 pgs.

Boulanger R.W, Khosravi M., Cox B.R., DeJong J.T. (2019). Liquefaction evaluation for an interbedded soil deposit: St. Teresa's School, Christchurch, New Zealand, *Proceedings*, *IACGE 2018: Geotechnical and Seismic Research and Practices for Sustainabilit*y, Chongqing, China, pp. 686–704.

Boulanger R.W., Mejia L.H., Idriss I.M. (1997). Liquefaction at Moss Landing during Loma Prieta earthquake, *J. Geotech. Geoenviro. En*g., 123(5):453–67, https://doi.org/10.1061/(ASCE)1090-0241(1997)123:5(453).

Bradley B.A. (2012). Strong ground motion characteristics observed in the 4 September 2010 Darfield, New Zealand earthquake, *Soil Dyn. Earthq. Eng*., 42:32–46, https://doi.org/10.1016/j.soildyn.2012.06.004.

Bradley B.A. (2013). A New Zealand-specific pseudo spectral acceleration ground-motion prediction equation for active shallow crustal earthquakes based on foreign models, *Bull. Seismol. Soc. Am.,* 103(3):1801–1822.

Bradley B.A. (2014). Site-specific and spatially-distributed ground motion intensity estimation in the 2010–2011 Christchurch earthquakes, *Soil Dyn. Earthq. Eng*., 48:35–47, https://doi.org/10.1016/j.soildyn.2014.01.025.

Bradley B.A. (2016). Strong ground motion characteristics observed in the 13 June 2011 Mw6.0 Christchurch, New Zealand earthquake, *Soil Dyn. Earthq. Eng*., 91:23–38, https://doi.org/10.1016/j.soildyn.2016.09.006.

Bradley B.A., Cubrinovski M. (2011). Near-source strong ground motions observed in the 22 February 2011 Christchurch earthquake, *Seismol. Res. Lett.,* 82(6):853–865, https://doi.org/10.1785/gssrl.82.6.853.

Bradley B.A., Razafindrakoto H., Maurer B.W., Motha J., Tarbali L., Lee, R. (2018). Simulation-based ground motion prediction of historical and future New Zealand earthquakes and consequent geohazard impacts, *Geotechnical Special Publication*, 291:29-42, https://doi.org/10.1061/9780784481462.004.

Bradley B.A., Savarimuthu S., Lagrava D., Huang J., Motha J., Polak V., Bae S. (2017). SeisFinder: A web application for extraction of data from computationally-intensive earthquake resilience calculations, Poster Presentation, *2017 SCEC Annual Meeting*. Palm Springs, CA.

Brandenberg S.J., Zimmaro P., Stewart J.P., Kwak D.Y., Franke K.W., Moss R.E., Kramer S.L. (2020). Next-generation liquefaction database. *Earthq. Spectra*, https://doi.org/10.1177/8755293020902477.

Bray J., Cubrinovski M., Zupan J., Taylor M. (2014). Liquefaction effects on buildings in the central business district of Christchurch, Earthq. Spectra 30(1):85–109, https://doi.org/10.1193/022113EQS043M.

Bray J.D., Macedo J. (2017). Simplified procedure for estimating liquefaction-induced building settlement, *Soil Dyn. Earthq. Eng*., 102:215–231, https://doi.org/10.1016/j.soildyn.2017.08.026.

Bray J.D., Sancio R.B. (2006). Assessment of the liquefaction susceptibility of fine-grained soils, *J. Geotech. Geoenviro. Eng.*, 132(9):1165–1177, https://doi.org/10.1061/(ASCE)1090-0241(2006)132:9(1165).

Brennan A.J., Madabhushi S.P. (2005). Liquefaction and drainage in stratified soil, *J. Geotech. Geoenviro. Eng.*, 131(7):876–885, https://doi.org/10.1061/(ASCE)1090-0241(2005)131:7(876).

Brown L.J. (1975). Water well data. Sheet 576/7-8, Belfast-Styx, *New Zealand Geological Survey, Report 72.*

Brown L.J., Beetham R.D., Paterson B.R., Weeber J.H. (1995). Geology of Christchurch, New Zealand, *Environ. Eng. Geosci*., 1(4):427–488, nttps://doi.org/10.2113/gseegeosci.I.4.427.

Brown L.J., Weeber J.H. (1992) Geology of the Christchurch urban area: Institute of Geological and Nuclear Sciences Geological Map 1, *Institute of Geological and Nuclear Sciences Limited, Lower Hutt, New Zealand, scale*, *1*(25,000), 1.

Brown L.J., Beetham R.D., Paterson B.R., Weeber J.H. (1995). Geology of Christchurch, New Zealand, *Environ. Eng. Geosci*., 1(4):427–488, nttps://doi.org/10.2113/gseegeosci.I.4.427.

Buck J.R., Daniel M.M, Singer A.C, (2002). *Computer Explorations in Signals and Systems Using MATLAB®,* 2nd Ed., Upper Saddle River, NJ: Prentice Hall.

Bullock Z., Karimi Z., Dashti S., Porter K., Liel A.B., Franke K.W., (2018). A physics-informed semi-empirical probabilistic model for the settlement of shallow-founded structures on liquefiable ground. *Géotechnique*, https://doi.org/10.1680/jgeot.17.P.174.

Byrne P.M., Park S.S., Beaty M., Sharp M.K., Gonzalez L., Abdoun T. (2004). Numerical modeling of liquefaction and comparison with centrifuge tests, *Can. Geotech. J.,* 41(2):193–211, https://doi.org/10.1139/t03-088.

CERA [2013]. *Purpose and Scope of the Canterbury Geotechnical Database*, Canterbury Earthquake Recovery Authority, Information Note, Revision D. Christchurch, New Zealand.

CESMD (2016). *U.S. Structural and Ground Response Data*, Center for Engineering Strong Motion Data, www.strongmotioncenter.org/.

Cetin K.O., Bilge H.T., Wu J, Kammerer A.M., Seed R.B., [2009]. Probabilistic model for the assessment of cyclically induced reconsolidation (volumetric) settlements, *J. Geotech. Geoenviro. Eng.*, 135(3):387–398, https://doi.org/10.1061/(ASCE)1090-0241(2009)135:3(387).

Cetin K.O., Seed R.B., Moss R.E.S., Der Kiureghian A.K., Tokimatsu K., Harder L.F., Kayen R.E. (2000). Field performance case histories for SPT-based evaluation of soil liquefaction triggering hazard, *Geotechnical Engineering Research Report No. UCB/GT-2000/09*, University of California, Berkeley, CA.

Chalmers G., McLennan N., Barsanti L. (2013). Lyttelton port of Christchurch seismic resilience from an owners' perspective, *Proceedings of Ports 2013: Success Through Diversification*, Seattle, WA, pp. 1405–1414.

Christensen S.A. (1995). *Liquefaction of Cohesionless Soils in the March 2, 1987 Edgecumbe Earthquake, Bay of Plenty, New Zealand, and other Earthquakes*, Master of Engineering Thesis, Department of Civil Engineering, University of Canterbury, Christchurch, New Zealand.

Cox B.R., Stolte A.C., Stokoe K.H., Wotherspoon L.M. (2018). A Direct-Push Crosshole (DPCH) test method for the in situ evaluation of high-resolution P-and S-wave velocities, *Geotech. Test. J.*, 42(5):1101–1132, https://doi.org/10.1520/GTJ20170382.

Cox B.R., Boulanger R.W., Tokimatsu K., Wood C., Abe A., Ashford S., Donahue J., Ishihara K., Kayen R., Katsumata K., Kishida T., Kokusho T., Mason B., Moss R., Stewart J., Tohyama K., Zekkos D., [2013]. Liquefaction at strong motion stations in Urayasu City during the 2011 Tohoku-Oki earthquake, *Earthq. Spectra,* 29(S1):S55–S80, https://doi.org/10.1193/1.4000110.

Cubrinovski M., Bray J.D., Taylor M., Giorgini S., Bradley B.A., Wotherspoon L., Zupan J. (2011). Soil liquefaction effects in the central business district during the February 2011 Christchurch earthquake, *Seismol. Res. Lett*., 82:893–904, https://doi.org/10.1785/gssrl.82.6.893.

Cubrinovski M., Ishihara K. (1998). State concept and modified elastoplasticity for sand modeling, *Soils Found.,* 38(4):213–225, https://doi.org/10.3208/sandf.38.4_213.

Cubrinovski M., Winkley A., Haskell J., Palermo A., Wotherspoon L., Robinson K., Bradley B., Brabhaharan P., Hughes M. (2014). Spreading-induced damage to short-span bridges in Christchurch, New Zealand, *Earthq. Spectra,* 30(1):57–83, https://doi.org/10.1193/030513EQS063M.

Cubrinovski M., Robinson K. (2016). Lateral spreading: Evidence and interpretation from the 2010–2011 Christchurch earthquakes, *Soil Dyn. Earthq. Eng*., 91:187–201, https://doi.org/10.1016/j.soildyn.2016.09.045.

Cubrinovski, M., Rhodes, A., Ntritsos, N., and van Ballegooy, S., (2019). System response of liquefiable deposits, *Soil Dyn. Earthq. Eng*., 124:212–229,

Darby K.M., Bronner J.D., Parra Bastidas A.M., Boulanger R.W., DeJong J.T. (2016). Effect of shaking history on the cone penetration resistance and cyclic strength of saturated sand, *Proceedings, Geotechnical and Structural Engineering Congress 2016*, Phoenix, AZ, pp. 1460–1471.

de Magistris F.S., Lanzano G., Forte G., Fabbrocino G. (2013). A database for PGA threshold in liquefaction occurrence, *Soil Dyn. Earthq. Eng.*, 54:17–19, https://doi.org/10.1016/j.soildyn.2013.07.011.

DeLong E.R., DeLong D.M., Clarke-Pearson, D.L. (1988). Comparing the areas under two or more correlated receiver operating characteristic curves: a nonparametric approach, *Biometrics,* 44:837–845, http://doi.org/10.1111/aas.12728.

Diaz-Rodriquez J.A. (1984). Liquefaction in the Mexicali Valley during the earthquake of June 9, 1980, *Proceedings, Eighth World Conference on Earthquake Engineering*, San Francisco, CA, pp. 223–230.

Diaz-Rodriquez J.A., Armijo-Palacio G. (1991). Liquefaction potential of fine cohesionless soils using the CPT, *Soils Found.,* 31(3):111-119, https://doi.org/10.3208/sandf1972.31.3_111.

Dobry R., Ladd R.S., Yokel F.Y., Chung R.M., Powell D. (1982). *Prediction of Pore Water Pressure Buildup and Liquefaction of Sands During Earthquakes by the Cyclic Strain Method*, National Bureau of Standards, Vol. 138, Gaithersburg, MD, https://doi.org/10.6028/NBS.BSS.138.

Dobry R., Thevanayagam S., El-Sekelly W., Abdoun T., Huang Q (2019). Large-scale modeling of preshaking effect on liquefaction resistance, shear wave velocity, and CPT tip resistance of clean sand, *J. Geotech. Geoenviro. Eng*., 145(10):04019065, https://doi.org/10.1061/(ASCE)GT.1943-5606.0002080.

Facciorusso J., Madiai C., Vannucchi G. (2015). CPT-based liquefaction case history from the 2012 Emilia Earthquake in Italy, *J. Geotech. Geoenviro. Eng*., 141(12):05015002, https://doi.org/10.1061/(ASCE)GT.1943-5606.0001349.

Farrar J.A. (1990). Study of in situ testing for evaluation of liquefaction resistance, *R-90-06*, Geotechnical Services Branch, Bureau of Reclamation, U.S. Department of the Interior, Denver CO.

Fawcett T. (2006). An introduction to ROC analysis, *Pattern Recogn. Lett.,* 27(8):861–874, https://doi.org/10.1016/j.patrec.2005.10.010.

FEMA (2013). *Earthquake Model HAZUS-MH 2.1 Technical Manual*, Federal Emergency Management Agency, Washington, D.C.

Fick S.E., Hijmans R.J. (2017). WorldClim 2: new 1-km spatial resolution climate surfaces for global land areas, *Inter. J. Climatol.*, 37(12):4302–4315, https://doi.org/10.1002/joc.5086.

Fiegel G.L., Kutter B.L. (1994). Liquefaction mechanism for layered soils, *J. Geotech. Geoenviro. Eng*., 120(4):737–755, https://doi.org/10.1061/(ASCE)0733-9410(1994)120:4(737).

Finno R.J., Gallant A.P., Sabatini P.J. (2016). Evaluating ground improvement after blast densification: performance at the Oakridge landfill, *J. Geotech. Geoenviro. Eng.,* 142(1):04015054, https://doi.org/10.1061/(ASCE)GT.1943-5606.0001365.

Geyin M., Baird A.J., Maurer B.W. (2020). Field assessment of liquefaction prediction models based on geotechnical vs. geospatial data, with lessons for each, *Earthq. Spectra,* 36(3):1386–1411, https://doi.org/10.1177/8755293019899951.

Geyin M., Maurer B.W. (2019). An analysis of liquefaction-induced free-field ground settlement using 1,000+ case-histories: observations vs. state-of-practice predictions, *Proceedings, Geocongress 2019*, C.L. Meehan, S. Kumar, M.A. Pando, and J.T. Coe, eds., *Geotechnical Special Publication*, 308:489–498.

Geyin M., Maurer B.W. (2020). *Horizon: CPT-Based Liquefaction Risk Assessment and Decision Software*, DesignSafe-CI, https://doi.org/10.17603/ds2-2fky-tm46.

Geyin M., Maurer B.W. (2021). Fragility functions for liquefaction induced ground failure, *J. Geotech. Geoenviro. Eng*., 146(12), https//doi.org/10.1061/(ASCE)GT.1943-5606.0002416.

Geyin M., Maurer B.W. (2019). An analysis of liquefaction-induced free-field ground settlement using 1,000+ case-histories: observations vs. state-of-practice predictions, *Geotechnical Special Publication,* 308:489–498, https://doi.org/10.1061/9780784482100.049.

Goda K., Hong H.P. (2008). Spatial correlation of peak ground motions and response spectra, *Bull. Seismol. Soc. Am.,* 98(1):354–365.

Green R.A., Ziotopoulou K. (2015). Overview of screening criteria for liquefaction triggering susceptibility. *Proceedings, 10th Pacific Conference on Earthquake Engineering*, Sydney, Australia, Paper No. 35. 2015.

Green R.A., Allen A., Wotherspoon L., Cubrinovski M., Bradley B., Bradshaw A., Cox B., Algie T. (2011). Performance of levees (stopbanks) during the 4 September M_w7.1 Darfield and 22 February 2011 M_w6.2 Christchurch, New Zealand, earthquakes, *Seismological Research Letters* 82(6): 939–949.

Green R.A., Bommer J.J., Rodriguez-Marek A., Maurer B.W., Stafford P.J., Edwards B., Kruiver P.P., De Lange G., Van Elk J. (2019). Addressing limitations in existing 'simplified' liquefaction triggering evaluation procedures: application to induced seismicity in the Groningen gas field, *Bulletin of Earthquake Engineering* 17(8):4539–4557, https://doi.org/10.1007/s10518-018-0489-3.

Green R.A., Cubrinovski M., Cox B., Wood C., Wotherspoon L., Bradley B., Maurer B. (2014). Select liquefaction case histories from the 2010–2011 Canterbury earthquake sequence, *Earthq. Spectra,* 30(1):131–153, https://doi.org/10.1193/030713EQS066M.

Green R.A., Maurer B.W., van Ballegooy S. (2018). The influence of the non-liquefied crust on the severity of surficial liquefaction manifestations: case history from the 2016 Valentine's Day earthquake in New Zealand. Geotechnical Earthquake Engineering and Soil Dynamics V: Liquefaction Triggering, Consequences, and Mitigation (S.J. Brandenberg and M.T. Manzari, eds.), *Geotechnical Special Publication*, 290:21–32, https://doi.org/10.1061/9780784481455.002.

Green R.A., Upadhyaya S., Wood C., Maurer B.W., Cox B.R., Wotherspoon L., Bradley B.A., Cubrinovski M. (2017). Relative efficacy of CPT- versus Vs – based simplified liquefaction evaluation procedures, *Proceedings,19th International Conference on Soil Mechanics and Geotechnical Engineering*, Seoul, Korea, pp. 1521–1524.

Green R.A., Bommer J.J., Rodriguez-Marek A., Maurer B.W., Stafford P.J., Edwards B., Kruiver P.P., De Lange G., Van Elk J. (2019). Addressing limitations in existing 'simplified' liquefaction triggering evaluation procedures: application to induced seismicity in the Groningen gas field, *Bull. Earthq. Eng.,* 17(8):4539–4557, https://doi.org/10.1007/s10518-018-0489-3.

Ha I.S., Olson S.M., Seo M.W., Kim M.M. (2011). Evaluation of reliquefaction resistance using shaking table tests, *Soil Dyn. Earthq. Eng*., 31(4):682–691, https://doi.org/10.1016/j.soildyn.2010.12.008.

Hayati H., Andrus R.D. (2009). Updated liquefaction resistance correction factors for aged sands, *J. Geotech. Geoenviro. Eng*., 135(11):1683–1692, https://doi.org/10.1061/(ASCE)GT.1943-5606.0000118.

Holzer T.L., Youd T.L. (2007). Liquefaction, ground oscillation, and soil deformation at the wildlife array, California, *Bull. Seismol. Soc. Am.,* 97(3):961–976.

Holzer T.L., Bennett M.J., Ponti D.J., Tinsley J.C., (1999). Liquefaction and soil failure during 1994 Northridge earthquake, *J. Geotech. Geoenviro. Eng*., 125(6):438–452, https://doi.org/10.1061/(ASCE)1090-0241(1999)125:6(438).

Hossain A.M., Andrus R.D., Camp W.M. III (2013). Correcting liquefaction resistance of unsaturated soil using wave velocity, *J. Geotech. Geoenviro. Eng*., 139(2):277–287, https://doi.org/10.1061/(ASCE)GT.1943-5606.0000770.

Idriss I.M., Boulanger R.W. (2008). *Soil Liquefaction during Earthquakes*, Earthquake Engineering Research Institute, Oakland, CA, 261 pgs.

Ishihara K. (1985). Stability of natural deposits during earthquakes, *Proceedings*, *11th International Conference on Soil Mechanics and Foundation Engineering*, San Francisco, CA, 1:321–376.

Ishihara K., Koga Y. (1981). Case studies of liquefaction in the 1964 Niigata earthquake, *Soils Found.,* 21(3):35–52, https://doi.org/10.3208/sandf1972.21.3_35.

Ishihara K., Tsukamoto Y. (2004). Cyclic strength of imperfectly saturated sands and analysis of liquefaction, *Proceedings, Japan Academy, Series B*, 80(8):372–391, https://doi.org/10.2183/pjab.80.372.

Iwasaki T., Tatsuoka F., Tokida K., Yasuda S. (1978). A practical method for assessing soil liquefaction potential based on case studies at various sites in Japan, *Proceedings*, *2nd International Conference on Microzonation*, San Francisco, CA.

Jeffries M.G., Davies M.P. (1993). Use of CPTu to estimate equivalent SPT N_{60}, *Geotech. Test. J.,* 16(4):458–468, https://doi.org/10.1520/GTJ10286J.

Johnson R.A., Wichern D.W. (2007). *Applied Multivariate Statistical Analysis,* Pearson Prentice Hall, Upper Saddle River, NJ.

Juang C.H., Yang S.H., Yuan H., Fang S.Y., (2005). Liquefaction in the Chi-Chi earthquake-effect of fines and capping non-liquefiable layers, *Soils Found.,* 45(6):89–101, https://doi.org/10.3208/sandf.45.89.

Kayen R.E., Mitchell J.K., Seed R.B., Nishio S. (1998). Soil liquefaction in the east bay during the earthquake*, The Loma Prieta, California, Earthquake of October 17, 1989 – Liquefaction*. Thomas L. Holzer, ed., United States Geological Survey, *USGS Professional Paper 1551-B*, pp. B61–B86, Menlo Park, CA.

Kayen R.E., Moss R.E.S., Thompson E.M., Seed R.B., Cetin O.K., Der Kiureghian A., Tanaka Y., Tokimatsu T. (2013). Shear wave velocity-based probabilistic and deterministic assessment of seismic soil liquefaction potential, *J. Geotech. Geoenviro. Eng*., 139(3):407–419, https://doi.org/10.1061/(ASCE)GT.1943-5606.0000743.

Kramer S.L., Sideras S.S., Greenfield M.W. (2016). The timing of liquefaction and its utility in liquefaction hazard evaluation, *Soil Dyn. Earthq. Eng*., 91:133–146, https://doi.org/10.1016/j.soildyn.2016.07.025.

Kramer S.L. (2008). Evaluation of liquefaction hazards in Washington State*, Report No. WA-RD 668.1*, Washington State Transportation Center, Seattle, WA.

Kulhawy F.H., Mayne P.W. (1990). Manual on estimating soil properties for foundation design, *Final Report 1493-6, EL-6800*, Electric Power Research Institute, Palo Alto, Calif

Kwasinski A., Eidinger J., Tang A., Tudo-Bornarel C. (2014). Performance of electric power systems in the 2010–2011 Christchurch, New Zealand, earthquake sequence, *Earthq. Spectra,* 30(1):205–230, https://doi.org/10.1193/022813EQS056M.

Lee D.H., Ku C.S., Juang C.H. [2000]. Preliminary investigation of soil liquefaction in the 1999 Chi-Chi, Taiwan, earthquake, *Proceedings, International Workshop on Annual Commemoration of Chi-Chi Earthquake, Vol. III—Geotechnical Aspect*, C.H. Loh and W.I. Liao, eds., National Center for Research on Earthquake Engineering, Taipei, Taiwan, pp. 140–151.

Lees J., Ballagh R.H., Orense R.P., van Ballegooy S. (2015b). CPT-based analysis of liquefaction and re-liquefaction following the Canterbury earthquake sequence, *Soil Dyn. Earthq. Eng.,* 79:304–314, https://doi.org/10.1016/j.soildyn.2015.02.004.

Lees J., van Ballegooy S., Wentz F.J. (2015a). Liquefaction susceptibility and fines content correlations of the Christchurch soils, *Proceedings, 6th International Conference on Earthquake Geotechnical Engineering*, Christchurch, New Zealand, Paper No. 491.

Lehner B., Verdin K., Jarvis A. (2006). *HydroSHEDS Technical Documentation*, U.S. World Wildlife Fund, Washington, D.C

Leon E., Gassman S.L. Talwani P. (2006). Accounting for soil aging when assessing liquefaction potential, *J. Geotech. Geoenviro. Eng*., 132(3):363–377, https://doi.org/10.1061/(ASCE)1090-0241(2006)132:3(363).

Li D.K., Juang C.H., Andrus R.D., Camp W.M. (2007). Index properties-based criteria for liquefaction susceptibility of clayey soils: a critical assessment*, J. Geotech. Geoenviro. Eng.,* 133(1):110–115, https://doi.org/10.1061/(ASCE)1090-0241(2007)133:1(110).

Lunne T., Robertson P.K., Powell J.M. (1997). *Cone Penetration Testing in Geotechnical Practice*. Blackie Academic and Professional, London, U.K.

Maurer B.W., Green R.A., Cubrinovski M., Bradley B.A. (2014). Evaluation of the liquefaction potential index for assessing liquefaction hazard in Christchurch, New Zealand, *J. Geotech. Geoenviro. Eng.,* 140(7):04014032, https://doi.org/10.1061/(ASCE)GT.1943-5606.0001117.

Maurer B.W., Green R.A., Taylor O.D.S. (2015a). Moving towards an improved index for assessing liquefaction hazard: lessons from historical data, *Soils Found.,* 55(4):778–787, https://doi.org/10.1016/j.sandf.2015.06.010.

Maurer B.W., Green R.A., Cubrinovski M. Bradley B.A. (2015b). Fines-content effects on liquefaction hazard evaluation for infrastructure during the 2010-2011 Canterbury, New Zealand earthquake sequence, *Soil Dyn. Earthq. Eng.*, 76:58–68, https://doi.org/10.1016/j.soildyn.2014.10.028.

Maurer B.W., Green R.A., Cubrinovski M., Bradley B.A. (2015c). Assessment of CPT-based methods for liquefaction evaluation in a liquefaction potential index framework, *Géotechnique*, 65(5):328–336, https://doi.org/10.1680/geot.SIP.15.P.007.

Maurer B.W., Green R.A., Cubrinovski M., Bradley B.A. (2015d). Calibrating the liquefaction severity number (LSN) for varying misprediction economies: a case study in Christchurch, New Zealand, *Proceedings, 6th International Conference on Earthquake Geotechnical Engineering*, Christchurch, NZ., Paper No. 491.

Maurer B.W., Green R.A., van Ballegooy S., Wotherspoon L. (2019). Development of region-specific soil behavior type index correlations for evaluating liquefaction hazard in Christchurch, New Zealand, *Soil Dyn. Earthq. Eng*., 117:96–105, https://doi.org/10.1016/j.soildyn.2018.04.059.

Maurer B.W., van Ballegooy, S., Bradley B.A. (2017). Fragility functions for performance-based damage assessment of soil liquefaction, *Proceedings*, *3rd International Conference on Performance-Based Design in Earthquake Geotechnical Engineering,* Vancouver, Canada.

Mayne P.W., Peuchen J., Bouwmeester D. (2010). Soil unit weight estimation from CPTs, *Proceedings*, *2nd International Symposium on Cone Penetration Testing*, Huntington Beach, CA, 8 pgs.

McLaughlin K. (2017). *Investigation of False-Positive Liquefaction Case History Sites in Christchurch*, New Zealand, M.S. Thesis. The University of Texas at Austin, Austin, TX.

Mesri G., Feng T., Benak J.M. (1990). Postdensification penetration resistance of clean sands, *J. Geotech. Eng.*, 116(7): 1095–1115, https://doi.org/10.1061/(ASCE)0733-9410(1990)116:7(1095).

Mitchell J.K., Lodge A.L., Coutinho R.Q., Kayen R.E., Seed R.B., Nishio S., Stokoe K.H., II (1994). In situ test results from four Loma Prieta earthquake liquefaction sites: SPT, CPT, DMT and shear wave velocity, *Report No. UCB/EERC-94/04*, Earthquake Engineering Research Center, University of California, Berkeley, CA.

Moss R.E.S., Seed R.B., Kayen R.E., Stewart J.P., Der Kiureghian A., Cetin KO (2006). CPT-based probabilistic and deterministic assessment of in situ seismic soil liquefaction potential, *J. Geotech. Geoenviro. Eng*., 132(8): 1032–1051, https://doi.org/10.1061/(ASCE)1090-0241(2006)132:8(1032).

Moss R.E.S., Collins B.D., Whang D.H. (2005). Retesting of liquefaction/nonliquefaction case histories in the Imperial Valley, *Earthq. Spectra*, 21(1):179–196, https://doi.org/10.1193/1.1852562.

Moss R.E.S., Kayen R.E., Tong L.-Y., Liu S.-Y., Cai G.-J., Wu, J., (2009). Re-investigation of liquefaction and nonliquefaction case histories from the 1976 Tangshan earthquake, *PEER Report No. 2009/102*, Pacific Earthquake Engineering Research Center, University of California, Berkeley, CA.

Moss R.E.S., Kayen R.E., Tong L.-Y., Liu S.-Y., Cai G.-J., Wu, J. (2011). Retesting of liquefaction and nonliquefaction case histories from the 1976 Tangshan earthquake, *J. Geotech Geoenviro. Eng*., 137(4)334–343, https://doi.org/10.1061/(ASCE)GT.1943-5606.0000406.

Moss R.E.S., Seed R.B., Kayen R.E., Stewart J.P., Youd T.L., Tokimatsu, K. (2003). Field case histories for CPT-based in situ liquefaction potential evaluation, *Geoengineering Research Report UCB/GE-2003/04*, University of California, Berkeley, CA.

Nakata T., Shimazaki K. (1997). Geo-slicer, a newly invented soil sampler, for high-resolution active fault studies, *J. Geogr.*, 106(1):59–69 (in Japanese), https://doi.org/ 10.5026/jgeography.106.59.

NRC (2016). *State of the Art and Practice in the Assessment of Earthquake-Induced Soil Liquefaction and its Consequences*, National Research Council, Committee on Earthquake Induced Soil Liquefaction Assessment (Edward Kavazanjian, Jr., Chair, Jose E. Andrade, Kandian "Arul" Arulmoli, Brian F. Atwater, John T. Christian, Russell A. Green, Steven L. Kramer, Lelio Mejia, James K. Mitchell, Ellen Rathje, James R. Rice, and Yumie Wang), The National Academies Press, Washington, DC.

Ntritsos N., Cubrinovski M. (2010). A CPT based effective stress analysis procedure for liquefaction assessment, *Soil Dyn. Earthq. Eng*., 131:106063.

NZGD (2020). New Zealand Geotechnical Database. *New Zealand Earthquake Commission.* <https://www.nzgd.org.nz/>, (Accessed Jan 01, 2020).

O'Rourke T, Jeon S.S., Toprak S., Cubrinovski M., Hughes M., van Ballegooy S. Bouziou D. (2014). Earthquake response of underground pipeline networks in Christchurch, NZ, Earthq. Spectra 30(1):183–204, https://doi.org/10.1193/030413EQS062M.

Özener P., Özaydin K., Berilgen, M. (2008). Numerical and physical modeling of liquefaction mechanisms in layered sands, *Proceedings*, *Geotech. Earthq. Eng. Soil Dyn.* IV, Sacramento, CA, pp. 1–12.

Ozutsumi O., Sawada S., Iai S., Takeshima Y., Sugiyama W., Shimazu T. (2002). Effective stress analyses of liquefaction-induced deformation in river dikes, *Soil Dyn. Earthq. Eng*., 22(9):1075–1082, https://doi.org/10.1016/S0267-7261(02)00133-1.

Papathanassiou G., Mantovani A., Tarabusi G., Rapti D., Caputo R. (2015). Assessment of liquefaction potential for two liquefaction prone areas considering the May 20, 2012 Emilia (Italy) earthquake, *Eng. Geol.*, 189:1–16, https://doi.org/10.1016/j.enggeo.2015.02.002.

Pass D.G. (1994). Soil Characterization of the Deep Accelerometer site at Treasure Island, San Francisco, California, MS Thesis, University of New Hampshire, Durham, NH.

Pease J.W. (2010). Misclassification in CPT liquefaction evaluation, *Proceedings*, *2nd International Symposium on Cone Penetration Testing*. Huntington Beach, CA, Paper # 3–23.

PEER (2000a). Documenting incidents of ground failure resulting from the 1999 Kocaeli, Turkey Earthquake, Pacific Earthquake Engineering Research Center, University of California, Berkeley, CA, https://tinyurl.com/ujtpwrk.

PEER (2000b). Documentation of soil conditions at liquefaction sites from 1999 Chi-Chi, Taiwan, earthquake, Pacific Earthquake Engineering Research Center, University of California, Berkeley, CA, https://tinyurl.com/sbh9cpg.

Pinheiro J., Bates D.M., DebRoy S., Sarkar D., R Core Team. (2008). NLME: Linear and nonlinear mixed effects models, *R Corepackage*, Ver. 3.1, http://www.r-project.org (Mar. 26, 2014).

Polito C. (2001). Plasticity based liquefaction criteria, *Proceedings, 4th International Conference on Recent Advances in Geotechnical Earthquake Engineering and Soil Dynamics*, San Diego, CA, Paper No. 25.

Quigley M.C., Bastin S., Bradley B.A. (2013). Recurrent liquefaction in Christchurch, New Zealand, during the Canterbury earthquake sequence, *Geol*., 41:419–422, https://doi.org/10.1130/G33944.1

Quigley M.C., Hughes M.W., Bradley B.A., van Ballegooy S., Reid C., Morgenroth J., Horton T., Duffy B., Pettinga J. (2016). The 2010–2011 Canterbury earthquake sequence: Environmental effects, seismic triggering thresholds, geologic legacy, *Tectonophys*., 672-673:228–274, https://doi.org/10.1016/j.tecto.2016.01.044.

Raschke S.A., Hryciw R.D. (1997). Vision cone penetrometer for direct subsurface soil observation, *J. Geotech Geoenvrion. Eng*., 123(11):1074–1076, https://doi.org/10.1061/(ASCE)1090-0241(1997)123:11(1074).

Rashidian V., Gillins D.T. (2018). Modification of the liquefaction potential index to consider the topography in Christchurch, New Zealand., Eng. Geol., 232:68–81, https://doi.org/10.1016/j.enggeo.2017.11.010.

Robertson P.K. (2011). Automated detection of CPT transition zones, *Geotech. News*, June, pp. 35–38.

Robertson P.K., Cabal K.L. (2010). Estimating soil unit weight from CPT, *Proceedings*, *2nd International Symposium on Cone Penetration Testing*, Huntington Beach, CA, 8 pgs.

Robertson P.K., Wride C.E. (1998). Evaluating cyclic liquefaction potential using the cone penetration test, *Can. Geotech. J.*, 35(3):442–459, *https://doi.org/10.1139/t98-017.*

Saftner D.A., Green R.A., Hryciw R.D. (2015). Use of explosives to investigate liquefaction resistance of aged sand deposits, *Eng. Geol.*, 199:140–147, https://doi.org/10.1016/j.enggeo.2015.11.002.

Seed R.B., Cetin K.O., Moss R.E.S., Kammerer A.M., Wu J., Pestana J.M., Riemer M.F., Sancio R.B., Bray J.D., Kayen R.E., Faris A. (2003). Recent advances in soil liquefaction engineering: a unified and consistent framework, *Proceedings, 26th Annual ASCE Los Angeles Geotechnical Spring Seminar*, Long Beach, CA.

Seed H.B., Tokimatsu K., Harder L.F. Jr., Chung R. (1984). The influence of SPT procedures in soil liquefaction resistance evaluations, *Report No. UCB/EERC-84/15*, Earthquake Engineering Research Center, University of California, Berkeley, CA.

Seed H.B., Idriss I.M. (1971). Simplified procedure for evaluating soil liquefaction potential, *J. Soil Mech. Found. Div*., 97(9):1249–1273, *https://doi.org/10.1061/JSFEAQ.0001662.*

Seisfinder (2020). *A web application to enable the extraction of high-fidelity outputs from computationally intensive earthquake resilience calculations*. Accessed 1 August 2020 <https://quakecoresoft.canterbury.ac.nz/seisfinder/>

Servizio Geologico, [2016]. Database of the Emilia-Romagna region: geological, seismic, and soil survey, http://ambiente.regione.emiliaromagna.it/geologia/cartografia/webgis-banchedati/.

Shengcong F., Tatsuoka, F. [1984]. Soil liquefaction during Haicheng and Tangshan earthquake in China; a review, *Soils Found.* 24(4):11–29, https://doi.org/10.3208/sandf1972.24.4_11.

Shibata T., Teparaska W. [1988]. Evaluation of liquefaction potential of soils using cone penetration testing, *Soils Found.,* 28(2):49–60, https://doi.org/10.3208/sandf1972.28.2_49.

Sideras S.S. (2019). *Evolutionary Intensity Measures for More Accurate and Informative Evaluation of Liquefaction Triggering*, PhD Thesis, University of Washington, Seattle, WA.

Strahler A.N., (1952). Hypsometric (area-altitude) analysis of erosional topology, *Geol. Soc. Am. Bull.*, 63(11):1117–1142, https://doi.org/10.1130/0016-7606(1952)63[1117:HAAOET]2.0.CO;2

Suzuki Y., Tokimatsu K., Moss R.E.S., Seed R.B., Kayen R.E., [2003]. CPT-based liquefaction case histories from the 1995 Hyogoken-Nambu (Kobe) earthquake, Japan, *Geotechnical Engineering Research Report No. UCB/GE-2003/03*, University of California, Berkeley, CA.

Takada K, Atwater B.F., (2004). Evidence for liquefaction identified in peeled slices of Holocene deposits along the lower Columbia River, Washington, *Bull. Seismol. Soc., Am.,* 94(2):550–575, https://doi.org/10.1785/0120020152.

Tang A., Kwasinski A., Eidinger J., Foster C., Anderson P. [2014]. Telecommunication systems' performance: Christchurch earthquakes, *Earthq. Spectra,* 30(1):231–252, https://doi.org/10.1193/022213EQS046M.

Toprak S., Holzer T.L. [2003]. Liquefaction potential index: field assessment, *J. Geotech. Geoenviro. Eng*., 129(4):315–322, https://doi.org/10.1061/(ASCE)1090-0241(2003)129:4(315).

Townsend D., Lee J.M., Strong D.T., Jongens R., Smith Lyttle B., Ashraf S., Taylor M.L. [2016]. Mapping surface liquefaction caused by the September 2010 and February 2011 Canterbury earthquakes: A digital dataset, *N.Z. J. Geol. Geophys.*, 59(4):496–513, https://doi.org/10.1080/00288306.2016.1182929.#

Treadwell D.D. (1976). *The Influence of Gravity, Prestress, Compressibility, and Layering on Soil Resistance to Static Penetration*, PhD Thesis, University of California, Berkeley, CA.

Turner B., Brandenberg S.J., Stewart J.P. (2016). Case study of parallel bridges affected by liquefaction and lateral spreading, *J. Geotech. Geoenviro. Eng*., 142(7), https://doi.org/10.1061/(ASCE)GT.1943-5606.0001480.

Upadhyaya S., Green R.A., Rodriguez-Marek A., Maurer B.W., Wotherspoon L.M., Bradley B.A., Cubrinovski M. (2019). Influence of corrections to recorded peak ground accelerations due to liquefaction on predicted liquefaction response during the 2010–2011 Canterbury, New Zealand, earthquake sequence, *Proceedings, 13th Australia New Zealand Conference on Geomechanics*.

Upadhyaya S., Maurer B.W., Green R.A., Rodriguez-Marek A. (2020). Selecting the optimal factor of safety or probability of liquefaction triggering for engineering projects based on misprediction costs, *J. Geotech. Geoenviro. Eng*., 147(6), https://doi.org/10.1061/(ASCE)GT.1943-5606.0002511.

van Ballegooy S, Malan P, Lacrosse V, Jacka ME, Cubrinovski M, Bray JD, O'Rourke TD, Crawford S.A., Cowan H. (2014a). Assessment of liquefaction-induced land damage for residential Christchurch, *Earthq. Spectra*, 30(1):31–55, https://doi.org/10.1193/031813EQS070M.

van Ballegooy S., Cox S.C., Thurlow C., Rutter H.K., Reynolds T., Harrington G., Fraser J., Smith T. (2014b). Median water table elevation in Christchurch and surrounding area after the 4 September 2010 Darfield earthquake: Version 2, *GNS Science Report 2014/18*, *79 pgs.*

van Ballegooy S., Green R.A., Lees J., Wentz F., Maurer B.W. (2015a). Assessment of various CPT based liquefaction severity index frameworks relative to the Ishihara (1985). H1–H2 boundary curves, *Soils Dyn. Earthq. Eng.,* 79:347–364, https://doi.org/10.1016/j.soildyn.2015.08.015.

van der Linden T.I., De Lange D.A., Korff M. (2018). Cone penetration testing in thinly inter-layered soils. *Proceedings, Institution of Civil Engineers-Geotechnical Engineering*, 171(3):215–231.

Wald D.J., Allen T.I. (2007). Topographic slope as a proxy for seismic site conditions and amplification, *Bull. Seismol*. Soc. Am., 97(5):1379–1395, https://doi.org/10.1785/0120060267.

Wang S., Yang J., Onyejekwe S. [2013]. Effect of previous cyclic shearing on liquefaction resistance of Mississippi River Valley silt, *J. Mat.Civil Eng.*, 25(10):1415–1423, https://doi.org/10.1061/(ASCE)MT.1943-5533.0000698.

Whitman R.V. (1971). Resistance of soil to liquefaction and settlement, *Soils Found*., 11(4):59–68, https://doi.org/10.3208/sandf1960.11.4_59.

Worden C.B., Wald D.J. [2016]. ShakeMap: Technical Manual, User's Guide, and software guide, U.S. Geological Survey, usgs.github.io/shakemap. https://doi.org/10.5066/F7D21VPQ.

Wotherspoon L.M., Bradshaw A., Green R.A., Wood C., Palermo A., Cubrinovski M., Bradley B.A. (2011). Performance of bridges during the 2010 Darfield and 2011 Christchurch earthquakes, Seismol. Res. Lett., 82(6):950–964, https://doi.org/10.1785/gssrl.82.6.950.

Wotherspoon L.M., Orense R.P., Green R.A., Bradley B.A., Cox B.R., Wood C.M. [2015]. Assessment of liquefaction evaluation procedures and severity index frameworks at Christchurch strong motion stations, *Soil Dyn. Earthq. Eng.*, 79(Part B):335–346, https://doi.org/10.1016/j.soildyn.2015.03.022.

Yost K.M., Cox B.R., Wotherspoon L., Boulanger R.W., van Ballegooy S., Cubrinovski M. (2019). In Situ Investigation of False-Positive Liquefaction Sites in Christchurch, New Zealand: Palinurus Road Case History. *Geo-Congress 2019: Earthquake Engineering and Soil Dynamics*, pp. 436–451.

Yost K.M., Green R.A., Upadhyaya S., Maurer B.W., Yerro-Colom A., Martin E. (2020). Assessment of the efficacies of correction procedures for multiple thin layer effects on cone penetration tests, *Soil Dyn. Earthq. Eng*., 144, https://doi.org/10.1016/j.soildyn.2021.106677.

Youd T.L., Carter B.L. [2005]. Influence of soil softening and liquefaction on spectral acceleration, *J. Geotech. Geoenviron. Eng*., 131(7):811–825, https://doi.org/10.1061/(ASCE)1090-0241(2005)131:7(811).

Youd T.L., DeDen D.W., Bray J.D., Sancio R., Cetin K.O., Gerber T.M. (2009). Zero-displacement lateral spreads, 1999 Kocaeli, Turkey, earthquake, *J. Geotech. Geoenviron. Eng*., https://doi.org/0.1061/(ASCE)1090-0241(2009)135:1(46).

Youd T.L., Hoose S.N. (1977). Liquefaction susceptibility and geologic setting, *Proceedings, 6th World Conference on Earthquake Engineering,* 3:2189–2194, New Delhi, India.

Youd T.L., Idriss I.M. (2001). Liquefaction resistance of soils: summary report from the 1996 NCEER and 1998 NCEER/NSF workshops on evaluation of liquefaction resistance of soils. *J. Geotech. Geoenviron. Eng*., 127:817–833, https://doi.org/10.1061/(ASCE)1090-0241(2001)127:4(297).

Zhang G., Robertson P.K., Brachman R.W.I. (2002). Estimating liquefaction-induced ground settlements from CPT for level ground. *Can. Geotech. J.*, 39(5):1168–1180, https://doi.org/10.1139/t02-047.

Zhang G., Robertson P.K., Brachman R.W.I. (2004). Estimating liquefaction-induced lateral displacements using the standard penetration test or cone penetration test. *J. Geotech. Geoenviron. Eng*., 130(8):861–871, https://doi.org/10.1061/(ASCE)1090-0241(2004)130:8(861).

Zhu J., Baise L.G., Thompson E.M. (2017). An updated geospatial liquefaction model for global application, *Bull. Seismol. Soc. Am*., 107(3):1365–1385, https://doi.org/10.1785/0120160198.

Zhu J., Daley D., Baise L.G., Thompson E.M., Wald D.J., Knudsen K.L. [2015]. A geospatial liquefaction model for rapid response and loss estimation, Earthq. Spectra, 31(3):1813–1837, https://doi.org/10.1193/121912EQS353M.

Zimmaro P., Brandenberg S.J., Bozorgnia Y., Stewart J.P., Kwak D.Y., Cetin K.O., Can G., Ilgac M., Franke K.W., Moss R.E.S., Kramer K.L., Stamatakos J., Juckett M., Weaver T. (2019). Quality control for next-generation liquefaction case histories, *Proceedings, 7th Int. Conference on Earthquake Geotechnical Engineering (VII ICEGE)*, pp. 5905–5912, Rome, Italy.

Ziotopoulou K., Boulanger R.W. [2016]. Plasticity modeling of liquefaction effects under sloping ground and irregular cyclic loading conditions, Soil Dyn. Earthq. Eng., 84:269–283, https://doi.org/10.1016/j.soildyn.2016.02.013.

Zou K.H., (2007). Receiver operating characteristic (ROC) literature research. *On-line bibliography*, *http://www.spl.harvard.edu/archive/spl-pre2007/pages/ppl/zou/roc.html*.

APPENDIX A Global Case-History Data

Provided on the following pages is a table of relevant metadata for each global liquefaction case-history compiled and analyzed in this study (i.e., the “global dataset”). This information would be needed to replicate the results presented herein. Additional methodology and commentary pertaining to this data is provided in Part Two of the report.

Table A.1 Global liquefaction case-history metadata.

No.	CPT ID	Date	Event	Country	Mag (M_w)	PGA (g)	GWT (mbg)	Y/N	References
1	D - Kawagisho-cho	16-Jun-64	Niigata	Japan	7.6	0.162	1.1	Y	Ishihara and Koga [1981]; Farrar [1990]; Moss et al. [2003]
2	E - Showa Bridge (Left Bank)	16-Jun-64	Niigata	Japan	7.6	0.162	1.4	Y	Ishihara and Koga [1981]; Farrar [1990]; Moss et al. [2003]
3	F - Showa Bridge (Right Bank)	16-Jun-64	Niigata	Japan	7.6	0.162	1.7	N	Ishihara and Koga [1981]; Farrar [1990]; Moss et al. [2003]
4	Balboa Boulevard (BAL-10)	9-Feb-71	San Fernando	United States	6.6	0.45	7.2	N	Bennett et al., 1998; Toprak and Holzer [2003]
5	Balboa Boulevard (BAL-11)	9-Feb-71	San Fernando	United States	6.6	0.45	7.6	N	Bennett et al., 1998; Toprak and Holzer [2003]
6	17th Middle School	4-Feb-75	Haicheng	China	7	0.3	1	N	Arulandan et al. (1986); Shengcong and Tatsuoka [1984]
7	Paper Mill	4-Feb-75	Haicheng	China	7	0.3	1.52	Y	Arulandan et al. (1986); Shengcong and Tatsuoka [1984]
8	Tangshan (T1)	27-Jul-76	Tangshan	China	7.6	0.64	3.7	Y	Shibata and Teparaska [1988]; Moss et al. [2009: 2011]
9	Tangshan (T4)	27-Jul-76	Tangshan	China	7.6	0.64	1.1	N	Shibata and Teparaska [1988]; Moss et al. [2009: 2011]
10	Tangshan (T6)	27-Jul-76	Tangshan	China	7.6	0.64	1.5	Y	Shibata and Teparaska [1988]; Moss et al. [2009: 2011]
11	Tangshan (T7)	27-Jul-76	Tangshan	China	7.6	0.64	3	Y	Shibata and Teparaska [1988]; Moss et al. [2009: 2011]
12	Tangshan (T8)	27-Jul-76	Tangshan	China	7.6	0.64	2.2	Y	Shibata and Teparaska [1988]; Moss et al. [2009: 2011]
13	Tangshan (T9-2)	27-Jul-76	Tangshan	China	7.6	0.64	1.1	N	Shibata and Teparaska [1988]; Moss et al. [2009: 2011]
14	Tangshan (T10)	27-Jul-76	Tangshan	China	7.6	0.64	1.5	Y	Shibata and Teparaska [1988]; Moss et al. [2009: 2011]
15	Tangshan (T11)	27-Jul-76	Tangshan	China	7.6	0.61	0.9	Y	Shibata and Teparaska [1988]; Moss et al. [2009: 2011]
16	Tangshan (T13)	27-Jul-76	Tangshan	China	7.6	0.58	1.1	Y	Shibata and Teparaska [1988]; Moss et al. [2009: 2011]
17	Tangshan (T16)	27-Jul-76	Tangshan	China	7.6	0.26	3.5	N	Shibata and Teparaska [1988]; Moss et al. [2009: 2011]
18	Kornbloom (KOR4)	15-Oct-79	Imperial Valley	United States	6.53	0.13	2.7	N	Bennett et al. [1984]; Moss et al. [2003]
19	Kornbloom (KOR5)	15-Oct-79	Imperial Valley	United States	6.53	0.13	2.7	N	Bennett et al. [1984]; Moss et al. [2003]
20	McKim Ranch (MCK4)	15-Oct-79	Imperial Valley	United States	6.53	0.51	1.5	N	Bennett et al. [1984]; Seed et al. [1984]
21	McKim Ranch (MCK7)	15-Oct-79	Imperial Valley	United States	6.53	0.51	1.5	Y	Bennett et al. [1984]; Seed et al. [1984]
22	Radio Tower (Rad2)	15-Oct-79	Imperial Valley	United States	6.53	0.2	2.1	Y	Bennett et al. [1984]; Seed et al. [1984]
23	Radio Tower (Rad4)	15-Oct-79	Imperial Valley	United States	6.53	0.2	2.1	N	Bennett et al. [1984]; Seed et al. [1984]
24	River Park (RVP002)	15-Oct-79	Imperial Valley	United States	6.53	0.16	0.3	Y	Moss et al. [2005]
25	Delta Site 1	9-Jun-80	Victoria (Mexicali)	Mexico	6.33	0.19	2.3	N	Diaz-Rodriguez [1984]; Diaz-Rodriguez and Armijo-Palaio [1991]; Moss et al. [2003]
26	Delta Site 2	9-Jun-80	Victoria (Mexicali)	Mexico	6.33	0.19	2.2	Y	Diaz-Rodriguez [1984]; Diaz-Rodriguez and Armijo-Palaio [1991]; Moss et al. [2003]
27	Delta Site 3	9-Jun-80	Victoria (Mexicali)	Mexico	6.33	0.19	2	Y	Diaz-Rodriguez [1984]; Diaz-Rodriguez and Armijo-Palaio [1991]; Moss et al. [2003]

No.	CPT ID	Date	Event	Country	Mag (M_w)	PGA (g)	GWT (mbg)	Y/N	References
28	Delta Site 3'	9-Jun-80	Victoria (Mexicali)	Mexico	6.33	0.19	2.2	Y	Diaz-Rodriguez [1984]; Diaz-Rodriguez and Armijo-Palaio [1991]; Moss et al. [2003]
29	Delta Site 4	9-Jun-80	Victoria (Mexicali)	Mexico	6.33	0.19	2	Y	Diaz-Rodriguez [1984]; Diaz-Rodriguez and Armijo-Palaio [1991]; Moss et al. [2003]
30	Wildlife B (3Cgb)	26-Apr-81	Elmore Ranch	United States	6.22	0.133	1.2	N	Bennett et al. [1984]; Cetin et al. [2000]
31	Wildlife B (3Cgc)	26-Apr-81	Westmorland	United States	5.9	0.26	1.2	Y	Bennett et al. [1984]; Cetin et al. [2000]
32	Herber Road (HEB001)	26-Apr-81	Westmorland	United States	5.9	0.17	1.8	N	Moss et al. [2005]
33	Kornbloom (KOR4)	26-Apr-81	Westmoreland	United States	5.9	0.32	2.7	Y	Bennett et al. [1984]; Seed et al. [1984]
34	Kornbloom (KOR5)	26-Apr-81	Westmoreland	United States	5.9	0.32	2.7	Y	Bennett et al. [1984]; Seed et al. [1984]
35	McKim Ranch (MCK4)	26-Apr-81	Westmorland	United States	5.9	0.09	1.5	N	Bennett et al. [1984]; Seed et al. [1984]
36	McKim Ranch (MCK7)	26-Apr-81	Westmorland	United States	5.9	0.09	1.5	N	Bennett et al. [1984]; Seed et al. [1984]
37	Radio Tower (Rad2)	26-Apr-81	Elmore Ranch	United States	6.22	0.09	2.1	N	Bennett et al. [1984]
38	Radio Tower (Rad2)	26-Apr-81	Westmorland	United States	5.9	0.2	2.1	Y	Bennett et al. [1984]; Seed et al. [1984]
39	Radio Tower (Rad4)	26-Apr-81	Westmorland	United States	5.9	0.2	2.1	N	Bennett et al. [1984]; Seed et al. [1984]
40	River Park (RVP002)	26-Apr-81	Westmorland	United States	5.9	0.17	0.3	N	Moss et al. [2005]
41	Akita B	26-May-83	Nihonkai-Chubu	Japan	7.7	0.17	1	Y	Farrar [1990]
42	Akita C	26-May-83	Nihonkai-Chubu	Japan	7.7	0.17	2.4	N	Farrar [1990]
43	Whiskey Springs Site 1 (CPT-1a)	28-Oct-83	Borah Peak	United States	6.88	0.5	0.8	Y	Andrus and Youd (1987), Moss et al. [2003]
44	Whiskey Springs Site 2 (CPT-2)	28-Oct-83	Borah Peak	United States	6.88	0.5	2.4	Y	Andrus and Youd (1987), Moss et al. [2003]
45	Whiskey Springs Site 3 (CPT-3)	28-Oct-83	Borah Peak	United States	6.88	0.5	6.8	Y	Andrus and Youd (1987), Moss et al. [2003]
46	Awaroa Farm (AWA004)	2-Mar-87	Edgecumbe	New Zealand	6.6	0.37	1.1	Y	Christensen [1995]
47	Brady Farm (BDY001)	2-Mar-87	Edgecumbe	New Zealand	6.6	0.4	1.65	Y	Christensen [1995], Moss et al. [2003]
48	Brady Farm (BDY004)	2-Mar-87	Edgecumbe	New Zealand	6.6	0.4	1.53	N	Christensen [1995], Moss et al. [2003]
49	Edgecumbe Pipe Breaks (EPB001)	2-Mar-87	Edgecumbe	New Zealand	6.6	0.39	3.5	Y	Christensen [1995], Moss et al. [2003]
50	Gordon Farm (GDN001)	2-Mar-87	Edgecumbe	New Zealand	6.6	0.43	0.5	Y	Christensen [1995], Moss et al. [2003]
51	Gordon Farm (GDN002)	2-Mar-87	Edgecumbe	New Zealand	6.6	0.43	0.9	N	Christensen [1995], Moss et al. [2003]
52	Whakatane Hospital (HSP001)	2-Mar-87	Edgecumbe	New Zealand	6.6	0.26	4.4	N	Christensen [1995], Moss et al. [2003]
53	James Street Loop (JSL006)	2-Mar-87	Edgecumbe	New Zealand	6.6	0.28	2	Y	Christensen [1995], Moss et al. [2003]
54	Keir Farm (KER001)	2-Mar-87	Edgecumbe	New Zealand	6.6	0.31	2.5	Y	Christensen [1995], Moss et al. [2003]
55	Landing Road Bridge LRB007)	2-Mar-87	Edgecumbe	New Zealand	6.6	0.27	1.2	Y	Christensen [1995], Moss et al. [2003]

No.	CPT ID	Date	Event	Country	Mag (M_w)	PGA (g)	GWT (mbg)	Y/N	References
56	Morris Farm (MRS001)	2-Mar-87	Edgecumbe	New Zealand	6.6	0.42	1.6	Y	Christensen [1995], Moss et al. [2003]
57	Morris Farm (MRS002)	2-Mar-87	Edgecumbe	New Zealand	6.6	0.42	1.89	N	Christensen [1995]
58	Morris Farm (MRS003)	2-Mar-87	Edgecumbe	New Zealand	6.6	0.41	2.08	N	Christensen [1995], Moss et al. [2003]
59	Robinson Farm (RBN001)	2-Mar-87	Edgecumbe	New Zealand	6.6	0.44	0.8	Y	Christensen [1995], Moss et al. [2003]
60	Robinson Farm (RBN002)	2-Mar-87	Edgecumbe	New Zealand	6.6	0.44	0.7	N	Christensen [1995]
61	Robinson Farm (RBN003)	2-Mar-87	Edgecumbe	New Zealand	6.6	0.44	0.9	N	Christensen [1995]
62	Robinson Farm (RBN004)	2-Mar-87	Edgecumbe	New Zealand	6.6	0.44	0.61	Y	Christensen [1995], Moss et al. [2003]
63	Sewage Pumping Station (SPS001)	2-Mar-87	Edgecumbe	New Zealand	6.6	0.26	1.3	Y	Christensen [1995], Moss et al. [2003]
64	Whakatane Board Mill (WBM001)	2-Mar-87	Edgecumbe	New Zealand	6.6	0.27	1.44	N	Christensen [1995], Moss et al. [2003]
65	Whakatane Board Mill (WBM002)	2-Mar-87	Edgecumbe	New Zealand	6.6	0.27	1.44	N	Christensen [1995], Moss et al. [2003]
66	Whakatane Pony Club (WPC001)	2-Mar-87	Edgecumbe	New Zealand	6.6	0.27	2.35	Y	Christensen [1995], Moss et al. [2003]
67	Whakatane Pony Club (WPC002)	2-Mar-87	Edgecumbe	New Zealand	6.6	0.27	2.2	Y	Christensen [1995]
68	Whakatane Pony Club (WPC003)	2-Mar-87	Edgecumbe	New Zealand	6.6	0.27	2.2	N	Christensen [1995]
69	Wildlife B (3Cg)	24-Nov-87	Superstition Hills	United States	6.54	0.206	1.2	Y	Bennett et al. [1984]; Holzer and Youd (2007); Cetin et al. [2000]
70	Herber Road (HEB001)	24-Nov-87	Superstition Hills	United States	6.6	0.16	1.8	N	Moss et al. [2005]
71	Kornbloom (KOR4)	24-Nov-87	Superstition Hills	United States	6.54	0.174	2.7	N	Bennett et al. [1984]; Cetin et al. [2000]
72	Kornbloom (KOR5)	24-Nov-87	Superstition Hills	United States	6.54	0.174	2.7	N	Bennett et al. [1984]; Cetin et al. [2000]
73	McKim Ranch (MCK4)	24-Nov-87	Superstition Hills	United States	6.54	0.2	1.5	N	Bennett et al. [1984]; Toprak and Holzer [2003]
74	Radio Tower (Rad2)	24-Nov-87	Superstition Hills	United States	6.54	0.2	2.1	N	Bennett et al. [1984]; Cetin et al. [2000]
75	Radio Tower (Rad4)	24-Nov-87	Superstition Hills	United States	6.54	0.18	2.1	N	Bennett et al. [1984]; Cetin et al. [2000]
76	River Park (RVP002)	24-Nov-87	Superstition Hills	United States	6.6	0.19	0.3	N	Moss et al. [2005]
77	Alameda Bay Farm Island (Dike)	18-Oct-89	Loma Prieta	United States	6.93	0.24	5.5	N	Mitchell et al. [1994]
78	Model Airport (AIR-18)	18-Oct-89	Loma Prieta	United States	6.93	0.26	2.4	Y	Bennett and Tinsely [1995]; Toprak and Holzer [2003]
79	Model Airport (AIR-21)	18-Oct-89	Loma Prieta	United States	6.93	0.26	2.4	Y	Bennett and Tinsely [1995]; Toprak and Holzer [2003]
80	Marine Lab (C4)	18-Oct-89	Loma Prieta	United States	6.93	0.28	2.8	Y	Boulanger et al. [1995; 1997]
81	Miller Farm (CMF-3)	18-Oct-89	Loma Prieta	United States	6.93	0.36	4.9	Y	Bennett and Tinsely [1995]; Toprak and Holzer [2003]
82	Miller Farm (CMF-5)	18-Oct-89	Loma Prieta	United States	6.93	0.36	4.9	Y	Bennett and Tinsely [1995]; Toprak and Holzer [2003]
83	Miller Farm (CMF-8)	18-Oct-89	Loma Prieta	United States	6.93	0.36	4.9	Y	Bennett and Tinsely [1995]; Toprak and Holzer [2003]
84	Miller Farm (CMF-10)	18-Oct-89	Loma Prieta	United States	6.93	0.36	3	N	Bennett and Tinsely [1995]; Toprak and Holzer [2003]

No.	CPT ID	Date	Event	Country	Mag (M_w)	PGA (g)	GWT (mbg)	Y/N	References
85	MBARI 4 (CPT-1)	18-Oct-89	Loma Prieta	United States	6.93	0.28	1.9	N	Boulanger et al. [1995; 1997]
86	General Fish (CPT-6)	18-Oct-89	Loma Prieta	United States	6.93	0.28	1.7	N	Boulanger et al. [1995; 1997]
87	Farris Farm (FAR-58)	18-Oct-89	Loma Prieta	United States	6.93	0.36	4.8	Y	Bennett and Tinsely [1995]; Toprak and Holzer [2003]
88	Farris Farm (FAR-59)	18-Oct-89	Loma Prieta	United States	6.93	0.36	4.8	Y	Bennett and Tinsely [1995]; Toprak and Holzer [2003]
89	Farris Farm (FAR-61)	18-Oct-89	Loma Prieta	United States	6.93	0.36	4.2	Y	Bennett and Tinsely [1995]; Toprak and Holzer [2003]
90	Granite Construction (GRA-123)	18-Oct-89	Loma Prieta	United States	6.93	0.34	5	Y	Bennett and Tinsely [1995]; Toprak and Holzer [2003]
91	Alameda Bay Farm Island (HBI-P6))	18-Oct-89	Loma Prieta	United States	6.93	0.24	3	Y	Mitchell et al. [1994]
92	Jefferson Ranch (JRR-141)	18-Oct-89	Loma Prieta	United States	6.93	0.21	2.1	Y	Bennett and Tinsely [1995]; Toprak and Holzer [2003]
93	Jefferson Ranch (JRR-148)	18-Oct-89	Loma Prieta	United States	6.93	0.21	3	Y	Bennett and Tinsely [1995]; Toprak and Holzer [2003]
94	KETT (KET-74)	18-Oct-89	Loma Prieta	United States	6.93	0.47	1.5	Y	Bennett and Tinsely [1995]; Toprak and Holzer [2003]
95	Leonardini (LEN-37)	18-Oct-89	Loma Prieta	United States	6.93	0.22	2.5	N	Bennett and Tinsely [1995]; Toprak and Holzer [2003]
96	Leonardini (LEN-39)	18-Oct-89	Loma Prieta	United States	6.93	0.22	1.9	Y	Bennett and Tinsely [1995]; Toprak and Holzer [2003]
97	Leonardini (LEN-51)	18-Oct-89	Loma Prieta	United States	6.93	0.22	1.8	Y	Bennett and Tinsely [1995]; Toprak and Holzer [2003]
98	Leonardini (LEN-52a)	18-Oct-89	Loma Prieta	United States	6.93	0.22	2.7	N	Bennett and Tinsely [1995]; Toprak and Holzer [2003]
99	Leonardini (LEN-53)	18-Oct-89	Loma Prieta	United States	6.93	0.22	2.1	Y	Bennett and Tinsely [1995]; Toprak and Holzer [2003]
100	Martella (MAR-110)	18-Oct-89	Loma Prieta	United States	6.93	0.13	1.8	N	Bennett and Tinsely [1995]; Toprak and Holzer [2003]
101	Martella (MAR-111)	18-Oct-89	Loma Prieta	United States	6.93	0.13	1.7	N	Bennett and Tinsely [1995]; Toprak and Holzer [2003]
102	McGowan Farm (MCG-136)	18-Oct-89	Loma Prieta	United States	6.93	0.26	2.4	N	Bennett and Tinsely [1995]; Toprak and Holzer [2003]
103	McGowan Farm (MCG-138)	18-Oct-89	Loma Prieta	United States	6.93	0.26	1.8	N	Bennett and Tinsely [1995]; Toprak and Holzer [2003]
104	Woodward Marine (14-A)	18-Oct-89	Loma Prieta	United States	6.93	0.28	1.2	Y	Boulanger et al. [1995; 1997]
105	Woodward Marine (15-A)	18-Oct-89	Loma Prieta	United States	6.93	0.28	1.3	Y	Boulanger et al. [1995; 1997]
106	Marinovich (MRR-65)	18-Oct-89	Loma Prieta	United States	6.93	0.4	5.6	Y	Bennett and Tinsely [1995]; Toprak and Holzer [2003]
107	Marinovich (MRR-67)	18-Oct-89	Loma Prieta	United States	6.93	0.4	6.2	N	Bennett and Tinsely [1995]; Toprak and Holzer [2003]
108	Port of Oakland (POO7-2)	18-Oct-89	Loma Prieta	United States	6.93	0.28	3	Y	Mitchell et al. [1994]; Kayen et al. [1998]
109	Port of Oakland (POO7-3)	18-Oct-89	Loma Prieta	United States	6.93	0.28	3	N	Mitchell et al. [1994]; Kayen et al. [1998]
110	Pajaro Dunes (PD1-44)	18-Oct-89	Loma Prieta	United States	6.93	0.22	3.4	Y	Bennett and Tinsely [1995]; Toprak and Holzer [2003]
111	Port of Richmond (POR-2)	18-Oct-89	Loma Prieta	United States	6.93	0.18	2.4	Y	Mitchell et al. [1994]; Kayen et al. [1998]
112	Port of Richmond (POR-3)	18-Oct-89	Loma Prieta	United States	6.93	0.18	2.4	Y	Mitchell et al. [1994]; Kayen et al. [1998]
113	Port of Richmond (POR-4)	18-Oct-89	Loma Prieta	United States	6.93	0.18	2.4	Y	Mitchell et al. [1994]; Kayen et al. [1998]
114	Radovich (RAD-98)	18-Oct-89	Loma Prieta	United States	6.93	0.38	3.5	N	Bennett and Tinsely [1995]; Toprak and Holzer [2003]
115	Radovich (RAD-99)	18-Oct-89	Loma Prieta	United States	6.93	0.38	4.1	Y	Bennett and Tinsely [1995]; Toprak and Holzer [2003]

No.	CPT ID	Date	Event	Country	Mag (M_w)	PGA (g)	GWT (mbg)	Y/N	References
116	MBARI 3 (RC-6)	18-Oct-89	Loma Prieta	United States	6.93	0.28	2.6	N	Boulanger et al. [1995; 1997]
117	MBARI 3 (RC-7)	18-Oct-89	Loma Prieta	United States	6.93	0.28	3.7	N	Boulanger et al. [1995; 1997]
118	Sea Mist (SEA-31)	18-Oct-89	Loma Prieta	United States	6.93	0.22	0.8	Y	Bennett and Tinsely [1995]; Toprak and Holzer [2003]
119	SFO Bay Bridge (SFOBB-1)	18-Oct-89	Loma Prieta	United States	6.93	0.28	3	Y	Mitchell et al. [1994]; Kayen et al. [1998]
120	SFO Bay Bridge (SFOBB-2)	18-Oct-89	Loma Prieta	United States	6.93	0.28	3	Y	Mitchell et al. [1994]; Kayen et al. [1998]
121	Silliman (SIL-68)	18-Oct-89	Loma Prieta	United States	6.93	0.38	3.5	Y	Bennett and Tinsely [1995]; Toprak and Holzer [2003]
122	Southern Pacific Bridge (SPR-48)	18-Oct-89	Loma Prieta	United States	6.93	0.33	5.3	Y	Bennett and Tinsely [1995]; Toprak and Holzer [2003]
123	Salinas River Bridge (SRB-116)	18-Oct-89	Loma Prieta	United States	6.93	0.12	6.4	N	Bennett and Tinsely [1995]; Moss et al. (2006)
124	Salinas River Bridge (SRB-117)	18-Oct-89	Loma Prieta	United States	6.93	0.12	6.4	N	Bennett and Tinsely [1995]; Moss et al. (2006)
125	Tanimura (TAN-103)	18-Oct-89	Loma Prieta	United States	6.93	0.13	5	Y	Bennett and Tinsely [1995]; Toprak and Holzer [2003]
126	Tanimura (TAN-105)	18-Oct-89	Loma Prieta	United States	6.93	0.13	4.2	N	Bennett and Tinsely [1995]; Toprak and Holzer [2003]
127	Treasure Island Fire Station (CPTU1)	18-Oct-89	Loma Prieta	United States	6.93	0.16	1.5	N	Pass [1994], Youd and Carter [2005]
128	Marine Lab (UC-1)	18-Oct-89	Loma Prieta	United States	6.93	0.28	2.4	Y	Boulanger et al. [1995; 1997]
129	Sandhold Road (UC-2)	18-Oct-89	Loma Prieta	United States	6.93	0.28	1.7	N	Boulanger et al. [1995; 1997]
130	Sandhold Road (UC-3)	18-Oct-89	Loma Prieta	United States	6.93	0.28	1.7	N	Boulanger et al. [1995; 1997]
131	Sandhold Road (UC-6)	18-Oct-89	Loma Prieta	United States	6.93	0.28	1.7	N	Boulanger et al. [1995; 1997]
132	Marine Lab (UC-7)	18-Oct-89	Loma Prieta	United States	6.93	0.28	2.4	Y	Boulanger et al. [1995; 1997]
133	Woodward Marine (UC-8)	18-Oct-89	Loma Prieta	United States	6.93	0.28	1.3	Y	Boulanger et al. [1995; 1997]
134	Woodward Marine (UC-9)	18-Oct-89	Loma Prieta	United States	6.93	0.28	1.2	Y	Boulanger et al. [1995; 1997]
135	Woodward Marine (UC-10)	18-Oct-89	Loma Prieta	United States	6.93	0.28	1	Y	Boulanger et al. [1995; 1997]
136	Woodward Marine (UC-11)	18-Oct-89	Loma Prieta	United States	6.93	0.28	1	Y	Boulanger et al. [1995; 1997]
137	Harbor Office (UC-12)	18-Oct-89	Loma Prieta	United States	6.93	0.28	1.9	Y	Boulanger et al. [1995; 1997]
138	Harbor Office (UC-13)	18-Oct-89	Loma Prieta	United States	6.93	0.28	1.9	Y	Boulanger et al. [1995; 1997]
139	State Beach Kiosk (UC-14)	18-Oct-89	Loma Prieta	United States	6.93	0.28	1.8	Y	Boulanger et al. [1995; 1997]
140	State Beach Path (UC-16)	18-Oct-89	Loma Prieta	United States	6.93	0.28	2.5	Y	Boulanger et al. [1995; 1997]
141	State Beach (UC-18)	18-Oct-89	Loma Prieta	United States	6.93	0.28	3.4	N	Boulanger et al. [1995; 1997]
142	Harbor Office (UC-20)	18-Oct-89	Loma Prieta	United States	6.93	0.28	3	Y	Boulanger et al. [1995; 1997]
143	Harbor Office (UC-21)	18-Oct-89	Loma Prieta	United States	6.93	0.28	2.7	Y	Boulanger et al. [1995; 1997]
144	Balboa Boulevard (BAL-10)	17-Jan-94	Northridge	United States	6.69	0.84	7.2	Y	Bennett et al., 1998; Holzer et al. [1999]; Moss et al. [2003]
145	Balboa Boulevard (BAL-11)	17-Jan-94	Northridge	United States	6.69	0.84	7.6	Y	Bennett et al., 1998; Holzer et al. [1999]; Moss et al. [2003]

No.	CPT ID	Date	Event	Country	Mag (M_w)	PGA (g)	GWT (mbg)	Y/N	References
146	Rory Lane (M-27)	17-Jan-94	Northridge	United States	6.69	0.8	3.4	Y	Abdel-Haq and Hryciw [1998]
147	Dust Management Facility (DMC)	16-Jan-95	Hyogoken-Nambu	Japan	6.9	0.37	2	Y	Suzuki et al. [2003]
148	Fukuzumi Park (FUP-1)	16-Jan-95	Hyogoken-Nambu	Japan	6.9	0.65	3.1	N	Suzuki et al. [2003]
149	Hamakoshienn Housing Area (HAH-1)	16-Jan-95	Hyogoken-Nambu	Japan	6.9	0.5	2	Y	Suzuki et al. [2003]
150	Honjyo Central Park (HCP-1)	16-Jan-95	Hyogoken-Nambu	Japan	6.9	0.7	2.5	N	Suzuki et al. [2003]
151	Imazu Elementary School (IES-1)	16-Jan-95	Hyogoken-Nambu	Japan	6.9	0.6	1.4	Y	Suzuki et al. [2003]
152	Kobe Art Institute (KAI-1)	16-Jan-95	Hyogoken-Nambu	Japan	6.9	0.5	3	N	Suzuki et al. [2003]
153	Kobe Customs Maya Office A (KMO-A)	16-Jan-95	Hyogoken-Nambu	Japan	6.9	0.6	1.8	Y	Suzuki et al. [2003]
154	Kobe Customs Maya Office A (KMO-B)	16-Jan-95	Hyogoken-Nambu	Japan	6.9	0.6	1.8	Y	Suzuki et al. [2003]
155	Kobe Port Construction Office (KOP-2)	16-Jan-95	Hyogoken-Nambu	Japan	6.9	0.6	2.5	Y	Suzuki et al. [2003]
156	Kobe Pump Station (KPS-1)	16-Jan-95	Hyogoken-Nambu	Japan	6.9	0.45	2.6	Y	Suzuki et al. [2003]
157	Mikuska Park (MIP-1)	16-Jan-95	Hyogoken-Nambu	Japan	6.9	0.65	2	Y	Suzuki et al. [2003]
158	Nagashi Park (NAP-1)	16-Jan-95	Hyogoken-Nambu	Japan	6.9	0.65	1	N	Suzuki et al. [2003]
159	Nisseki Kobe Oil Tank A (NKO-2)	16-Jan-95	Hyogoken-Nambu	Japan	6.9	0.6	2.4	Y	Suzuki et al. [2003]
160	Nisseki Kobe Oil Tank B (NKO-3)	16-Jan-95	Hyogoken-Nambu	Japan	6.9	0.6	2.4	Y	Suzuki et al. [2003]
161	New Port No. 6 Pier (NPP-1)	16-Jan-95	Hyogoken-Nambu	Japan	6.9	0.6	2.5	Y	Suzuki et al. [2003]
162	New Wharf Construction Offices (NWC-1)	16-Jan-95	Hyogoken-Nambu	Japan	6.9	0.45	2.6	Y	Suzuki et al. [2003]
163	Sumiyoshi Elementary (SES-1)	16-Jan-95	Hyogoken-Nambu	Japan	6.9	0.6	1.9	N	Suzuki et al. [2003]
164	Shimonakajima Park (SHP-2)	16-Jan-95	Hyogoken-Nambu	Japan	6.9	0.65	2	N	Suzuki et al. [2003]
165	Shiporex Kogyo Osaka Factory (SKF-1)	16-Jan-95	Hyogoken-Nambu	Japan	6.9	0.4	1.5	Y	Suzuki et al. [2003]
166	Tokuyama Concrete Factory (TCF-1)	16-Jan-95	Hyogoken-Nambu	Japan	6.9	0.5	2	Y	Suzuki et al. [2003]
167	Yoshida Kogyo Factory (YKF-1)	16-Jan-95	Hyogoken-Nambu	Japan	6.9	0.5	3	N	Suzuki et al. [2003]
168	Adapazari Site C2 (CPT-C4)	17-Aug-99	Kocaeli	Turkey	7.51	0.4	0.4	Y	PEER [2000a]

No.	CPT ID	Date	Event	Country	Mag (M_w)	PGA (g)	GWT (mbg)	Y/N	References
169	Adapazari Site K (CPT-K1)	17-Aug-99	Kocaeli	Turkey	7.51	0.4	0.8	Y	PEER [2000a]
170	Adapazari Site B	17-Aug-99	Kocaeli	Turkey	7.51	0.4	3.3	Y	PEER [2000a]
171	Adapazari Site D (CPT-D1)	17-Aug-99	Kocaeli	Turkey	7.51	0.4	1.5	Y	PEER [2000a]
172	Degirmendere DN-1	17-Aug-99	Kocaeli	Turkey	7.51	0.4	1.7	Y	Youd et al. [2009]
173	Degirmendere DN-2	17-Aug-99	Kocaeli	Turkey	7.51	0.4	2.5	N	Youd et al. [2009]
174	Adapazari Site E (CPT-E1)	17-Aug-99	Kocaeli	Turkey	7.51	0.4	0.5	Y	PEER [2000a]
175	Adapazari Site F (CPT-F1)	17-Aug-99	Kocaeli	Turkey	7.51	0.4	0.5	Y	PEER [2000a]
176	Adapazari Site G (CPT-G1)	17-Aug-99	Kocaeli	Turkey	7.51	0.4	0.5	Y	PEER [2000a]
177	Adapazari Site H (CPT-H1)	17-Aug-99	Kocaeli	Turkey	7.51	0.4	1.7	Y	PEER [2000a]
178	Adapazari Site J (CPT-J2)	17-Aug-99	Kocaeli	Turkey	7.51	0.4	0.6	Y	PEER [2000a]
179	Adapazari Site L (CPT-L1)	17-Aug-99	Kocaeli	Turkey	7.51	0.4	1.72	Y	PEER [2000a]
180	Police Station PS-1	17-Aug-99	Kocaeli	Turkey	7.51	0.4	1	Y	PEER [2000a]
181	Soccer Field SF-5	17-Aug-99	Kocaeli	Turkey	7.51	0.37	1	Y	PEER [2000a]
182	Hotel Spanca SH-4	17-Aug-99	Kocaeli	Turkey	7.51	0.37	0.5	Y	PEER [2000a]
183	Yalova Harbor YH-3	17-Aug-99	Kocaeli	Turkey	7.51	0.37	1	Y	PEER [2000a]
184	Nantou Site C (CPT-1)	20-Sep-99	Chi-Chi	Taiwan	7.62	0.38	1	Y	PEER (2000b)
185	Nantou Site C2	20-Sep-99	Chi-Chi	Taiwan	7.62	0.38	5	Y	PEER (2000b)
186	Nantou Site C3	20-Sep-99	Chi-Chi	Taiwan	7.62	0.38	1.5	Y	PEER (2000b)
187	Nantou Site C7 (CPT-7)	20-Sep-99	Chi-Chi	Taiwan	7.62	0.38	1	Y	PEER (2000b)
188	Nantou Site C8 (CPT-8)	20-Sep-99	Chi-Chi	Taiwan	7.62	0.38	1	Y	PEER (2000b)
189	Nantou Site C13	20-Sep-99	Chi-Chi	Taiwan	7.62	0.38	2	N	PEER (2000b)
190	Nantou Site C16	20-Sep-99	Chi-Chi	Taiwan	7.62	0.38	5.3	N	PEER (2000b)
191	Nantou Site K1	20-Sep-99	Chi-Chi	Taiwan	7.62	0.38	2.5	Y	PEER (2000b)
192	Nantou Site K5	20-Sep-99	Chi-Chi	Taiwan	7.62	0.38	2.5	Y	PEER (2000b)
193	WuFeng Site C7 NCREE	20-Sep-99	Chi-Chi	Taiwan	7.62	0.6	3.2	Y	PEER (2000b)
194	WuFeng Site C8 NCREE	20-Sep-99	Chi-Chi	Taiwan	7.62	0.6	3.2	N	PEER (2000b)
195	WuFeng Site C10 NCREE	20-Sep-99	Chi-Chi	Taiwan	7.62	0.6	1.4	Y	PEER (2000b)
196	WuFeng Site C15 NCREE	20-Sep-99	Chi-Chi	Taiwan	7.62	0.6	2.5	Y	PEER (2000b)
197	WuFeng Site B (WBC-1)	20-Sep-99	Chi-Chi	Taiwan	7.62	0.6	1.1	Y	PEER (2000b)
198	WuFeng Site C (WCC-6)	20-Sep-99	Chi-Chi	Taiwan	7.62	0.6	1.2	Y	PEER (2000b)
199	WuFeng Site K5	20-Sep-99	Chi-Chi	Taiwan	7.62	0.6	1	Y	Lee et al. [2000]
200	Yanlin Site C2	20-Sep-99	Chi-Chi	Taiwan	7.62	0.25	0.56	Y	PEER (2000b)

No.	CPT ID	Date	Event	Country	Mag (M_w)	PGA (g)	GWT (mbg)	Y/N	References
201	Yanlin Site C4	20-Sep-99	Chi-Chi	Taiwan	7.62	0.25	0.7	Y	PEER (2000b)
202	Yanlin Site C5	20-Sep-99	Chi-Chi	Taiwan	7.62	0.25	2.4	N	PEER (2000b)
203	Yanlin Site C7	20-Sep-99	Chi-Chi	Taiwan	7.62	0.25	1.7	N	PEER (2000b)
204	Yanlin Site C8	20-Sep-99	Chi-Chi	Taiwan	7.62	0.25	1.3	N	PEER (2000b)
205	Yanlin Site C9	20-Sep-99	Chi-Chi	Taiwan	7.62	0.25	1.2	N	PEER (2000b)
206	Yanlin Site C10	20-Sep-99	Chi-Chi	Taiwan	7.62	0.25	1.9	N	PEER (2000b)
207	Yanlin Site C11	20-Sep-99	Chi-Chi	Taiwan	7.62	0.25	2.9	N	PEER (2000b)
208	Yanlin Site C13	20-Sep-99	Chi-Chi	Taiwan	7.62	0.25	1.1	N	PEER (2000b)
209	Yanlin Site C15	20-Sep-99	Chi-Chi	Taiwan	7.62	0.25	1.5	N	PEER (2000b)
210	Yanlin Site C16	20-Sep-99	Chi-Chi	Taiwan	7.62	0.25	2.5	N	PEER (2000b)
211	Yanlin Site C19	20-Sep-99	Chi-Chi	Taiwan	7.62	0.25	0.6	Y	PEER (2000b)
212	Yanlin Site C22	20-Sep-99	Chi-Chi	Taiwan	7.62	0.25	1.1	Y	PEER (2000b)
213	Yanlin Site C24	20-Sep-99	Chi-Chi	Taiwan	7.62	0.25	1.2	Y	PEER (2000b)
214	Yanlin Site C25	20-Sep-99	Chi-Chi	Taiwan	7.62	0.25	3.5	Y	PEER (2000b)
215	Yanlin Site C32	20-Sep-99	Chi-Chi	Taiwan	7.62	0.25	0.7	Y	PEER (2000b)
216	Yanlin Site 44	20-Sep-99	Chi-Chi	Taiwan	7.62	0.25	1.4	N	PEER (2000b)
217	Site I (CPT-2)	8-Jun-08	Achaia-Ilia	Greece	6.4	0.18	0.4	Y	Batilas et al. [2014]
218	Site II (CPT-5)	8-Jun-08	Achaia-Ilia	Greece	6.4	0.18	0.4	N	Batilas et al. [2014]
219	San Felipito Bridges (CPT-1)	4-Apr-10	El Mayor-Cucapah	Mexico	7.2	0.265	2	Y	Turner et al. [2016]
220	Hinode Minami Elementary School	11-Mar-11	Tohoku	Japan	9	0.17	1.1	N	Cox et al. [2013], Boulanger and Idriss [2014]
221	Hosoyama Nekki	11-Mar-11	Tohoku	Japan	9	0.18	2.5	N	Cox et al. [2013], Boulanger and Idriss [2014]
222	Takasu Chuou Park	11-Mar-11	Tohoku	Japan	9	0.21	1.1	Y	Cox et al. [2013], Boulanger and Idriss [2014]
223	Takasu Kaihin Park	11-Mar-11	Tohoku	Japan	9	0.22	1.3	Y	Cox et al. [2013], Boulanger and Idriss [2014]
224	Akemi Elementary School	11-Mar-11	Tohoku	Japan	9	0.169	1.2	N	Cox et al. [2013], Boulanger and Idriss [2014]
225	Hinode Elementary School	11-Mar-11	Tohoku	Japan	9	0.199	1.2	Y	Cox et al. [2013], Boulanger and Idriss [2014]
226	Irifune Nursery School	11-Mar-11	Tohoku	Japan	9	0.256	1.6	Y	Cox et al. [2013], Boulanger and Idriss [2014]
227	184050U015	20-May-12	Emilia	Italy	6.1	0.22	4.2	N	Papathanassiou et al. [2015]; Servizio Geologico [2016]
228	184050U016	20-May-12	Emilia	Italy	6.1	0.22	4.2	N	Papathanassiou et al. [2015]; Servizio Geologico [2016]
229	184050U017	20-May-12	Emilia	Italy	6.1	0.22	2.65	N	Papathanassiou et al. [2015]; Servizio Geologico [2016]
230	184050U018	20-May-12	Emilia	Italy	6.1	0.22	3.45	N	Papathanassiou et al. [2015]; Servizio Geologico [2016]
231	184060U001	20-May-12	Emilia	Italy	6.1	0.31	3.8	N	Papathanassiou et al. [2015]; Servizio Geologico [2016]

No.	CPT ID	Date	Event	Country	Mag (M_w)	PGA (g)	GWT (mbg)	Y/N	References
232	184090U047	20-May-12	Emilia	Italy	6.1	0.27	4.2	N	Papathanassiou et al. [2015]; Servizio Geologico [2016]
233	184090U048	20-May-12	Emilia	Italy	6.1	0.27	3.7	N	Papathanassiou et al. [2015]; Servizio Geologico [2016]
234	184090U049	20-May-12	Emilia	Italy	6.1	0.27	3.25	N	Papathanassiou et al. [2015]; Servizio Geologico [2016]
235	184090U050	20-May-12	Emilia	Italy	6.1	0.27	3.2	N	Papathanassiou et al. [2015]; Servizio Geologico [2016]
236	184090U051	20-May-12	Emilia	Italy	6.1	0.25	2.5	N	Papathanassiou et al. [2015]; Servizio Geologico [2016]
237	184090U052	20-May-12	Emilia	Italy	6.1	0.25	2.5	N	Papathanassiou et al. [2015]; Servizio Geologico [2016]
238	184090U053	20-May-12	Emilia	Italy	6.1	0.19	4.9	N	Papathanassiou et al. [2015]; Servizio Geologico [2016]
239	184090U054	20-May-12	Emilia	Italy	6.1	0.19	4.9	N	Papathanassiou et al. [2015]; Servizio Geologico [2016]
240	184090U055	20-May-12	Emilia	Italy	6.1	0.23	3.4	N	Papathanassiou et al. [2015]; Servizio Geologico [2016]
241	185130B501	20-May-12	Emilia	Italy	6.1	0.59	3	Y	Papathanassiou et al. [2015]; Servizio Geologico [2016]
242	185130B502	20-May-12	Emilia	Italy	6.1	0.6	3	Y	Papathanassiou et al. [2015]; Servizio Geologico [2016]
243	185130B503	20-May-12	Emilia	Italy	6.1	0.59	3	Y	Papathanassiou et al. [2015]; Servizio Geologico [2016]
244	185130B504	20-May-12	Emilia	Italy	6.1	0.59	3	Y	Papathanassiou et al. [2015]; Servizio Geologico [2016]
245	185130U006	20-May-12	Emilia	Italy	6.1	0.73	3	N	Papathanassiou et al. [2015]; Servizio Geologico [2016]
246	185130U022	20-May-12	Emilia	Italy	6.1	0.58	1.8	N	Papathanassiou et al. [2015]; Servizio Geologico [2016]
247	185130U505	20-May-12	Emilia	Italy	6.1	0.6	5	Y	Papathanassiou et al. [2015]; Servizio Geologico [2016]
248	185130U506	20-May-12	Emilia	Italy	6.1	0.6	4.84	Y	Papathanassiou et al. [2015]; Servizio Geologico [2016]
249	185130U507	20-May-12	Emilia	Italy	6.1	0.6	5.16	Y	Papathanassiou et al. [2015]; Servizio Geologico [2016]
250	185130U508	20-May-12	Emilia	Italy	6.1	0.59	4.22	Y	Papathanassiou et al. [2015]; Servizio Geologico [2016]
251	185130U509	20-May-12	Emilia	Italy	6.1	0.59	2.37	N	Papathanassiou et al. [2015]; Servizio Geologico [2016]
252	185130U510	20-May-12	Emilia	Italy	6.1	0.59	5.23	N	Papathanassiou et al. [2015]; Servizio Geologico [2016]
253	185130U511	20-May-12	Emilia	Italy	6.1	0.59	4.65	N	Papathanassiou et al. [2015]; Servizio Geologico [2016]
254	185130U512	20-May-12	Emilia	Italy	6.1	0.58	4.4	Y	Papathanassiou et al. [2015]; Servizio Geologico [2016]
255	185130U513	20-May-12	Emilia	Italy	6.1	0.58	4.18	Y	Papathanassiou et al. [2015]; Servizio Geologico [2016]
256	185130U514	20-May-12	Emilia	Italy	6.1	0.58	4.55	Y	Papathanassiou et al. [2015]; Servizio Geologico [2016]
257	185140B001	20-May-12	Emilia	Italy	6.1	0.54	2	N	Papathanassiou et al. [2015]; Servizio Geologico [2016]
258	185140U002	20-May-12	Emilia	Italy	6.1	0.53	2.3	N	Papathanassiou et al. [2015]; Servizio Geologico [2016]
259	185140U003	20-May-12	Emilia	Italy	6.1	0.54	3.6	N	Papathanassiou et al. [2015]; Servizio Geologico [2016]
260	185140U004	20-May-12	Emilia	Italy	6.1	0.54	3.3	N	Papathanassiou et al. [2015]; Servizio Geologico [2016]
261	185140U005	20-May-12	Emilia	Italy	6.1	0.56	4.9	N	Papathanassiou et al. [2015]; Servizio Geologico [2016]
262	203010U001	20-May-12	Emilia	Italy	6.1	0.65	4	Y	Papathanassiou et al. [2015]; Servizio Geologico [2016]
263	203010U002	20-May-12	Emilia	Italy	6.1	0.65	4.9	Y	Papathanassiou et al. [2015]; Servizio Geologico [2016]

No.	CPT ID	Date	Event	Country	Mag (M_w)	PGA (g)	GWT (mbg)	Y/N	References
264	203010U005	20-May-12	Emilia	Italy	6.1	0.66	2.4	Y	Papathanassiou et al. [2015]; Servizio Geologico [2016]
265	203010U006	20-May-12	Emilia	Italy	6.1	0.65	2.4	Y	Papathanassiou et al. [2015]; Servizio Geologico [2016]
266	203010U509	20-May-12	Emilia	Italy	6.1	0.72	1.9	N	Papathanassiou et al. [2015]; Servizio Geologico [2016]
267	203020U095	20-May-12	Emilia	Italy	6.1	0.48	4.5	Y	Papathanassiou et al. [2015]; Servizio Geologico [2016]
268	203020U096	20-May-12	Emilia	Italy	6.1	0.48	1.6	Y	Papathanassiou et al. [2015]; Servizio Geologico [2016]
269	203020U097	20-May-12	Emilia	Italy	6.1	0.5	2.05	N	Papathanassiou et al. [2015]; Servizio Geologico [2016]
270	203020U098	20-May-12	Emilia	Italy	6.1	0.5	1.9	N	Papathanassiou et al. [2015]; Servizio Geologico [2016]
271	203020U099	20-May-12	Emilia	Italy	6.1	0.51	1.8	N	Papathanassiou et al. [2015]; Servizio Geologico [2016]
272	CPTU1	20-May-12	Emilia	Italy	6.1	0.31	1.4	Y	Papathanassiou et al. [2015]; Servizio Geologico [2016]; Facciorusso et al. [2015]
273	Wildlife B (3Cgd)		Mexicali		7.2	0.094	1.2	N	Bennett et al. [1984]; Holzer and Youd (2007); NEES [2016]
274	Herber Road (HEB001)		Mexicali		7.2	0.23	1.8	N	Moss et al. [2005]; CESMD [2016]

APPENDIX B Fragility Functions

Provided on the following pages are 240 fragility functions for predicting the severity of foundation damage using the RGM3 and GGM2 geospatial models. These functions are for specific severities of damage, specific modes of damage, and for specific types of shallow-foundation system. Function coefficients (for implementing the functions in forward analyses) are provided in Tables B.1 and B.2. Additional details and discussion are provided within the text of this report.

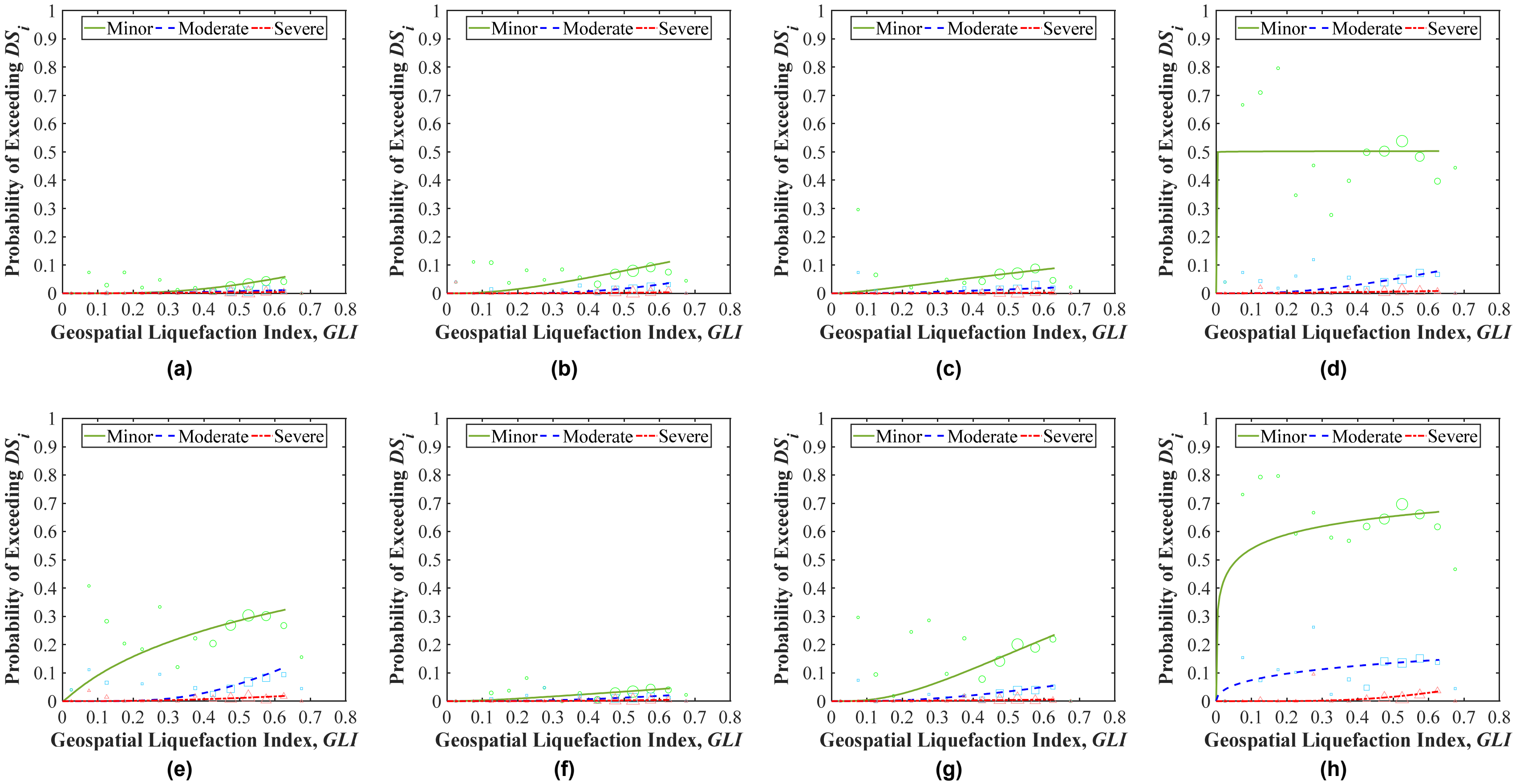

Figure B.1 **Fragility functions for predicting the probability of damage to timber floor on pile foundations using global geospatial model GGM2: (a) stretching failure; (b) hogging failure; (c) dishing failure; (d) twisting failure; (e) tilting failure; (f) discontinuous foundation failure; (g) global settlement failure; and (h) the failure mode with greatest observed severity.**

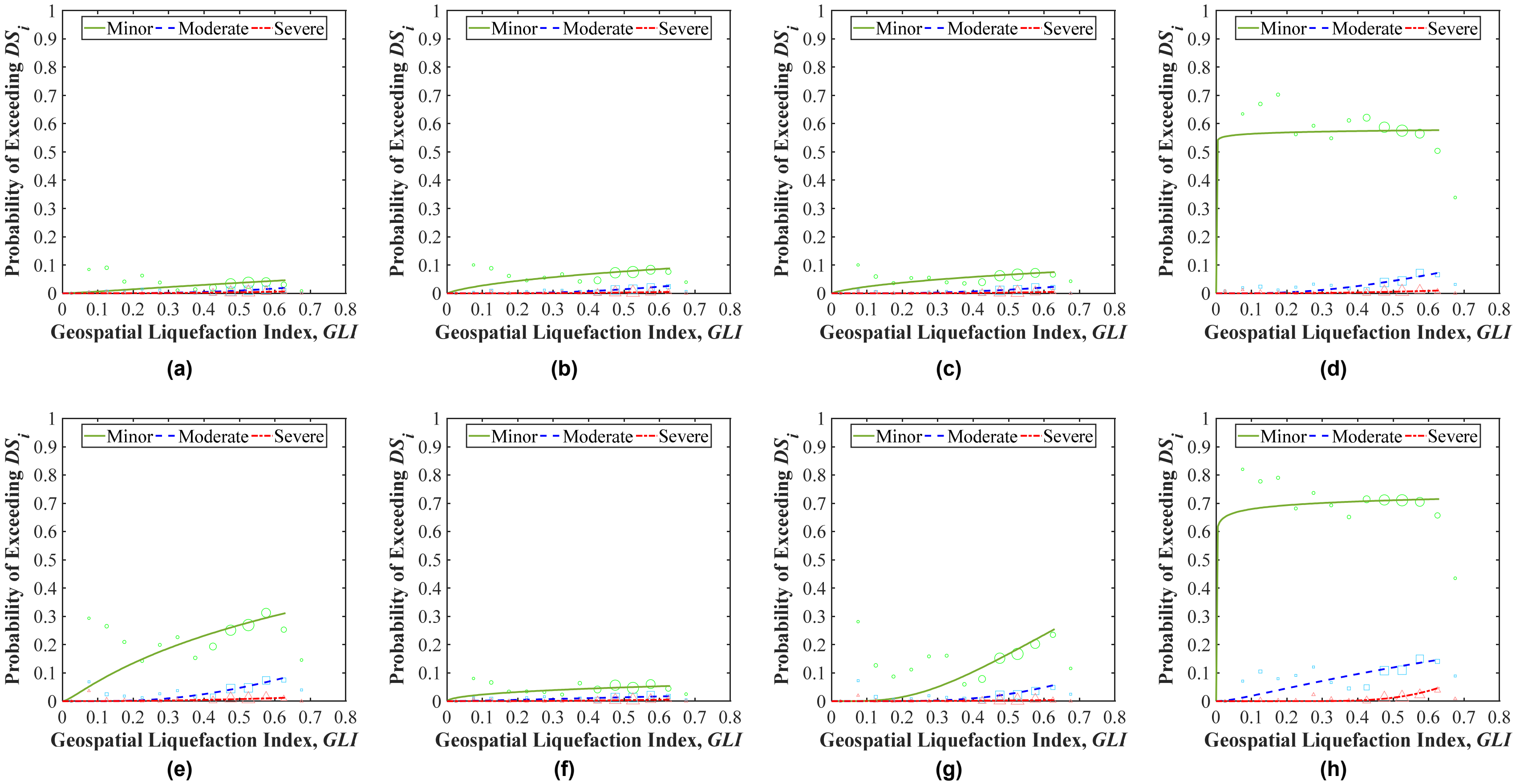

Figure B.2 **Fragility functions for predicting the probability of damage to timber on internal piles with perimeter concrete footing foundations using global geospatial model GGM2: (a) stretching failure; (b) hogging failure; (c) dishing failure; (d) twisting failure; (e) tilting failure; (f) discontinuous foundation failure; (g) global settlement failure; and (h) the failure mode with greatest observed severity.**

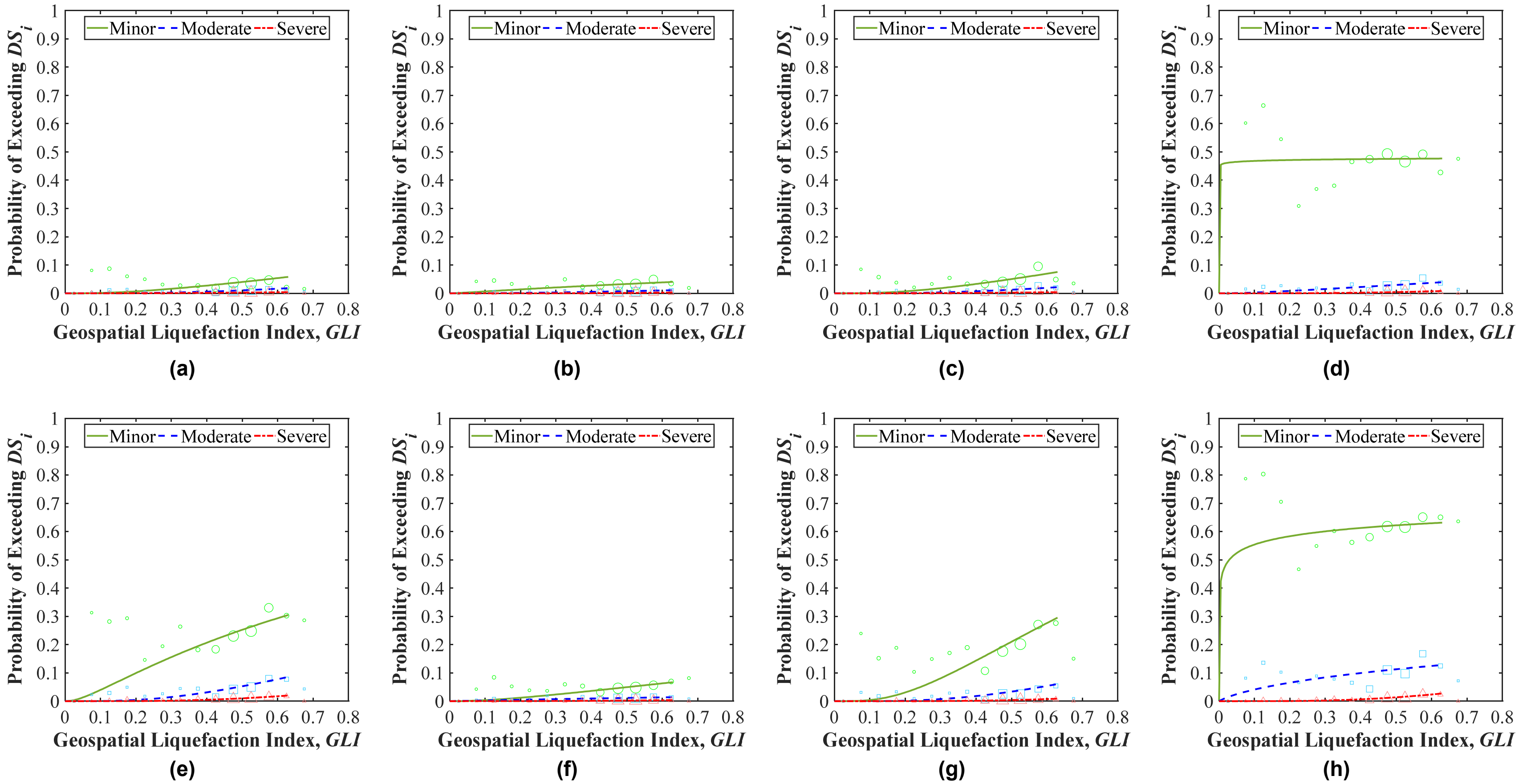

Figure B.3 **Fragility functions for predicting the probability of damage to concrete slab on grade foundations using global geospatial model GGM2: (a) stretching failure; (b) hogging failure; (c) dishing failure; (d) twisting failure; (e) tilting failure; (f) discontinuous foundation failure; (g) global settlement failure; and (h) the failure mode with greatest observed severity.**

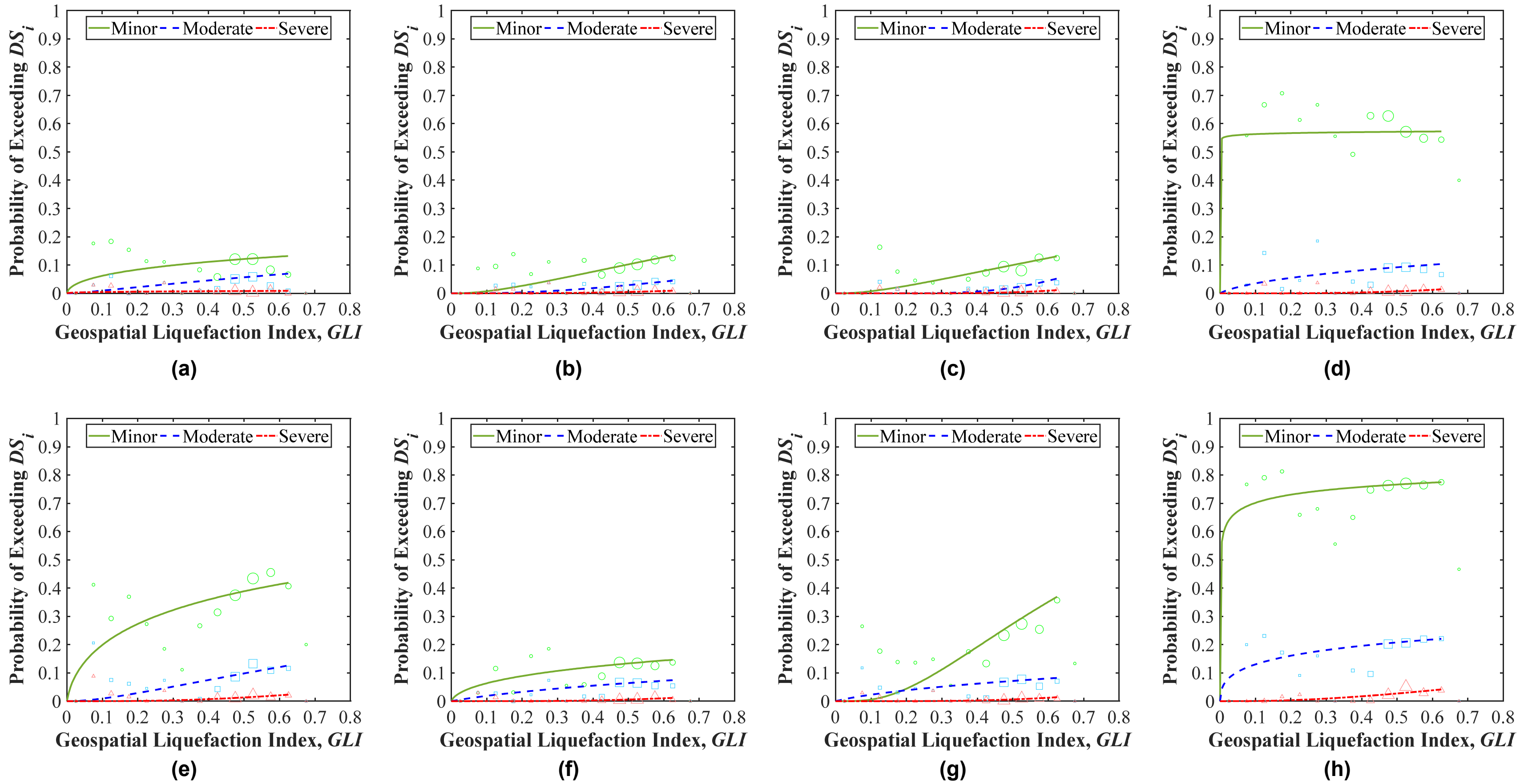

Figure B.4 **Fragility functions for predicting the probability of damage to Mixed foundations using global geospatial model GGM2: (a) stretching failure; (b) hogging failure; (c) dishing failure; (d) twisting failure; (e) tilting failure; (f) discontinuous foundation failure; (g) global settlement failure; (h) the failure mode with greatest observed severity.**

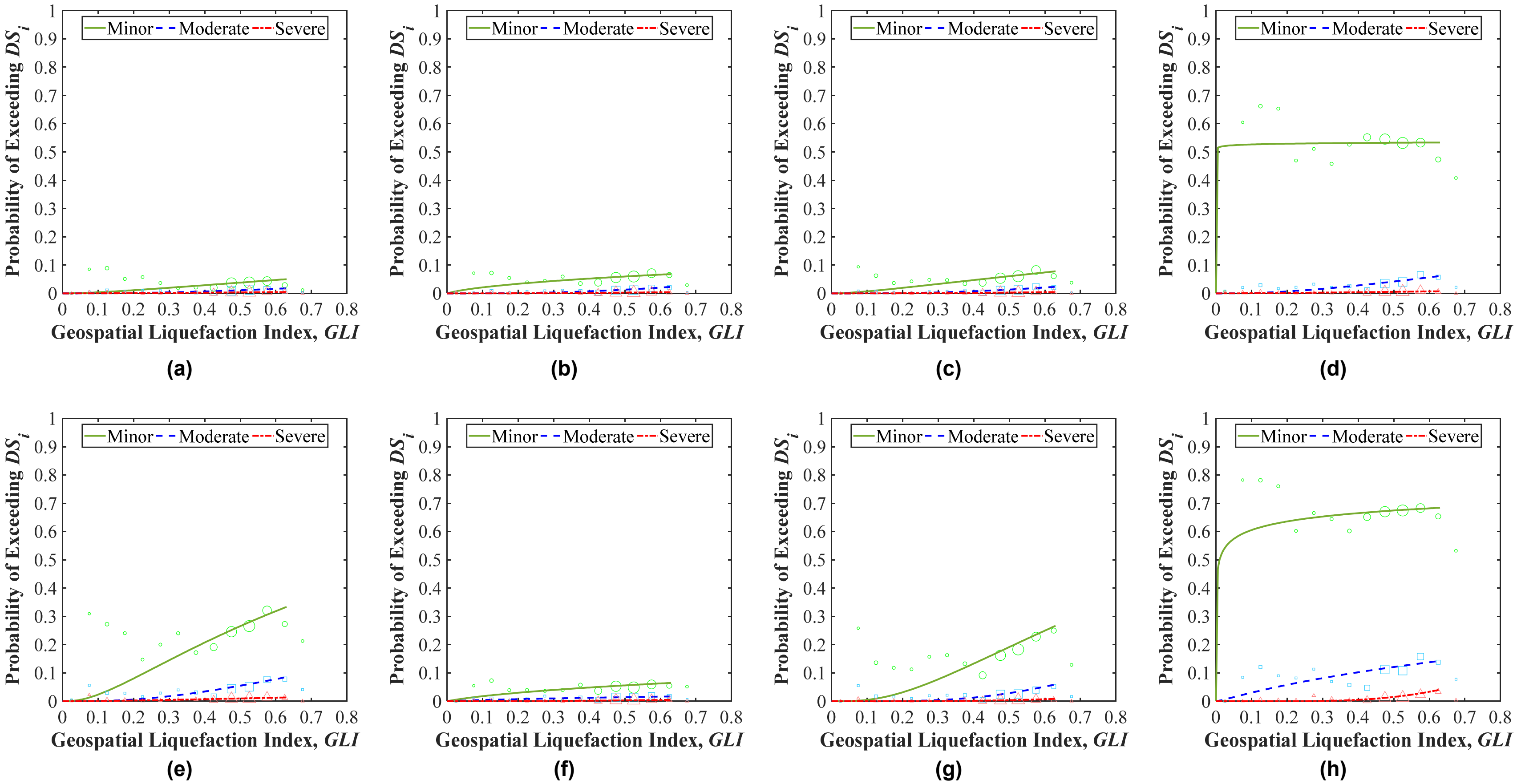

Figure B.5 **Fragility functions for predicting the probability of damage to shallow foundations (all variants) using global geospatial model GGM2: (a) stretching failure; (b) hogging failure; (c) dishing failure; (d) twisting failure; (e) tilting failure; (f) discontinuous foundation failure; (g) global settlement failure; and (h) the failure mode with greatest observed severity.**

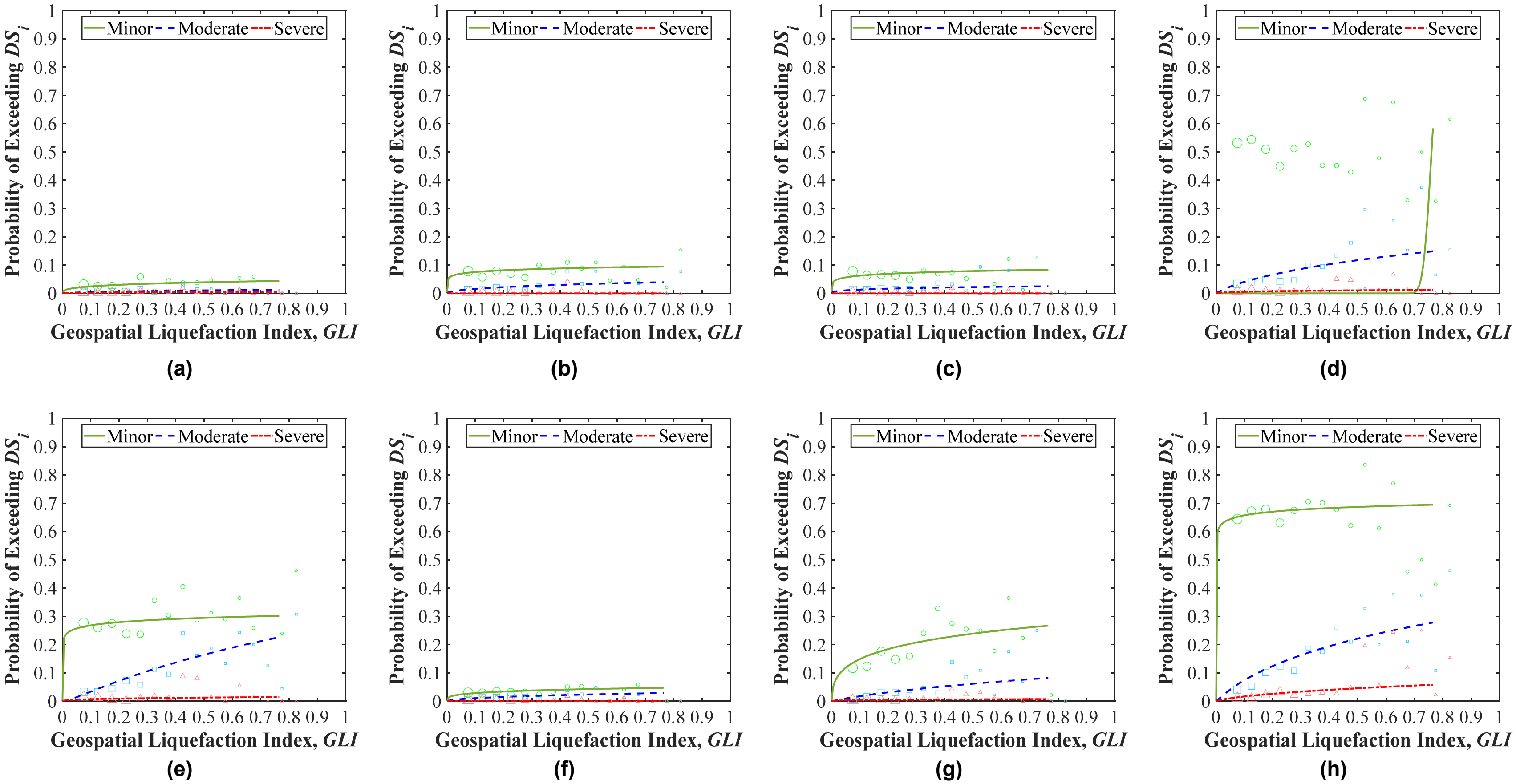

Figure B.6 **Fragility functions for predicting the probability of damage to timber floor on pile foundations using regional geospatial model RGM3: (a) stretching failure; (b) hogging failure; (c) dishing failure; (d) twisting failure; (e) tilting failure; (f) discontinuous foundation failure; (g) global settlement failure; and (h) the failure mode with greatest observed severity.**

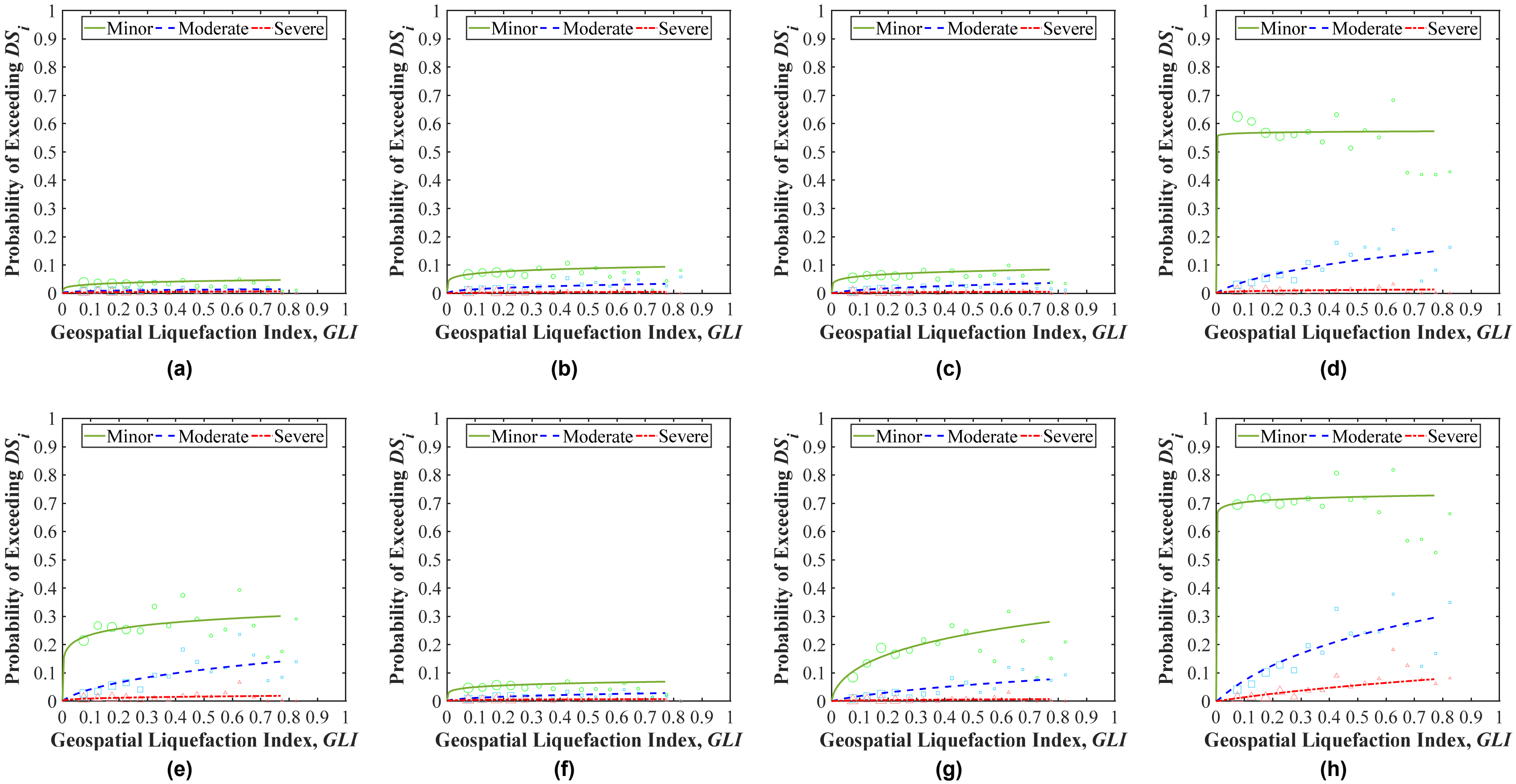

Figure B.7 **Fragility functions for predicting the probability of damage to timber on internal piles with perimeter concrete footing foundations using regional geospatial model RGM3: (a) stretching failure; (b) hogging failure; (c) dishing failure; (d) twisting failure; (e) tilting failure; (f) discontinuous foundation failure; and (g) global settlement failure; (h) the failure mode with greatest observed severity.**

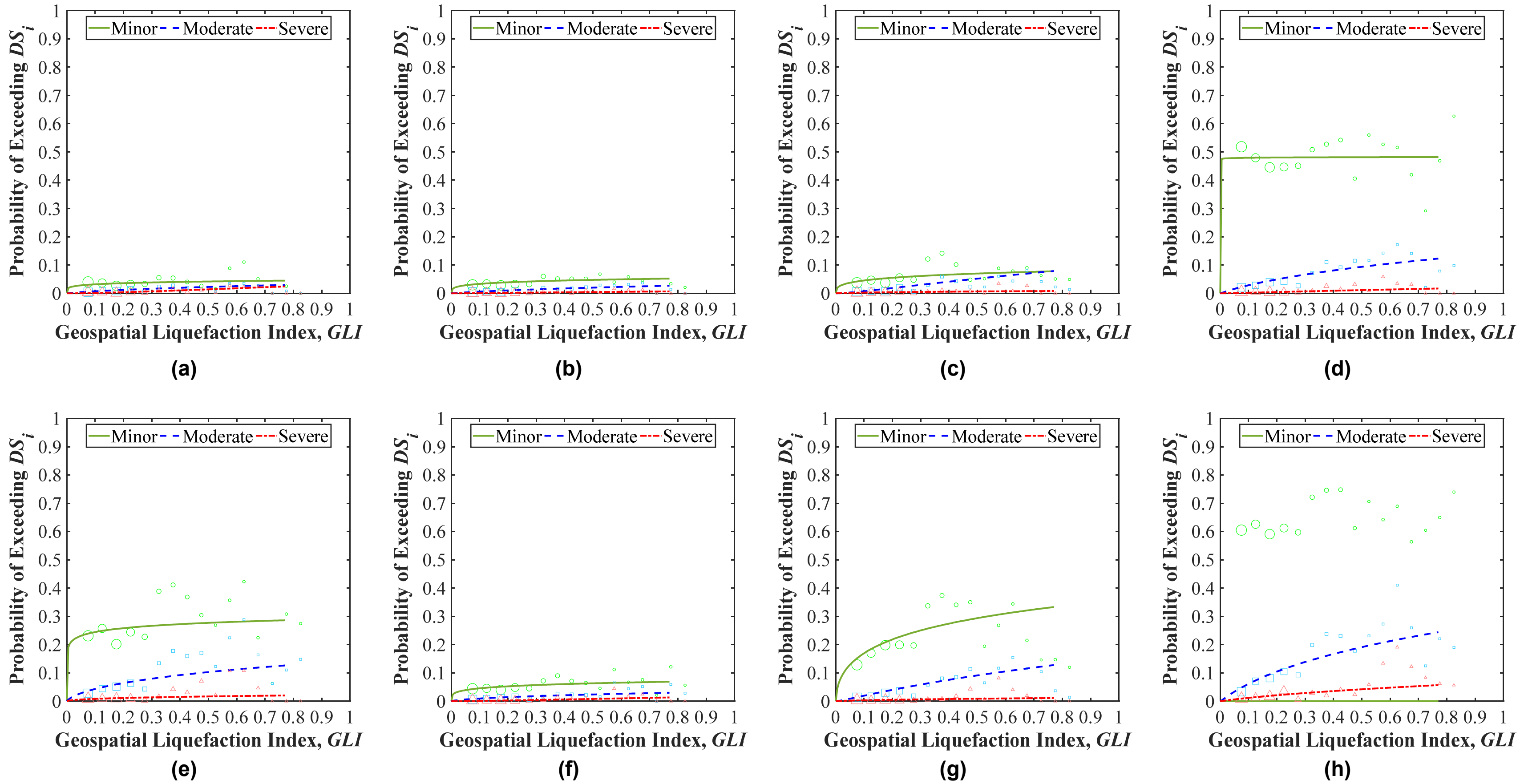

Figure B.8 **Fragility functions for predicting the probability of damage to concrete slab on grade foundations using regional geospatial model RGM3: (a) stretching failure; (b) hogging failure; (c) dishing failure; (d) twisting failure; (e) tilting failure; (f) discontinuous foundation failure; and (g) global settlement failure; and (h) the failure mode with greatest observed severity.**

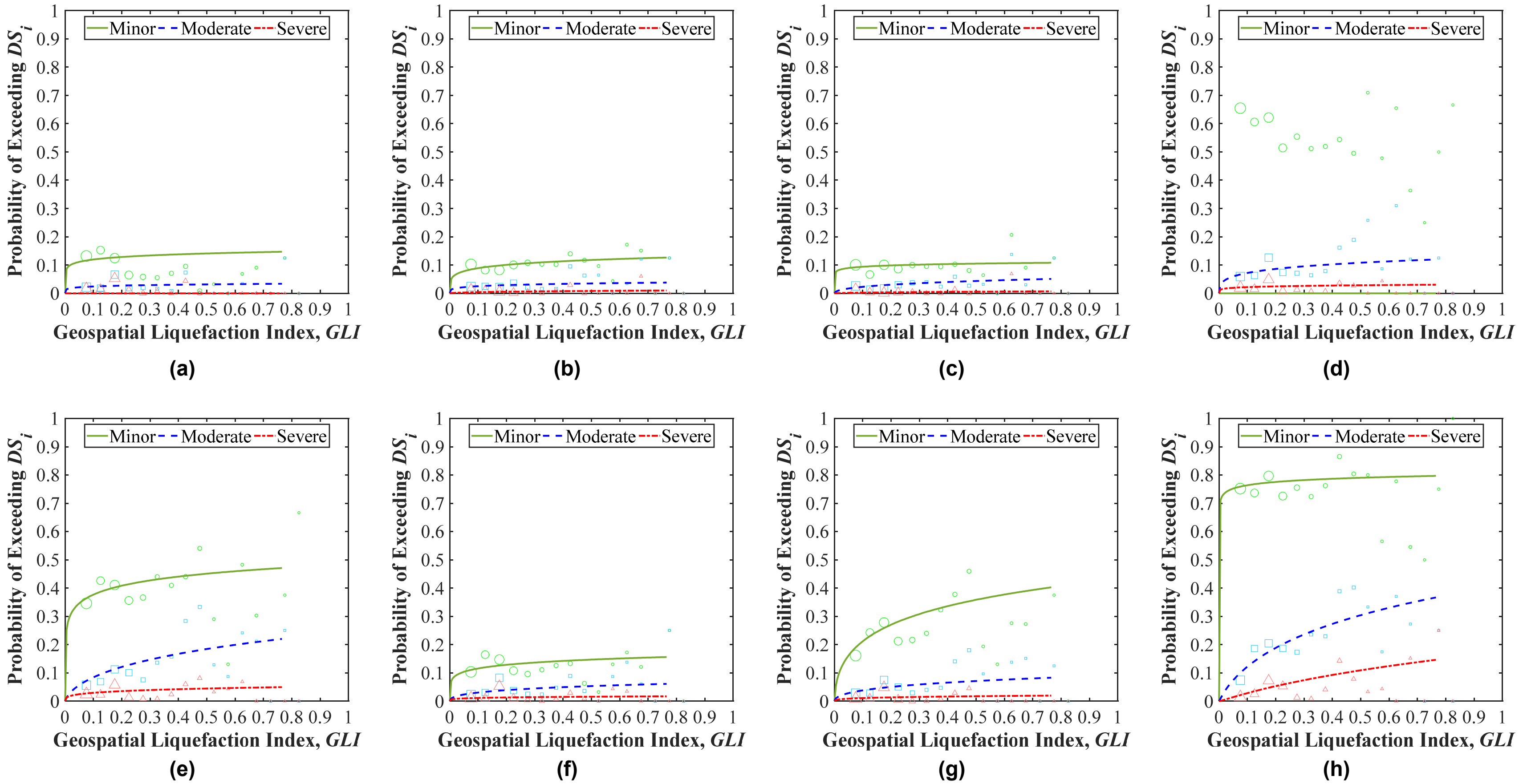

Figure B.9 Fragility functions for predicting the probability of damage to mixed foundations using regional geospatial model RGM3: (a) stretching failure; (b) hogging failure; (c) dishing failure; (d) twisting failure; (e) tilting failure; (f) discontinuous foundation failure; (g) global settlement failure; and (h) the failure mode with greatest observed severity.

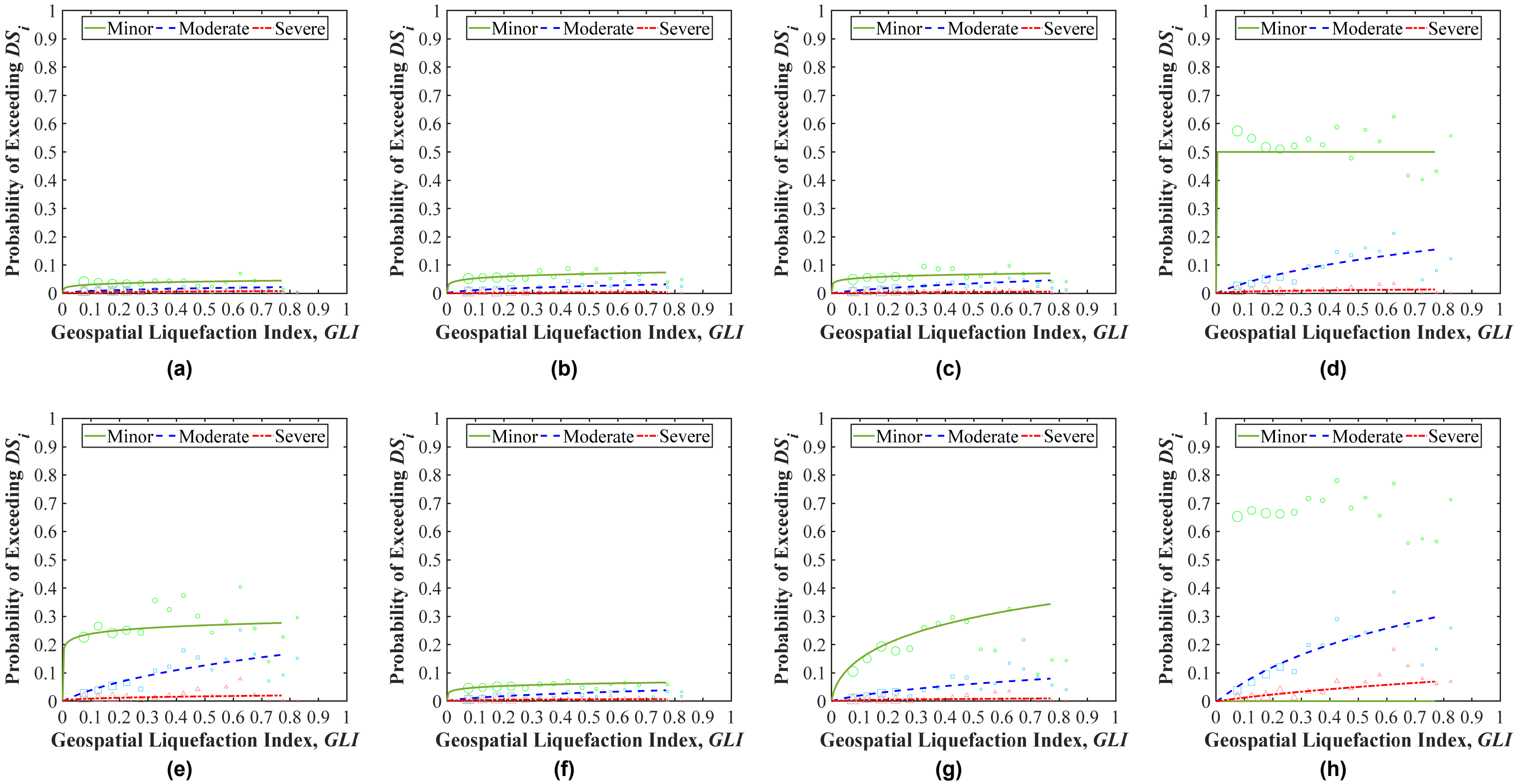

Figure B.10 **Fragility functions for predicting the probability of damage to shallow foundations (all variants) using regional geospatial model RGM3: (a) stretching failure; (b) hogging failure; (c) dishing failure; (d) twisting failure; (e) tilting failure; (f) discontinuous foundation failure; (g) global settlement failure; and (h) the failure mode with greatest observed severity.**

Table B.1 Fragility-function coefficients for geospatial model *RGM3*, which can be used to predict the probability of liquefaction-induced foundation damage exceeding a given severity, as defined in Figure 4.4.

			Stretching	Hogging	Dishing	Twisting	Tilting	Discontinuous foundation	Global settlement	Worst (all)
Timber floor on piles (Type A)	Minor	β	0.078	16.930	15.290	-	24.548	-	4.954	-
		x_m	1.449	3579715134.903	1464296169.904	-	365609.132	-	17.761	-
	Moderate	β	5.133	5.209	7.830	2.899	1.884	4.903	2.818	2.370
		x_m	73527.350	7220.297	3529586.069	15.665	3.151	8470.387	38.399	3.084
	Severe	β	6.846	0.117	0.117	6.754	7.110	0.117	8.984	3.630
		x_m	34879262.158	16.153	16.153	2811468.136	4142715.733	16.153	2866924982.818	230.295
Timber on internal piles with perimeter concrete footing (Type B)	Minor	β	10.877	12.375	12.237	-	10.348	11.452	3.451	-
		x_m	60115066.790	8700668.925	17676579.826	-	179.343	16802492.747	5.717	-
	Moderate	β	8.781	5.681	4.344	2.926	3.162	5.451	3.038	2.231
		x_m	155216559.280	25013.577	1864.084	16.269	23.475	24604.890	58.448	2.560
	Severe	β	8.305	6.676	8.399	9.131	7.449	11.491	6.037	2.615
		x_m	596434178.231	19365811.836	1346455813.461	446729231.433	4123055.832	1232641633278.430	2067746.754	31.646
Concrete slab on grade (Type C)	Minor	β	15.790	10.109	-	-	16.962	10.422	3.895	-
		x_m	284531612543.277	11115828.039	-	-	13054.515	4562906.457	4.141	-
	Moderate	β	3.659	3.500	2.013	2.755	3.569	4.339	2.193	2.397
		x_m	757.466	653.472	13.199	18.869	45.746	2741.985	9.329	4.062
	Severe	β	1.946	3.087	5.077	2.732	5.871	2.297	4.450	2.975
		x_m	35.695	1576.805	143309.416	250.134	132947.483	127.870	20176.974	85.422
Mixed Foundations	Minor	β	15.062	10.181	-	-	8.452	11.966	3.677	-
		x_m	5103886.446	88898.082	-	-	1.419	178572.180	1.896	-
	Moderate	β	13.861	11.181	5.656	7.154	3.366	6.183	5.249	2.469
		x_m	75906344189.413	315569458.331	7939.727	3453.424	10.297	10804.985	1102.818	1.773
	Severe	β	0.117	6.439	5.688	14.389	8.516	12.585	8.772	2.385
		x_m	16.153	2401770.649	864209.823	389815492927.571	961245.538	289653696327.526	55254278.802	9.426
All foundations	Minor	β	12.013	11.999	14.918	-	17.147	13.108	3.219	-
		x_m	546198426.962	26795894.400	2530161618.342	-	19932.695	291675689.965	2.810	-
	Moderate	β	5.318	4.829	3.428	2.602	2.610	4.095	3.163	2.117
		x_m	34125.943	5985.564	247.960	10.802	9.882	1075.954	65.977	2.385
	Severe	β	6.514	4.972	5.670	6.946	6.632	8.743	6.132	2.688
		x_m	5165746.808	302650.524	1232623.327	3420789.598	628953.677	1429244855.777	1299018.521	41.231

Table B.2 **Fragility-function coefficients for geospatial model *GGM2*, which can be used to predict the probability of liquefaction-induced foundation damage exceeding a given severity, as defined in Figure 3.4.**

			Stretching	Hogging	Dishing	Twisting	Tilting	Discontinuous foundation	Global settlement	Worst (all)
Timber floor on piles (Type A)	Minor	β	0.7901	1.209	2.0588	-	2.0991	-	0.9511	-
		x_m	2.1703	2.7396	10.4178	-	1.6448	-	1.2535	-
	Moderate	β	1.4845	0.6947	1.5133	0.976	0.6246	1.1016	1.0347	4.7003
		x_m	18.5092	2.1864	13.9522	2.4952	1.3086	5.9454	3.2863	89.053
	Severe	β	1.8459	1.4639	1.7405	2.0264	1.1891	1.234	2.0041	0.6732
		x_m	75.9703	32.8245	82.8354	80.3083	7.5253	15.5452	101.7372	2.136
Timber on internal piles with perimeter concrete footing (Type B)	Minor	β	2.5306	4.9707	3.3833	-	1.8677	4.0606	0.756	-
		x_m	46.3306	632.6935	81.5739	-	1.5787	322.1766	1.0373	-
	Moderate	β	0.8688	0.9265	0.9591	0.9218	0.7801	2.3117	0.6051	1.788
		x_m	3.8051	3.7801	4.2493	2.4073	1.8478	82.4018	1.6359	4.1193
	Severe	β	1.2189	1.2478	1.0026	1.1596	1.2617	1.3506	1.5441	0.3978
		x_m	13.0783	15.7803	8.3003	9.4004	10.9058	19.4781	38.9964	1.2235
Concrete slab on grade (Type C)	Minor	β	4.9323	2.7124	-	-	1.48	1.7033	0.8614	-
		x_m	3784.9445	73.4465	-	-	1.3417	8.2174	1.0012	-
	Moderate	β	1.083	1.6463	1.077	1.8323	0.9146	2.9712	0.8295	3.0567
		x_m	6.069	27.1361	5.5422	15.8071	2.2015	433.9911	2.2798	20.3189
	Severe	β	1.7043	0.9952	1.5914	1.0331	0.8444	1.3204	0.7737	0.8071
		x_m	57.5255	9.8321	43.1447	7.5061	3.5708	21.8156	3.9792	2.9769
Mixed Foundations	Minor	β	5.8007	1.3798	-	-	2.8556	4.5756	2.996	-
		x_m	439.7579	2.8744	-	-	1.1209	80.3509	3.9953	-
	Moderate	β	2.1195	1.1434	0.5146	3.3448	1.5117	2.8706	3.0141	5.1622
		x_m	14.3638	4.3518	1.4423	42.4222	3.5288	39.5498	41.3093	33.4292
	Severe	β	7.8593	0.9874	0.5718	0.8472	0.9755	0.8495	0.7358	1.1692
		x_m	78780584.93	6.3835	2.3045	4.0094	4.3797	4.3029	3.1512	4.7525
All foundations	Minor	β	2.3919	3.4041	1.7818	-	1.6945	3.7489	0.9286	-
		x_m	34.738	100.4902	7.8953	-	1.4452	193.077	1.1241	-
	Moderate	β	1.2652	1.0368	1.0379	1.2388	1.0038	3.5636	0.6751	2.2756
		x_m	9.0177	5.0013	4.9768	4.2592	2.4919	1238.7445	1.8053	7.1787
	Severe	β	2.0039	1.4974	1.4601	2.1879	1.9102	1.4331	0.8027	0.542
		x_m	111.9411	32.42	28.1578	131.1824	43.7671	26.2218	4.3299	1.6212

The Pacifi c Earthquake Engineering Research Center (PEER) is a multi-institutional research and education center with headquarters at the University of California, Berkeley. Investigators from over 20 universities, several consulting companies, and researchers at various state and federal government agencies contribute to research programs focused on performance-based earthquake engineering.

These research programs aim to identify and reduce the risks from major earthquakes to life safety and to the economy by including research in a wide variety of disciplines including structural and geotechnical engineering, geology/seismology, lifelines, transportation, architecture, economics, risk management, and public policy.

PEER is supported by federal, state, local, and regional agencies, together with industry partners.

PEER Core Institutions

University of California, Berkeley (Lead Institution)
California Institute of Technology
Oregon State University
Stanford University
University of California, Davis
University of California, Irvine
University of California, Los Angeles
University of California, San Diego
University of Nevada, Reno
University of Southern California
University of Washington

PEER reports can be ordered at https://peer.berkeley.edu/peer-reports or by contacting

Pacific Earthquake Engineering Research Center
University of California, Berkeley
325 Davis Hall, Mail Code 1792
Berkeley, CA 94720-1792
Tel: 510-642-3437
Email: peer_center@berkeley.edu

ISSN 2770-8314
https://doi.org/10.55461/QMOD7718